Application of Functionally Graded Materials
for Severe Plastic Deformation and Smart Materials
―Experimental Study and Finite Element Analysis―

巨大ひずみ加工およびスマートマテリアルへの
傾斜機能材料技術の応用
―有限要素法解析および実験的検証―

Thesis submitted to
Graduate School of Engineering,
Nagoya Institute of Technology.
Doctor degree of engineering.

by
Saifulnizan Jamian

Supervisors
Prof. Yoshimi Watanabe
Assoc. Prof. Hisashi Sato

Department of Engineering Physics, Electronics and Mechanics

2012

Declaration of Originality

I hereby declare that the research recorded in this thesis and the thesis itself was accomplished and originated entirely by myself in the Graduate School of Engineering at Nagoya Institute of Technology.

Saifulnizan Jamian

Abstract

Functionally graded materials (FGMs) refer to the composite materials where the compositions or the microstructures are locally varied so that a certain variation of the local material properties is achieved. Determination of compositional gradient and the process of making an FGM are dependent on its intended use. In this study, new possible applications of FGM and its production process were investigated. Three possible application of FGM were proposed.

First, the novel technique in producing ultra fine grain of difficult-to-work materials by equal-channel angular pressing (ECAP) process at ambient temperature was developed by using FGM. For this study, Ti as the difficult-to-work material was tightly encapsulated in a hollow host material made of Al-based FGM matrix. The Al-based FGM as a host material assists the deformation of Ti. The ECAP process was simulated by the finite element method (FEM) to determine the appropriate compositional gradient of Al-based FGM and the position to embed Ti wire. FEM was conducted with Ti embedded into a different host material type as well as different die channel geometry. The strain distribution of the specimen after a single ECAP pass was analyzed. From the obtained results, it is found that the strain distribution in Ti is strongly influenced by the host material and the shape of the die channel. An experimental work was carried out to confirm the ability of the proposed technique in producing ultra fine grain of Ti. The host material was prepared by embedding Al-Al$_3$Ti alloy into Al. Three types of the Al-Al$_3$Ti alloys with different Al$_3$Ti volume fractions were used to prepare the host materials. ECAP for specimens was carried out for up to eight passes by route A. The microstructure and hardness of ECAPed specimens were investigated. The changes in microstructure and the increase in the hardness value of Ti with increased number of ECAP passes are evidences showing that Ti is successfully deformed by this technique.

Second, new types of FGM crash boxes with stepwise strength gradient in longitudinal directions were proposed. The property of the proposed FGM crash boxes were analyzed using FEM. Crash behavior of the crash box under axial quasi-static and dynamic impact loads were studied. The obtained load-displacement curves and the crash failure patterns then were evaluated to assess the effect of the stepwise strength gradient of the crash-box.

Moreover, four different shapes of cross-sectional i.e. square, circle, pentagon and hexagon were considered. The results show that the FGM crash box is superior to than the homogeneous crash box in overall crashworthiness. Although there were no trigger mechanism introduced, the FGM crash boxes experience the progressive crushing initiated at the impact side.

Third, the FGMs were applied in pipe and pressure vessel field. A solution procedure for finite element thermo-visco-plasticity and creep analysis in an FGM thick-walled pressure vessel subjected to thermal and internal pressure was presented. The thick-walled pressure vessel was replaced by a system of discrete rectangular cross-section ring elements interconnected along circumferential nodal circles. The property of FGM was assumed to be continuous function of volume fraction of material composition. The thermo-visco-plasticity and creep behavior of the structures were obtained by the use of an incremental approach. The obtained results show that the material composition significantly affects the stress as a function of time at the inside and outside surface of thick-walled pressure vessel. The use of FGM can adjust the stress distribution in the structure.

Moreover, one of the FGM fabrication method, centrifugal casting, was investigated. Two types of centrifugal casting method namely, centrifugal solid-particle method (CSPM) and centrifugal mixed-powder method (CMPM), were used to fabricate Al/SiC FGM. Formations of graded distribution of SiC particles within molten Al by CSPM and CMPM under huge centrifugal force were examined and simulated. The movement of SiC particles in viscous liquid under centrifugal force was explained theoretically based on Stoke's law. The effect of composition gradient of particles on viscosity was taken into account. Also, the effect of temperature distribution on viscosity and density were considered. A computer code to simulate the formation of compositional gradient in an Al/SiC FGM manufactured by CSPM and CMPM was developed. From the obtained results, it was found that the SiC particles can be graded from inner to outer surface of Al/SiC FGM by CSPM. Meanwhile by CMPM, the SiC particles can be dispersed on the surface of Al/SiC FGM. The graded distribution in Al/SiC FGM under huge centrifugal force was significantly affected by the mold temperature but less affected by the initial temperature of molten Al and casting atmosphere.

Acknowledgments

During the development of my graduate studies in the Nagoya Institute of Technology several persons and institutions have collaborated directly and indirectly with my research. That is why I wish to dedicate this section to recognize their support.

First I would like to thank to ALlah, who gave me energy and courage to complete this thesis. I wish to extend my thanks to Prof. Yoshimi Watanabe and Assoc. Prof. Hisashi Sato for giving me the opportunity to study in their laboratory, for leading and helping me to achieve my goals. They have encouraged me, prepared me for the next step from the first day I came to the lab. From the system established in the lab, regular lab meetings, discussions and team working, I feel that I have gained interesting experiences. Finally, I thank them for their understanding, patience and professionalism.

I am also really grateful to Assoc. Prof. Miura, Prof. Tsukamoto, Dr. Kunimine, Ms. Yamada, Mrs. Suzuki, Ms. Asai and all the lab members for the continuous guidance and support during my study in Japan. It seems not complete if I do not mention some lab members' name here. Thanks are due to my colleges, Mizuno, Tabushi, Furukawa, Shibuya and Nishimura for their help during the experiments.

I would next like to thank the Ministry of Higher Education of the Malaysia Government for providing me with the scholarship to pursue my study in Japan. Thanks also to the support from "Tokai Region Nanotechnology Manufacturing Cluster in "*Knowledge Cluster Initiative*" by Ministry of Education, Culture, Sports, Science and Technology of Japan.

Finally, I would like to thank my parents, my wife, my son and my family members for their love, support and encouragement.

Table of Contents

Chapter 4 – A Numerical Crashworthiness Investigation of FGM Crash Boxes

under Axial Quasi-static and Dynamics Loading

Chapter 5 – Thermo-Visco-Plasticity and Creep Analysis of Thick-Walled

Pressure Vessels made of Functionally Graded Materials

Chapter 6 – Formation of Compositional Gradient in Al/SiC FGM Fabricated under Centrifugal Force: Solid-Particle Method and Mixed-Powder Method

Chapter 1

Introduction and Literature Survey

1.1 Functionally Graded Materials

Functionally graded materials (FGMs) refer to the composite materials where the composition or the microstructure is locally varied so that a certain variation of the local material properties is achieved. The materials can be designed for specific function and applications. Various approaches based on the bulk (particulate processing), preform processing, layer processing and melt processing are used to fabricate the FGMs [1]. The concept of FGM was fist considered in Japan in 1984 during a space plane project. That time the aim is to fabricate a space plane body's material with improved thermal resistance and mechanical properties by gradually changing (grading) compositions. Therefore, the space plane body is resistant to severe condition from temperature gap (about 1000 deg. C gap) in between the inside and the outside.

The structural unit of an FGM is referred to as an element or a material ingredient [1]. It is a conceptual unit for constructing an FGM that includes various aspects of its chemical composition, physical state and geometrical configuration. According to Miyamoto et al. [1] the term material ingredient, probably expresses the overall concept best. Generally, there are two main types of FGMs i.e. continuous graded materials and discontinuous graded materials. In the simplest FGMs, two different material ingredients change gradually from one to the other as illustrated in Fig. 1.1(a). In the second type, the material ingredients change in a discontinuous way such as the stepwise gradation illustrated in Fig. 1.1(b).

A material can be considered to be an FGM even if the gradation of the material ingredients is limited to a specific location in the material such as the interface, a joint, or a surface. As long as the material incorporates the FGM concept it can be categorized as an FGM. Therefore, an FGM can be produced from a homogeneous material and then processed with different condition such as heat treatment and deformation.
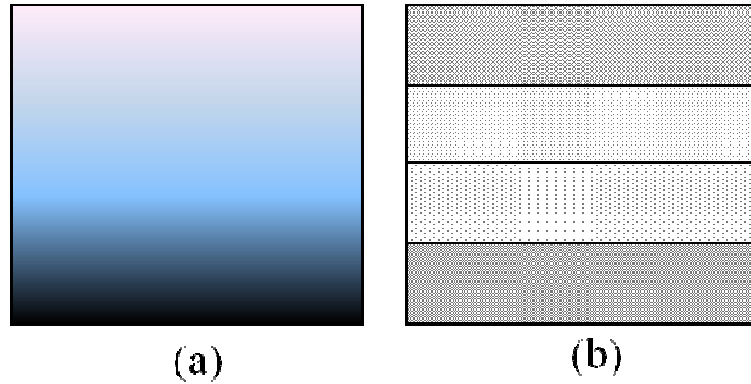
1

Fig. 1.1 Type of FGM structure: (a) continuous and (b) discontinuous.

1.2 Manufacturing Process of FGMs

There is wide variety of processing methods to fabricate FGMs available today [1–4]. The processing methods can be classified into those based on constructive processing and those based on mass transport [2]. In the first class, the FGM is constructed layer-by-layer starting with an appropriate distribution of the FGM's constituents. These techniques are called constructive processes because gradients are literally constructed in space. Meanwhile in the second class of FGM process, the gradients within a components are depend on natural transport phenomena such as the flow of fluid, the diffusion of atomic species, or the conduction of heat. FGMs can be manufactured by centrifugal casting [3], sequential slip casting [5], thermal spraying [6], physical vapour deposition (PVD) [7], chemical vapour deposition (CVD) [7] and laser cladding [8].

Powder metallurgy, a constructive processing method, is a one of the most important methods of producing FGMs. Generally, this method consists of three main steps. At first, materials desired in powder form are weighed and mixed. Next step is stepwise staking of premixed powder according to a predesigned spatial distribution of the composition. Last step is a sintering. By this method, the FGM fabricated usually have the stepwise structure, and it is difficult to produce the FGM with continuous gradient.

An example of natural transport phenomena method is centrifugal method. FGMs are fabricated under a centrifugal force, by which it is possible to produce the FGMs

2

with continuous gradients. Fabrication methods of FGMs under the centrifugal force are classified into three categories, namely centrifugal method (application of centrifugal casting), centrifugal slurry method (centrifugal sedimentation) and centrifugal pressurization method (simple pressurization by the centrifugal force). In case of centrifugal method, a centrifugal force applied to a homogeneous molten metal, dispersed with ceramics particles or intermetallic compound particles, drives the formation of the desired gradation. The composition gradient is then achieved primarily by the difference in the centrifugal force produced by the difference in density between the molten metal and solid particles [9, 10]. It is known that the motion of particles in a viscous liquid under a centrifugal force obeys the Stokes' law [10–12].

In contrast, slurry with two types of solid particles, high-velocity particle and low-velocity particle, is subjected to the centrifugal force during the fabrication of FGMs by the centrifugal slurry method [13]. After complete sedimentation occurs, liquid part of the slurry will be removed, and therefore, it does not become a part of FGM. Third one is the centrifugal pressurization method, by which the centrifugal force is only used for simple pressurization. In this method, compositional gradation should be formed prior the application of centrifugal force [14, 15].

1.3 Application of FGMs

Nowadays the researches on FGMs have been carried out intensively. Since the concept developed in aeronautics field in 1984, FGMs are also a concern in the other fields such as industrial materials, optoelectronics, biomaterials, and energy materials. FGMs offer great promise in applications where the operating conditions are severe. Potential applications include those structural and engineering uses that require combinations of incompatible functions such as refractoriness or hardness with toughness or chemical inertness with toughness. In aerospace and nuclear energy applications, reliability rather than cost is the key issue. On the other hands, in applications such as cutting tools, machine parts and engine components, which require wear, heat, mechanical shock and corrosion resistance, the key issues are the cost/performance ratio and reliability. Examples of available commercial FGM products are high performance cutting tools of

tungsten carbide/cobalt based FGMs and razor blades of an iron aluminide/stainless steel FGM [1].

There are many potentially useful applications of the FGM concept which is not limited to the fields discussed in this report as well as the manufacturing processes of FGMs. In this study, three possible applications of FGMs were discussed. For the two first proposed applications, the stepwise gradations FGMs were used. Meanwhile for the third proposed application, the continuous graded materials were chosen to be applied in tube and pressure vessel field.

1.4 Experimental and Numerical Approach

In analyzing the possible applications of FGMs proposed in this study both experimental and numerical works were carried out. In engineering applications, there are many types of numerical method that usually used such as finite difference method (FDM), finite volume method (FVM), finite element method (FEM), boundary element method (BEM) and mesh-free method. However in this study, for the numerical analysis only FEM was considered. FEM are widely used in diverse fields to solve static and dynamic problems. The advantages and disadvantages of FEM are listed in Table 1.1

In FEM the solution procedure is very typical. The main steps in implementation of FEM are summarized as follow:

a) Discretization of the domain into a set of finite elements.
b) Defining an approximate solution over the element.
c) Weighted integral formulation of the differential equation.
d) Substitute the approximate solution and get the algebraic equation

Table 1.1 Advantages and disadvantages of FEM

Advantages	Disadvantages
Able to handle very complex geometry	A general closed-form solution, which would permit one to examine system response to changes in various parameters, is not produced.
Able to solve a wide variety of engineering problems	The results obtains only "approximate" solutions
Able to handle complex restraints	It has "inherent" errors.
Able to handle complex loading	Mistakes by users can be fatal.

The main challenge to implement FEM in analyzing FGMs structures is to describe the material properties of FGMs. To describe the material properties of FGMs by theoretical approach is not easy. The estimation of material properties for phase composites by theoretical approaches are split into microscopic and overall studies. The prediction methods of overall material properties are generally classified into three group i.e direct, variational and approximation approaches. The direct method seeks closed-form analytic solution. Therefore a precise mathematical treatment becomes troublesome. On the other hand, the variational method such as Hashin Shtrikman's bounds does not specify the details in the phase geometry but rather provide the upper and lower bounds for the overall properties. In the approximation approach, the self-consistent model by Hill and the others, the mean field micro-mechanics models by Mori and Tanaka and Wakashima and Tsukamoto, the linear and modified rules of mixtures by Tamura and the unit cell model by Ravichandran are widely employed overall estimation [1−3]. The overall models are simple and convenient to predict the overall thermo-mechanical response and material properties. However, in this study, the conventional modeling of FGMs, the rule of mixture is considered. Although, the macroscopic properties of FGMs cannot be accurately described by the rule of mixture,

but by dividing the FGMs structure into significantly small size of mesh and the material properties considered at every integration points is gives reasonable results when analyzing the FGMs structure by FEM.

In this study, FEM is used to determine the appropriate FGMs structure for the proposed application to reduce number of experimental works carried out. Experimental work still required to be performed in order to prove the workability of the proposed FGMs applications.

1.5 Thesis outline

In Chapter 2, the novel technique in producing ultra fine grain of difficult-to-work materials by ECAP process at ambient temperature was developed by using FGM. The ECAP process was simulated by the FEM to determine the appropriate compositional gradient of Al-based FGM and the position to embed Ti wire.

In Chapter 3, an experimental work was carried out to confirm the ability of the proposed technique in producing ultra fine grain of Ti. The microstructure and hardness of ECAPed specimens were investigated.

In Chapter 4, new types of FGM crash boxes with stepwise strength gradient in longitudinal directions were proposed. Finite element analysis was performed in order to determine the crash behavior of the crash boxes. The crashworthiness characteristics of FGM crash boxes were discussed.

Chapter 5 discussed the possible application of FGM in pipe and pressure vessels field. The analysis of thermo-visco-plasticity and creep characteristics of the FGM thick-walled pressure vessels were carried out using FEM. The obtained results show that the use of FGMs can adjust the stress distribution in the structure.

Finally Chapter 6 describes the promising mass manufacturing of FGMs, centrifugal casting. The fabrications of Al/SiC FGM using two types of centrifugal casting method namely, solid-particle method and mixed-powder method, were carried out. The formation of graded distribution of SiC particles within molten Al by centrifugal solid-particle method and centrifugal mixed-powder method were examined and simulated.

Chapter 7 present the overall conclusion and recommendation for future work in this research area.

References

1) Y. Miyamoto, W.A. Kaysser, B.H. Rabin, A. Kawasaki, and R.G. Ford: Functionally Graded Materials: Design, Processing and Applications, Kluwer Academic, Boston (1999).

2) S. Suresh and A. Mortensen: Fundamental of Functionally Graded Materials, The University Press, Cambridge (1998).

3) A. Neubrand and J. Rödel. Gradient Materials: An overview of a novel concept. Z. fur Metallkunde. **5(88)** (1997) 358.

4) Y. Watanabe and H. Sato: Review Fabrication of Functionally Graded Materials under a Centrifugal Force, Nanocomposites with Unique Properties and Applications in Medicine and Industry (2011) 133.

5) J.S. Moya, J.A. Sánchez-Herencia, J. Requena, and R. Moreno: Mat. Let. **14**(1992) 333.

6) J. Musil and J. Fiala: Surface and Coating Technology **52** (1992) 211.

7) D.C. Sun, E.Y. Yiang, S. Liu Ming, and C. Lin: J.Phys. D: Applied Physics **28** (1995) 4.

8) K.M. Jasim, R.D. Rawlings, and R.F. West: J. Mater. Sci. 43(1-4) (1993) 2820.

9) Y. Fukui: JSME Int. J. Series III, **34 (1)** (1991) 144.

10) Y. Watanabe, N. Yamanaka, and Y. Fukui: Comp. A **29A** (1998) 595.

11) C.G. Kang and P.K. Rohatgi: Metall Mater Trans B **27B** (1996) 277.

12) T. Ogawa, Y. Watanabe, H. Sato, I.S. Kim, and Y. Fukui: Comp. A **37** (2006) 2194.

13) Watanabe, E. Miura-Fujiwara, and H. Sato: J. Jpn. Soc. Powder Powder Metall. **57** (2010) 321.

14) Y. Watanabe, S. Watanabe, and K. Matsuura: Metall. Mater. Trans. A **35A** (2004) 1517.

15) Y. Watanabe, Y. Inaguma, H. Sato, and E. Miura-Fujiwara: Mater. **2** (2009) 2510.

Chapter 2

Finite Element Analysis of Severe Plastic Deformation of Difficult-to-Work Material by Equal-Channel Angular Pressing at Ambient Temperature

2.1 Introduction

Equal-channel angular pressing (ECAP) invented by Segal et al.[1] in 1977 is one of the severe plastic deformation (SPD) techniques, which has great potential for producing ultrafine grain materials in bulk. Figure 2.1 shows a schematic illustration of ECAP process. As shown in Fig. 2.1, the ECAP process is performed by pressing a specimen through a die consisting of two intersecting channels meeting at an angle ϕ and outer corner meeting at an angle φ. This process has the advantage that a large plastic strain can be induced without changing the cross section of the specimen. Because of it, a larger plastic strain is imposed by repeating several passes. In addition, the ECAP process has four standard routes: route A (no rotation), route B_A (90° back and forth rotation between passes), route B_C (90° in the same direction between passes), and route C (180° in the same direction between passes). Therefore, the property of the induced strain can be controlled by the processing route.

In the case of the deformation of a high-strength material using ECAP, an elevated temperature is often required [2, 3]. In particular, Ti alloys are difficult to deform, and a higher pressing-temperature is required to increase their ductility during the deformation. This is because Ti and Ti alloys have limited numbers of slip systems owing to the crystal having a hexagonal close packed (hcp) structure [4, 5]. In previous studies, the ECAP process for Ti has been performed under elevated temperatures [3−8]. In previous studies, this ECAP process for Ti was carried out at elevated temperatures up to 450 °C, and they suggested that the lowest temperature for deforming Ti successfully was 200 °C [8]. Therefore, it is very difficult to deform Ti by ECAP at room temperature.
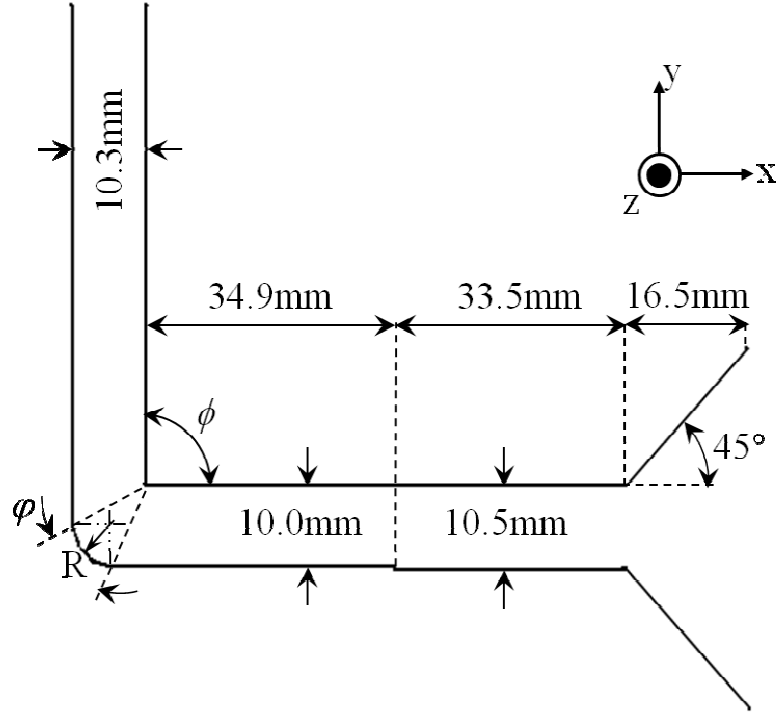
Fig. 2.1 ECAP die geometry featuring the die angle ϕ, outer corner angle φ, and outer fillet radius R.

Recently, the present authors have proposed a new technique of ECAP at ambient temperature [9]. The proposed ECAP process is carried out by embedding a difficult-to-work material into an easy-to-work material. According to our previous study, Ti (difficult-to-work material) has been successfully deformed by embedding it into pure Al (easy-to-work material) at room temperature. However, the proposed method has the problem that a crack is generated at the interface between Ti and pure Al during ECAP. In order to solve this problem, it is considered that the easy-to-work material should be an Al-based alloy or an Al-based functionally graded material (FGM). This is because it is better to decrease the difference in mechanical property between the difficult-to-work material and the easy-to-work material. Moreover, the amount of strain induced in Ti by the proposed ECAP is still unclear.

9

In this study, a comprehensive examination of the deformation of a difficult-to-work material using ECAP at room temperature is carried out by the finite element method (FEM). For this study, Ti as the difficult-to-work material is embedded into an Al-based alloy and an Al-based FGM matrix. The strain distribution in a specimen induced with single-pass ECAP depending on the position of Ti, the material for the matrix, and the geometry of die channels are discussed. From the obtained results, the capability of the proposed ECAP process to deform difficult-to-work materials is also discussed.

2. 2 FEM Analysis for the Strain Distribution in Specimen Induced by ECAP

FEM simulation was performed using the implicit finite element code Marc. The solution procedure is based on the full Newton-Raphson iterative-increment procedure. For the convergence criteria, the relative displacement criterion and relative residual force criterion are used, and convergence is obtained if one converges. Two-dimensional plane strain modeling is applied since material flow in the z-direction is restricted [10] for a single ECAP pass. A plane representing the ECAP specimen was divided into a mesh of 1200 equal four-node quadrilateral elements with 21 nodes in the x-direction and 61 nodes in the y-direction. The frictional coefficient between the die channel inside and the specimen is assumed to be zero because the specimen is lubricated during the experiment of ECAP. The geometry of the die channel is also shown in Fig. 2.1. The die channel and puncher made of die steel (DC53) produced by Daido Steel Co, Ltd. were considered to be rigid. The puncher moved down along the inlet channel at a constant velocity of 4 mm/s. To describe briefly the experiment of ECAP, the dummy specimen is used to push the specimen out of the die channels. After being pressed by the puncher for 50 mm, the specimen is pushed out by the dummy specimen. The schematic process of ECAP is shown in Fig. 2.2.

Figure 2.3 shows two types of specimen used in this simulation. For one specimen shown in Fig. 2.3(a), Ti with a length of 20 mm and a width of 1 mm is embedded at the end of the host material. The other specimen shown in Fig. 2.3(b) has the structure in which Ti is embedded in the middle of the host material. The host material is either an alloy or FGM with gradient strength. The FGM matrix is made by combining two

10

different Al alloys with the higher-strength alloy on the inner side, as defined in Table 2.1. The dimensions of the host material are 60 mm in length and 10 mm in width, and for the FGM matrix, the second layer is 40 mm in length and 5 mm in width. In the simulation, each material is defined as a different deformable body. For simplicity, the nodes at the interface belong to both materials and the separation of nodes is not considered.
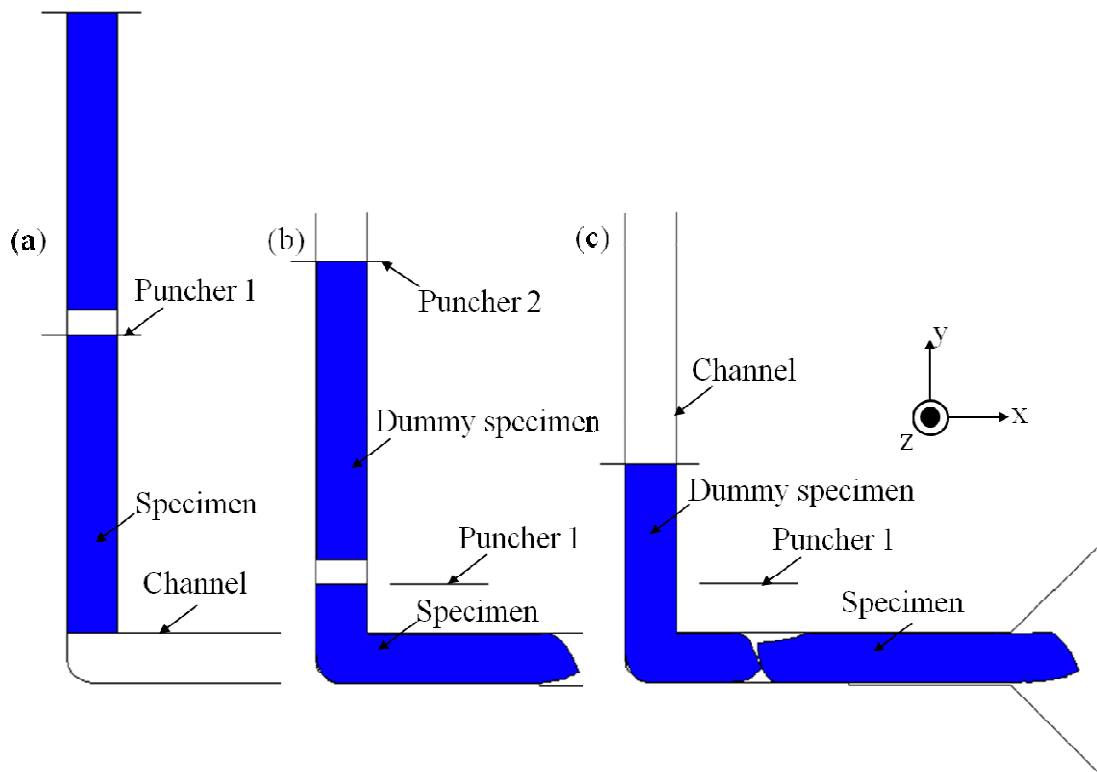

Fig. 2.2 ECAP process: (a) the initial deformation stage, (b) during steady-state of ECAP, and (c) the final stage after ECAP.
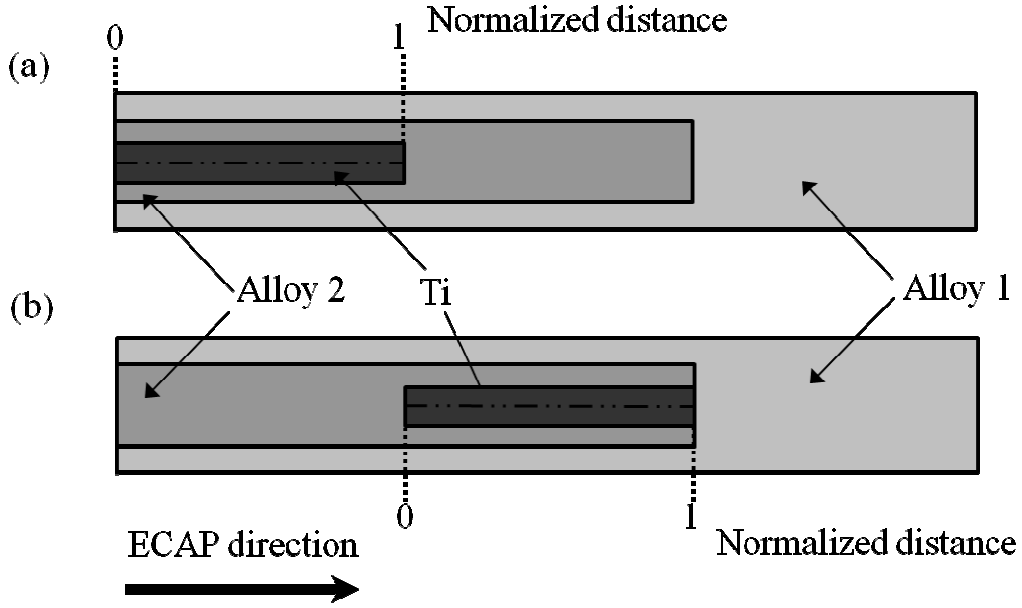
Fig. 2.3 Schematic of ECAP specimens: (a) Ti embedded at the end and (b) Ti embedded in the middle of specimen. The representative line defined along Ti is indicated.

As listed in Table 2.1, pure Al, Al-5%Ti, and Al-10%Ti are used as the host materials. The material properties of Al-5%Ti and Al-10%Ti are determined from the material properties of pure Ti and Al on the basis of the law of mixture. Although these material properties are inaccurately described, it is adequate to show the different strengths of these alloys used in this simulation. Young's modulus, E, Poisson's ratio, v, and yield stress, σ^y, for Al are 71 GPa, 0.33, and 22.5 MPa, respectively. On the other hand, E, v, and σ^y for Ti are 116 GPa, 0.32, and 140 MPa, respectively. The strain hardening for both materials can be presented as follows,

$$\sigma_{Al} = \sigma_{Al}^y \left[1 + 3.5 \left(\varepsilon^P \right)^{0.7} \right], \tag{2.1}$$

$$\sigma_{Ti} = \sigma_{Ti}^y \left[1 + \left(\varepsilon^P \right)^{0.25} \right], \tag{2.2}$$

where σ is the flow stress and ε^P denotes the equivalent plastic strain.

Table 2.1 List of the specimens defined on the basis of Fig. 2.3.

Sample	Alloy 1	Alloy 2
H1	Al	Al
H2	Al-5 mass%Ti	Al-5 mass%Ti
H3	Al-10 mass%Ti	Al-10 mass%Ti
FGM1	Al	Al-5 mass%Ti
FGM2	Al	Al-10 mass%Ti
FGM3	Al-5 mass%Ti	Al-10 mass%Ti

Firstly, the finite element calculation was validated by comparing with analytical solution. Since the frictional effect is neglected, the obtained results can be compared with equivalent strain presented in following equation [11]

$$\varepsilon = \frac{1}{\sqrt{3}}\left[2\cot\left(\frac{\phi}{2}+\frac{\varphi}{2}\right)+\varphi\cosec\left(\frac{\phi}{2}+\frac{\varphi}{2}\right)\right] . \tag{2.3}$$

In this equation, $\phi = 90°$ and $\varphi = 37.5°$, which corresponds to R = 5.15 mm, were considered as the size of the ECAP die. The equivalent strain estimated using Eq. (2.3) is 0.99 while the obtained value calculated by FEM is 1.08. This estimated value is in good agreement with that calculated by FEM. This means that the present FEM analysis is valid as the analysis method for strain distribution in ECAPed specimens.
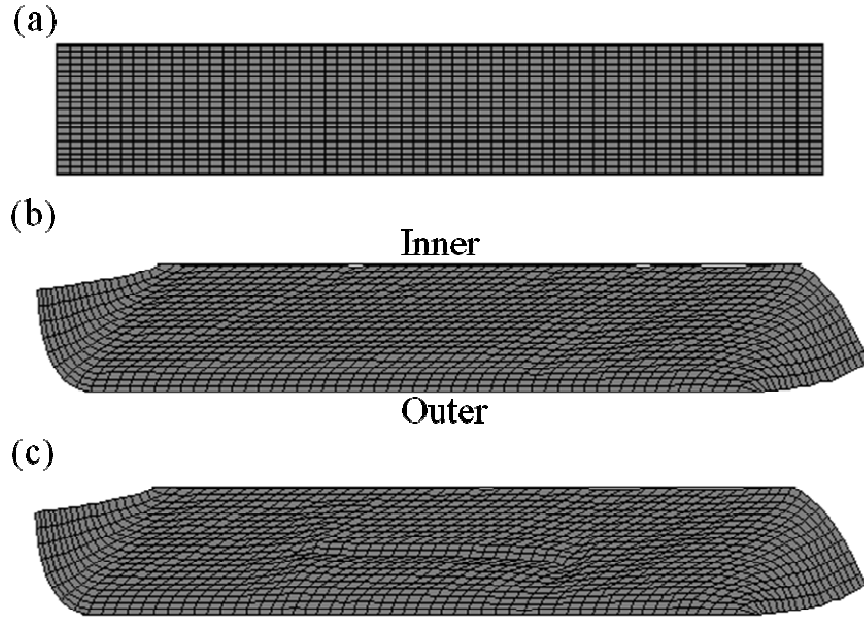
13

(a)

(b)

Inner

Outer

(c)

Fig. 2.4 Deformed geometry changes during ECAP: (a) Before ECAP; (b) and (c) after single pass of pure Al without and with Ti embedded, respectively.

Figure 2.4 shows the comparison of deformed geometry after a single ECAP pass. As shown in Fig. 2.4, the equal-quadrilateral-element mesh is distorted by passing through the angular shear zone. Moreover, it is seen from Fig. 2.4(b) that shear deformation in the outer part of the ECAP sample is smaller than in another part. This is in agreement with the results of previous studies [2, 12–15].
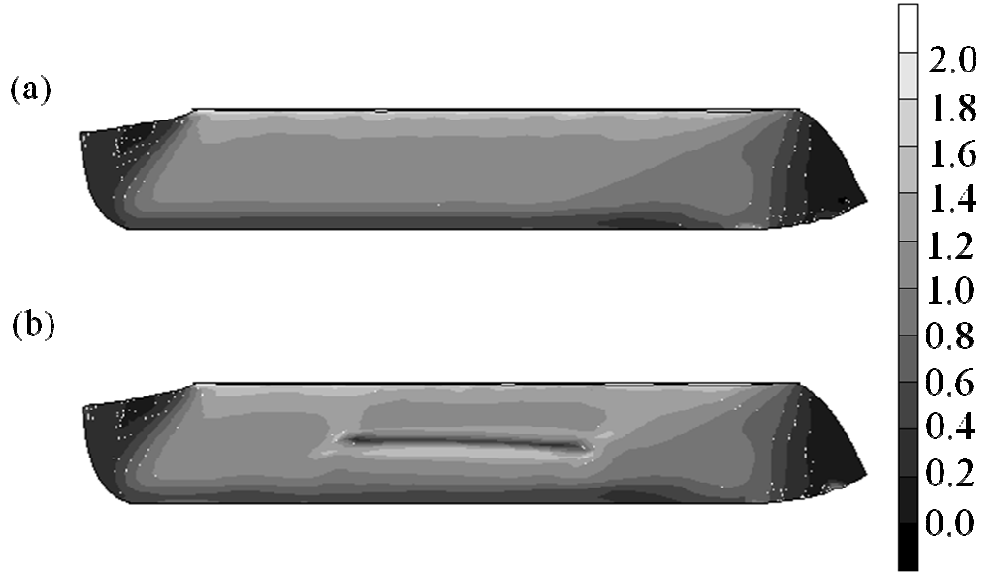
Fig. 2.5 Comparison of distribution of the equivalent strain in the specimen after single ECAP pass: (a) pure Al and (b) Ti embedded in pure Al (H1).

The deformation of a specimen during the ECAP process is inhomogeneous. The calculated strain varies along the specimen axis and the transverse direction from top to bottom. Figure 2.5(a) presents the distribution of equivalent strain in the pure Al sample after a single ECAP pass. As can be seen, the difference in the shape of specimen at the head and tail also shows that the deformation is inhomogeneous along the longitudinal direction. In order to quantify the degree of strain inhomogeneity, the coefficient of variance of the equivalent strains, *CV*, introduced by Patil et al. is used [16]. The coefficient of variance of the equivalent strains is defined as

$$CV = \frac{\text{Stdev}\,\varepsilon}{\varepsilon_{ave}} \quad , \qquad\qquad (2.4)$$

where $\text{Stdev}\,\varepsilon$ is the standard deviation of equivalent strain and ε_{ave} is the average of the equivalent strains along a chosen section of the specimen.

2.3 Results and Discussion

2.3.1 Influence of the Position of Ti in Matrix on Strain Inhomogenity along Ti

In order to determine the best position for embedding Ti in the host material, three different positions were considered. As the initial structure, two types of specimen shown in Fig. 2.3 are considered in this simulation. Figures 2.4(c) and (b) show the deformed geometry and the distribution of the equivalent strain in specimen H1 with Ti embedded in the middle after a single ECAP pass, respectively. As can be observed, the deformation and the strain distribution are inhomogeneous in both the longitudinal direction and transverse direction. Moreover, it is seen from Fig. 2.4(c) that the amount of shear strain in Ti is less than that in the host matrix.

Figure 2.6 shows strain distributions along the neutral axis of the specimen for sample H1 and FGM2. Figures 2.6(a), (b), and (c) are results obtained for specimens in which Ti is embedded at the front end, in the middle, and at the rear end of the specimen, respectively. For comparison, the strain distributions in specimen without Ti are also shown in those figures. In the case of the specimen without Ti, strain distribution along the neutral axis is relatively homogeneous. On the other hand, equivalent strains in samples H1 and FGM2 drastically dropped in the part with Ti, and the strain distribution in another region is similar to that of Al without Ti. Comparing the strain distributions in Ti between H1 and FGM2, it is found that Ti embedded in the middle has the most homogeneous strain distribution and the highest equivalent strain. Therefore, it can be concluded that the middle part in the host material of an ECAPed specimen is the appropriate position to induce SPD in a difficult-to-work material.
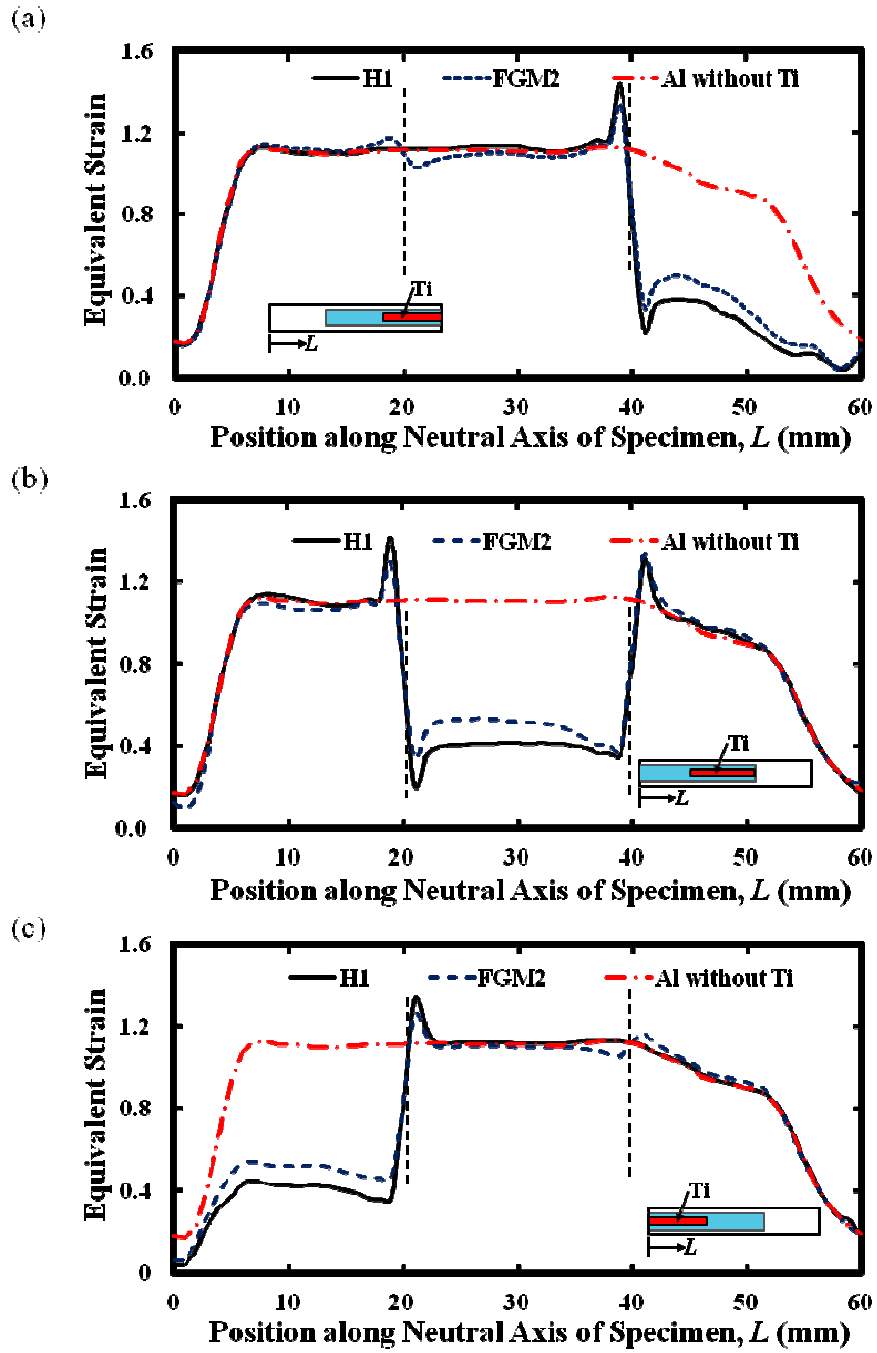
16

Fig. 2.6 Variation of equivalent strain along neutral axis of specimen with Ti in different positions: (a) at the front end, (b) in the middle, and (c) at the rear end. The schematic illustrations in graphs show the position of Ti. The dash lines indicate the interface between alloys.

17

2.3.2 Influence of the Host Material on Strain Inhomogeneity along Ti

To investigate the effect of the properties of the host material, FEM analysis was carried out using a different host material, as shown in Table 2.1. Figure 2.7 presents variation of equivalent strain inside Ti as a function of the normalized distance along Ti shown in Fig. 2.3. Figures 2.7(a) and (b) are ECAPed specimens with host materials of the homogeneous matrix (H1, H2 and H3) and composite matrix (FGM1, FGM2, and FGM3), respectively. Comparing the strain distributions along Ti embedded into homogeneous and FGM host materials, the strain distribution along Ti in FGM host materials is more homogeneous than that in the specimen with homogeneous materials. Also, the equivalent strain along Ti in the specimen with FGM host materials is relatively higher than that in the specimen with homogeneous materials. From these results, it is found that FGM is better than a homogeneous material as the host material in ECAP.

Moreover, it is found that the strain distributions of Ti in H3 and FGM3 show almost no difference and only show a small difference from that of Ti in FGM2. For these three specimens, Ti is embedded in the same inner layer material (Al-10%Ti) and is distinguished by the outer layer material. The outer layer materials of H3, FGM3, and FGM2 are Al-10%Ti, Al-5%Ti, and Al, respectively. Because FGM3 has almost similar strengths of the outer and inner layer materials, the strain distribution of Ti in FGM3 becomes similar to that in H3. On the other hand, a significant difference in the strength between the outer and inner layer materials of FGM2 gives a different strain distribution of Ti. These results show the significance of the gradient in strength of the host material.
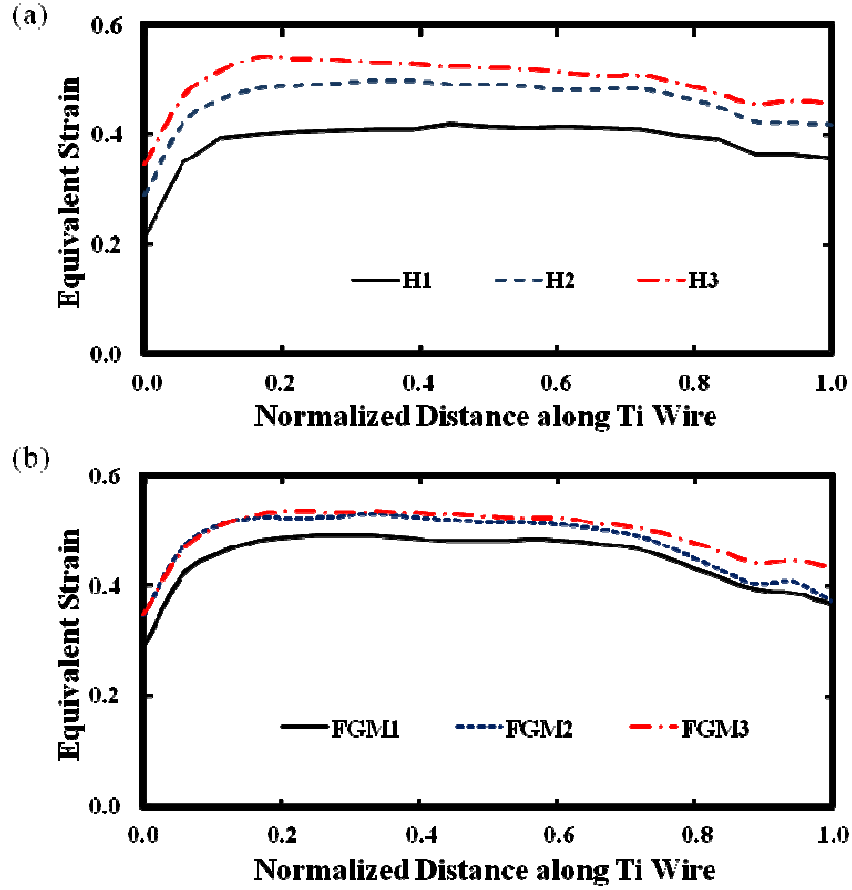
Fig. 2.7 Variation of equivalent strain along Ti: (a) embedded into homogeneous matrix and (b) embedded into composite matrix.

2.3.3 Effect of Die Geometry

The amount of strain in the specimen deformed by ECAP strongly depends on the shape of the die channel. In order to study this effect, an angle $\phi = 90°$ and different outer fillet radii R were considered. Also, the strain distributions of Ti in the specimen prepared using an ECAP die with an outer fillet radius R = 5.15 mm with $\phi = 90°$, $\phi = 105°$, and $\phi = 120°$ were studied.
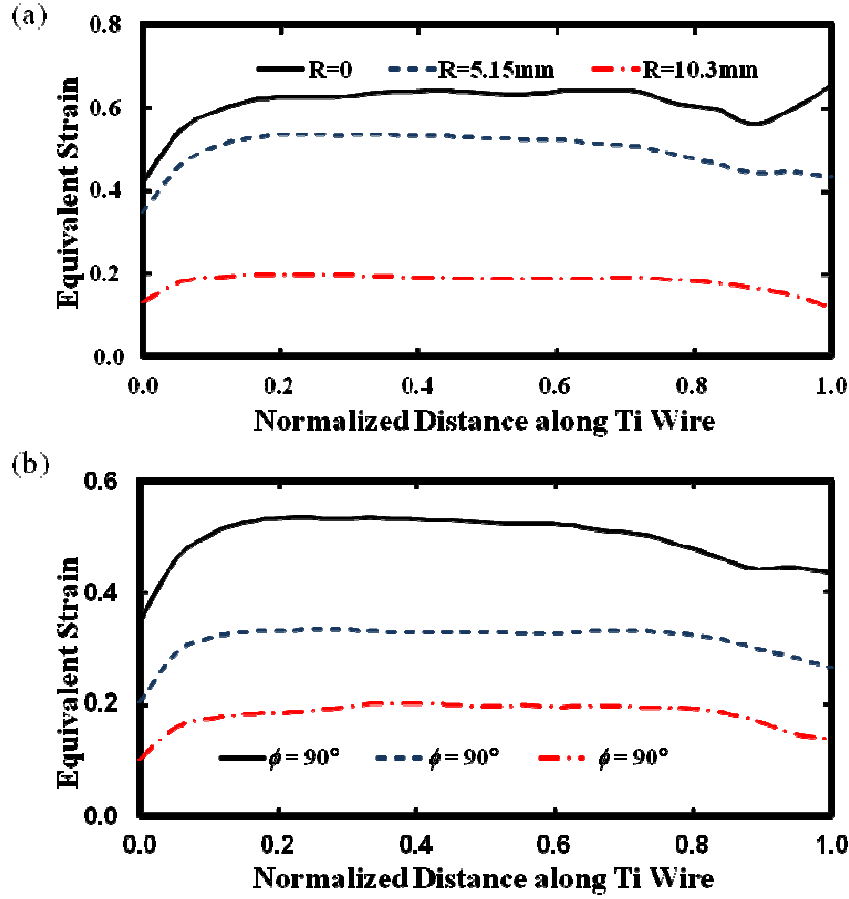
19

Fig. 2.8 Variation of equivalent strain along Ti embedded into FGM3: (a) with different outer fillet radii, R and (b) with different die angles, ϕ.

Figures 2.8(a) and (b) show the variation of equivalent strain along Ti with different die outer filler radii, R, and die angle, ϕ, respectively. When the angle of the die channel is fixed, the strain induced in Ti is increased by reducing R. On the other hand, a die with ϕ increment reduces the strain induced in Ti. From these results, it is found that the strain of Ti is controlled by die geometry.

Average equivalent strain, ε_{ave}, and coefficients of variance of the equivalent strains, *CV*, along Ti were calculated for each specimen. For comparison, only Ti embedded into

H2 and FGM3 at different die outer fillet radii, R, and die angles are shown in Table 2.2. The strain inhomogeneity decreases as the die outer fillet radii or die angle decreases.

Table 2.2 Average equivalent strain $\varepsilon_{\mathrm{ave}}$ and coefficient of variance of the equivalent strain CV (Eq. (2.4)) along Ti embedded into H2 and FGM3.

ϕ (°)	R (mm)	H2		FGM3	
		$\varepsilon_{\mathrm{ave}}$	CV	$\varepsilon_{\mathrm{ave}}$	CV
90	0	0.564	0.108	0.605	0.089
90	5.15	0.459	0.110	0.493	0.102
90	10.3	0.164	0.145	0.178	0.133
105	5.15	0.281	0.109	0.313	0.107
120	5.15	0.156	0.158	0.179	0.148

2. 4 Conclusions

FEM analysis is successfully carried out in order to investigate the deformation of a difficult-to-work material during the single ECAP pass at ambient temperature. It is possible to induce SPD into the difficult-to-work material at ambient temperature using the proposed technique. The selection of the host material is very important. In the case of SPD of Ti, an Al-based alloy or Al-based FGM should be selected as the host material. Apart from that, the position for embedding the difficult-to-work material and the die geometry are important factors for its SPD. For SPD of Ti using ECAP, it is suggested that Ti is embedded in the middle of the Al-based FGM host material and that an ECAP die with an outer fillet radius R = 5.15 mm and ϕ = 90° is used.

References

1) V. M. Segal, V. I. Reznikov, A. E. Drobyshevski, and V. I. Kopylov: Russ. Metall. **1** (1981) 99.

2) R. B. Figueiredo, P. R. Cetlin, and T.G. Langdon: Acta Mater. **55** (2007) 4769.

3) S. L. Semiatin, V. M. Segal, R. E. Goforth, N. D. Frey, and D. P. DeLo: Metall.Mater. Trans. A **30** (1999) 1425.

4) I. Kim, W. S. Jeong, J. Kim, K. T. Park, and D. H. Shin: Scr. Mater. **45** (2001) 575.

5) D. H. Shin, I. Kim, J. Kim, Y. S. Kim, and S. L. Semiatin: Acta Mater. **51** (2003) 983.

6) A. Balakrishnan, B. C. Lee, T. N. Kim, and B. B. Panigrahi: Trends Biomater. Artif. Organs **22** (2008) 54.

7) A. Balyanov, J. Kutnyakova, N. A. Amirkhanova, V. V. Stolyarov, R. Z. Valiev, X. Z. Liao, Y. H. Zhao, Y. B. Jiang, H. F. Xu, T. C. Lowe, and Y. T. Zhu: Scr. Mater. **51** (2004) 225.

8) G. I. Raab, E. P. Soshnikova, and R. Z. Valiev: Mater. Sci. Eng. A **387-389** (2004) 674.

9) S. Jamian, Y. Watanabe, H. Sato, and E. Miura-Fujiwara: presented at 20th Functional Graded Material Symp. (FGM2009), 2009.

10) Y. L. Yang and S. Lee: J. Mater. Process. Technol. **140** (2003) 583.

11) Y. Iwahashi, J. Wang, Z. Horita, M. Nemoto, and T. G. Langdon: Scr. Mater. **35** (1996) 143.

12) S. Li, M. A. M. Bourke, I. J. Beyerlein, D. J. Alexander, and B. Clausen: Mater. Sci. Eng. A **382** (2004) 217.

13) C. J. Luis, P. Gonzalez, and Y. Garces: J. Mater. Process. Technol. **143-144** (2003) 506.

14) H. S. Kim, M. H. Seo, and S. I. Hong: J. Mater. Process. Technol. **113** (2001) 622.

15) H. S. Kim, S. I. Hong, and M. H. Seo: J. Mater. Res. **16** (2001) 856.

16) V. Patil Basavaraj, U. Chakkingal, and T. S. Prasanna Kumar: J. Mater. Process. Technol. **209** (2009) 89.

Chapter 3

Experimental Study on Severe Plastic Deformation of Ti by Novel Equal-Channel Angular Pressing

3.1 Introduction

Equal-channel angular pressing (ECAP) process is preferred because a large plastic strain can be induced without any change in cross-sectional shape of the billet. Because of this, the deformation for the specimen can be repeated for huge strains. The multiple passes make it possible to induce different strains depending on the processing route [1−3]. The processing routes involved are, route A (no rotation), route B_A (90° back and forth rotation between passes), route B_C (90° in the same direction between passes), and route C (180° in the same direction between passes). Therefore, ECAP can induce huge strain by controlling the processing route.

However, severe plastic deformation (SPD) of Ti and Ti alloys at ambient temperature by ECAP is very difficult due to their ductility [1]. When Ti and Ti alloys are deformed by ECAP, the ECAP processing is carried out under high temperatures [1, 3−10]. This is because Ti and Ti alloys are difficult to deform due to hexagonal close packed (hcp) structure [1, 5]. In previous studies, the ECAP process for Ti has been performed under elevated temperatures up to 450 °C and it has been suggested that the lowest temperature for the successful deforming of Ti is 200 °C [7]. These studies show that it is very difficult to deform Ti by ECAP at ambient temperature.

Several recent reports have demonstrated that it is possible to deform Ti through multiple passes of ECAP at ambient temperature by increasing the channel angle up to 120°, under the processing speed of 2 mm/s [11−13]. For ECAP carried out in these studies, a special graphite lubricant containing ~15% MoS_2 powder was used. Based on these studies, it was reported that Ti was successfully processed through up to eight passes with route B_C. On the other hand, the authors have proposed an alternative

technique in processing Ti by ECAP at ambient temperature [14]. The proposed technique is the deformation of Ti by embedding a Ti wire into an easy-to-work material. In previous investigations, the deformation of Ti embedded in two different kinds of host material, namely homogeneous Al alloy and Al-based functionally graded material (FGM) with single-pass ECAP was carried out by the finite element method (FEM). Moreover, different positions of Ti embedded in the host material and different die geometry were considered. Based on the FEM results, an Al-based FGM matrix with the higher-strength alloy on the inner side was found to be a good host material. To reduce strain inhomogeneity along Ti, it has been suggested that Ti is embedded in the middle part in the host material and that an ECAP die with an outer fillet radius $R = 5.15$ mm and the two intersecting channels meeting at an angle 90° is used [14]. However, the workability of this technique is still questionable as no experimental work has been carried out so far. Moreover, the FEM was carried out only for a single ECAP pass and no data are available for multiple passes.

In this study, an experimental work using novel technique is carried out. Ti wire is tightly encapsulated in a hollow of host material made of Al-based FGM. ECAP is performed under route A for up to eight passes. Effects of the ECAP process and the host material on the microstructure and the hardness of Ti are discussed.

3.2 Experimental Procedure

3.2.1 Preparation of FGM billet

Figure 3.1 shows a schematic illustration of the FGM billet used in this work. The annealed Ti is embedded in the middle of the host material. Pure Ti (99.5%) with a diameter of 1.5 mm and a length of 20 mm is annealed at 800 °C for 5 min using a vacuum furnace. Pure Al (99.99%) and Al-Al$_3$Ti alloys are chosen as an outer layer and inner layer of the host materials, respectively.
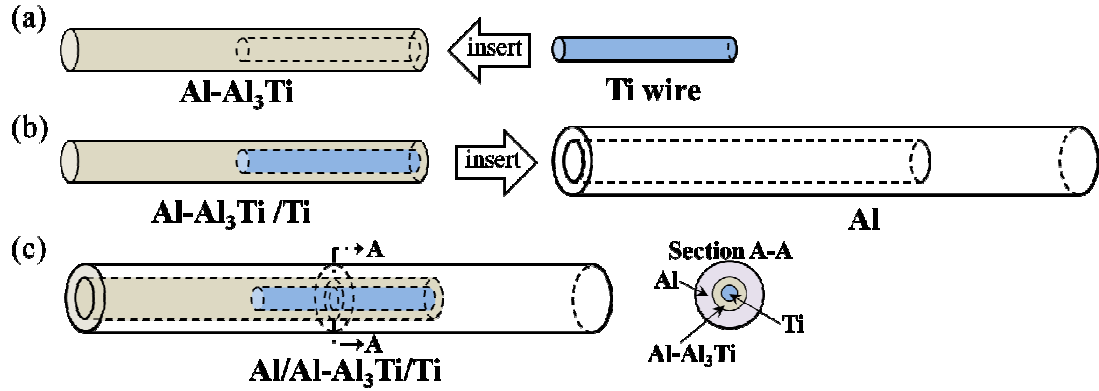
24

Fig. 3.1 A schematic illustration showing the assembly steps in preparing the FGM billet with stepwise gradient in strength: (a) Ti wire is inserted into a hole in the Al-Al$_3$Ti alloy rod. (b) The Al-Al$_3$Ti/Ti composite is inserted into a hole in the pure Al rod. (c) The FGM billet is fabricated.

FGM billets having 5, 11, and 21 vol% of Al$_3$Ti in Al-Al$_3$Ti alloy rod are prepared and designated as FGM1, FGM2, and FGM3, respectively. A rod-shaped ECAP billet of pure Al matrix with a diameter of 10 mm and a length of 60 mm is prepared by casting at 750 °C and machining. For the inner layer of the host material, Al-Al$_3$Ti alloy rods with a diameter of approximately 12 mm and a length of 140 mm are prepared by casting at 800 °C (for Al-5 vol% Al$_3$Ti) and 850 °C (for Al-11 vol% Al$_3$Ti). For the Al-21 vol% Al$_3$Ti rod, the Al-21 vol% Al$_3$Ti ingot was heated up to 850 °C and kept for one hour in argon atmosphere. The as-cast and annealed Al-Al$_3$Ti alloy rods are machined into a rod dimension with a diameter of 5 mm and a length of 40 mm each. A narrow hole with 5 mm in diameter and 40 mm in depth is drilled into an edge surface of pure Al. A hole with 1.5 mm in diameter and 20 mm in depth is drilled into an edge surface of Al-Al$_3$Ti alloy rods. The FGM billet is prepared by inserting an annealed Ti wire into a hole in the Al-Al$_3$Ti alloy rod (Fig. 3.1(a)). Then, both the Ti wire and the Al-Al$_3$Ti rod are press-fitted into a hole in the pure Al rod as shown in Fig. 3.1(b). By this method, an FGM billet with a gradient in strength can be obtained (Fig. 3.1(c)).

3.2.2 ECAP Process

The FGM billets are subjected to ECAP using a die with geometry shown in Fig. 3.2. Each billet is pressed at ambient temperature and under pressing speed of 4 mm/min. Graphite oil is used as lubricant to minimize friction between the inner surface of the die channel and the billet. ECAP are performed under route A for two and eight passes.
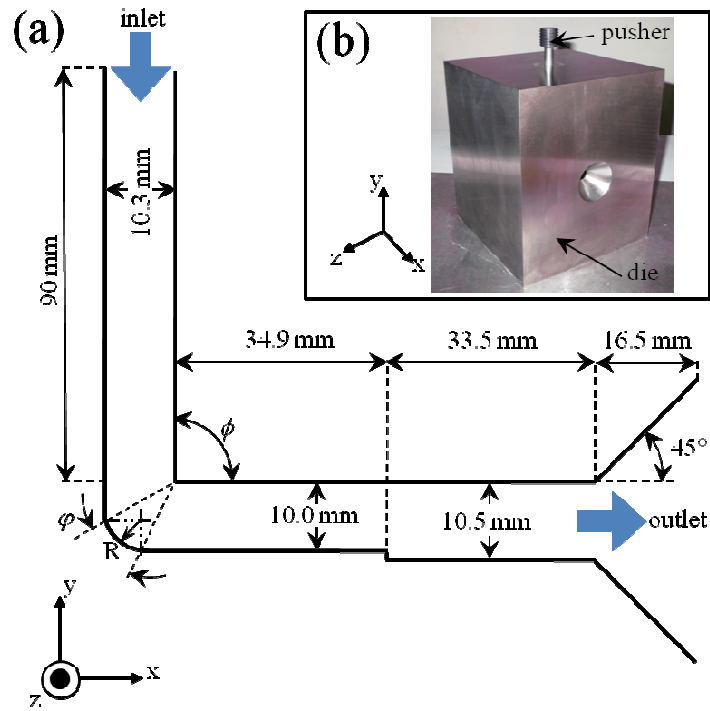

Fig. 3.2 (a) Schematic of ECAP die channel geometry featuring the die angle ϕ, the outer corner angle φ, and the outer fillet radius, R. (b) A photograph of the ECAP die and the pusher.

3.2.3 Characterization

The ECAPed specimens are cut along the main axis of the billet about 10 mm in length at the middle of the ECAPed specimen in the parallel section as shown in Fig. 3.3. These ECAPed specimens for evaluation are polished with emery paper and Al_2O_3 suspension. The samples are etched by an etchant of 0.5% HF and 99.5% H_2O. Microstructural

26

characterization is done by scanning electron microscope (SEM) and optical microscope (OM).
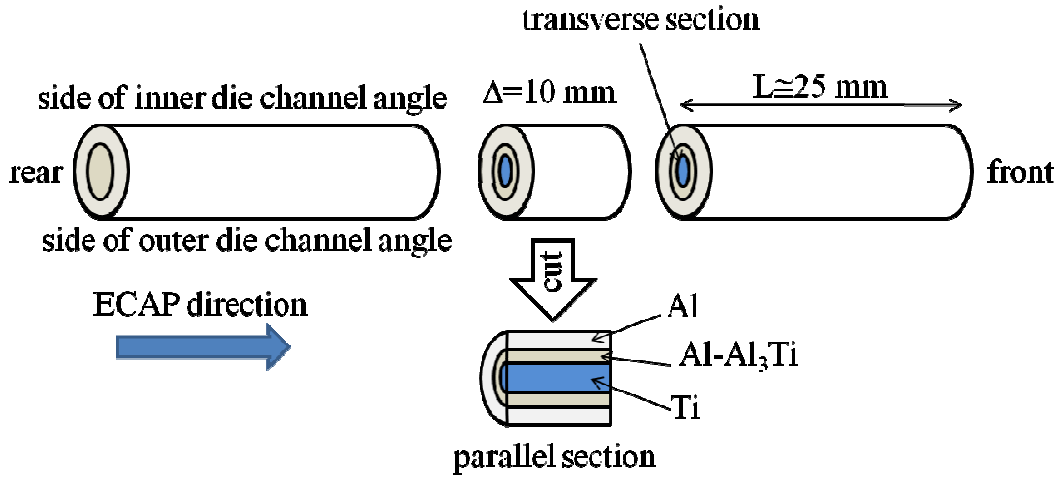

Fig. 3.3 Specimen for microstructural characterization and microhardness test.

Microhardness of as-annealed Ti and ECAPed Ti is measured using a Vickers microhardness tester under the load of 200 g for 30 s. Compression tests are carried out at ambient temperature. Cylindrical samples with a diameter of 10mm and a length of 10 mm are cut from as-cast pure Al and Al-Al$_3$Ti alloys for the compress tests. A strain rate of 6.6 x 10^{-3} s^{-1} is used. At least, three samples are tested for each material.

3.3 Results and Discussion
3.3.1 FGM Billets before ECAP
Three FGM billets with stepwise gradient in strength have been prepared. Figure 3.1(c) shows the illustration of the FGM billet. Each FGM billet was prepared with the highest-strength material (Ti wire) as the core, followed by Al-Al$_3$Ti alloy in the middle, and pure Al as the outer layer. The difference between these three billets is the volume fraction of Al$_3$Ti particles in Al-Al$_3$Ti. Table 3.1 shows the results of compression tests and microhardness measurements of each material used in fabricating the FGM billets. The 0.2% proof stress and the hardness increase with the increase in volume fraction of

Al$_3$Ti particles in Al-Al$_3$Ti alloy. The difference between these two mechanical properties of Al, Al-Al$_3$Ti alloys, and Ti make the stepwise gradient in strength of the FGM billets. The increments in the 0.2% proof stress and the hardness with increase in volume fraction of Al$_3$Ti particles in Al-Al$_3$Ti alloy indicate differences between FGM1, FGM2, and FGM3.

Table 3.1 Mechanical properties of FGM billet components.

Material	0.2% Proof Stress (MPa)	Hardness (Hv)
Outer layer :		
Pure Al	29	21
Middle layer:		
Al-5 vol% Al$_3$Ti alloy	47	25
Al-11 vol% Al$_3$Ti alloy	62	33
Al-21 vol% Al$_3$Ti alloy	73	38
Core:		
Ti	-	150

Figures 3.4(a), (b) and (c) are SEM micrographs showing the microstructure of Al-Al$_3$Ti in FGM1, FGM2, and FGM3, respectively. Al$_3$Ti particles in these FGMs are platelet in shape [15] and homogeneously distributed. Figures 3.5(a), (b) and (c) show the backscatter electron (BE) and secondary electron (SE) micrographs of annealed Ti and the OM macrograph of as-cast pure Al, respectively. The average grain size of as-annealed pure Ti and Al was approximately 40 µm and 700 µm, respectively.
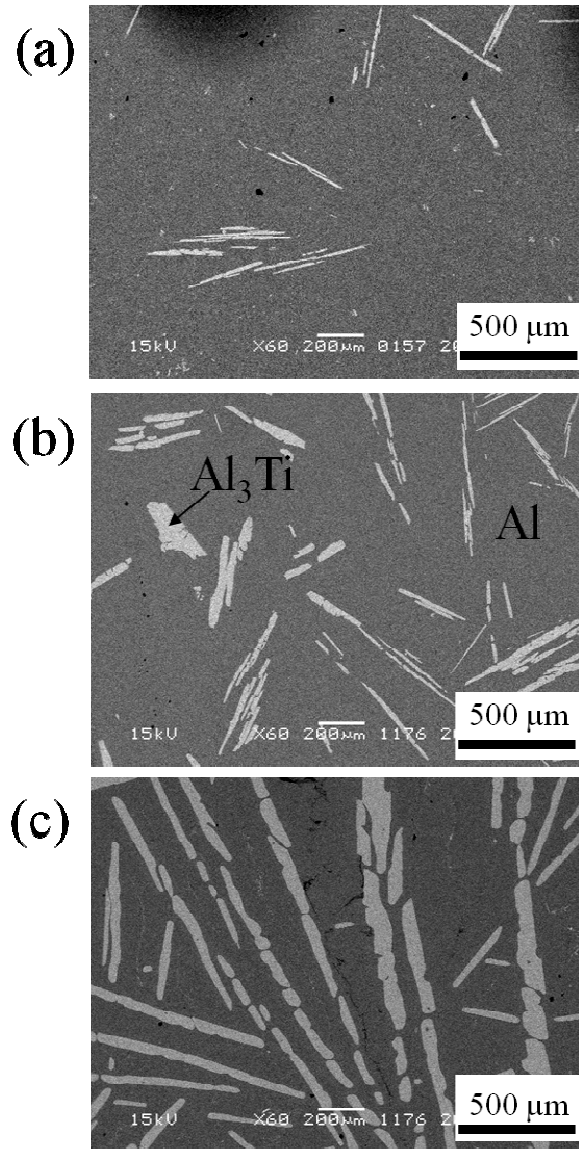
Fig. 3.4 The SEM micrographs of as-cast Al-Al$_3$Ti alloys: (a) 5vol% Al$_3$Ti, (b) 11vol%
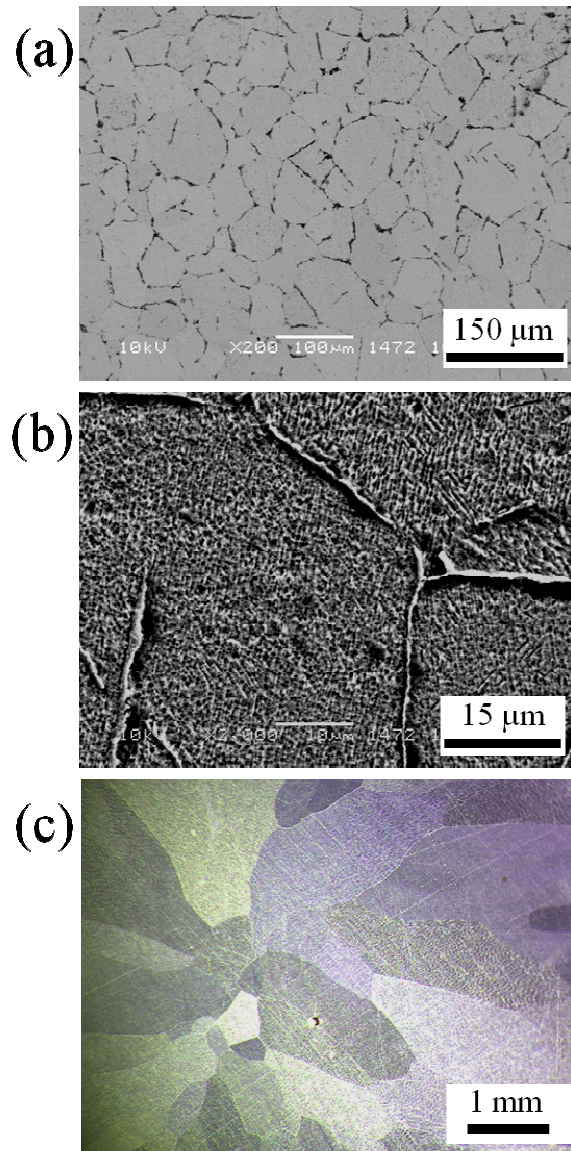Al$_3$Ti, and (d) 21vol% Al$_3$Ti.

Fig. 3.5 The SEM micrographs of as-annealed Ti: (a) backscatter electron (BE) image and (b) the magnified secondary electron (SE) image. (c) The OM macrograph of as-cast pure Al.

3.3.2 Change of Microstructure of Sample Deformed by ECAP

Figure 3.6 shows a composite billet shape before and after ECAP. Figures 3.6(b) and (c) are samples ECAPed for two passes and eight passes, respectively. As can be observed, only few small cracks exist on the billet surface after ECAP, even after eight passes. Thus, it is possible to continue ECAP process more than eight passes by the proposed technique.
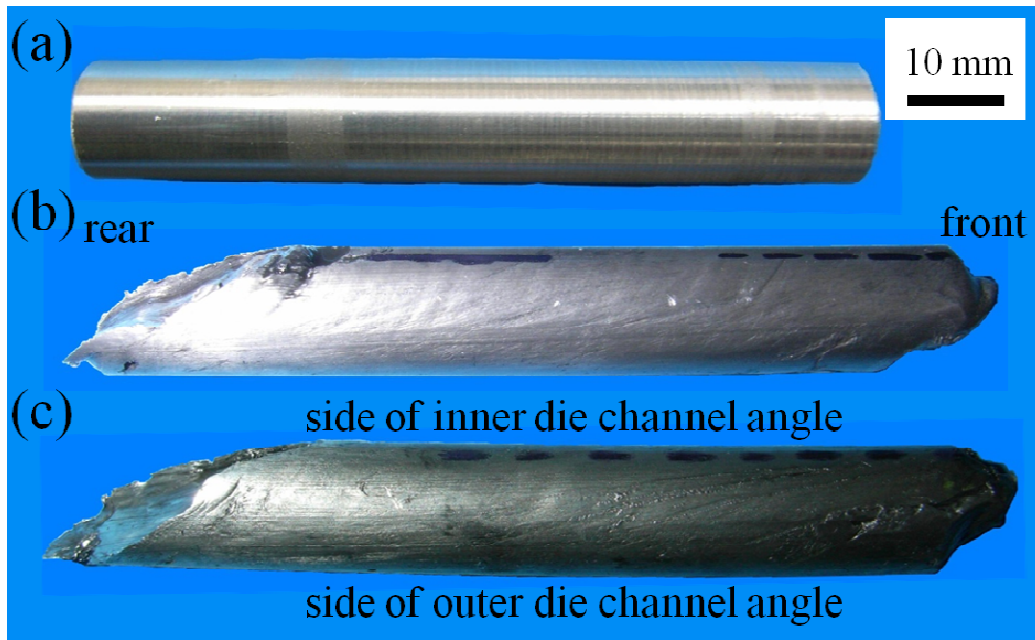

Fig. 3.6 Appearance of the FGM billets: (a) before ECAP, (b) after two passes, and (c) after eight passes.

3.3.3 Microstructural Characterization

The OM photograph in Fig 3.7(a) shows a typical macroscopic image of the parallel section of ECAPed FGM billet except for FGM3 after ECAP at eight passes. As can been seen, Ti is straightly embedded into Al-Al$_3$Ti alloy. Small cracks are observed in Al-Al$_3$Ti alloy and at the interface between Ti and Al-Al$_3$Ti alloy as well as between Al-Al$_3$Ti alloy and Al. Figures 3.7(b) and (c) show the macroscopic images of the parallel section and the transverse section of FGM3 after 8 ECAP passes, respectively. Ti is

broken into small segments and many cracks are observed. The size of cracks is relatively bigger than the cracks observed in other ECAPed FGM billets.
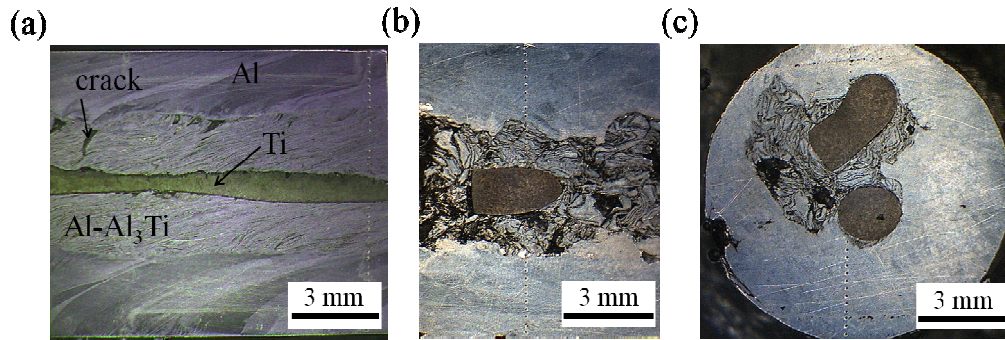

Fig. 3.7 The macroscopic image of ECAPed billets: (a) the parallel section of FGM2 after two passes; (b) and (c) the parallel and the transverse section of FGM3 after eight passes, respectively.

SEM micrographs in Figs. 3.8(a) and (b) show the microscopic structure of Ti in FGM1 after two passes and eight passes, respectively. Although no twins were observed in the as-annealed state (Figs. 3.5(a) and (b)), they are observed in ECAPed billets. The formation of twins increases as the number of passes increases. The formation of twins plays a major role in the plastic deformation of Ti by ECAP. This phenomenon is also observed on Ti encapsulated in FGM2 and FGM3 as shown in Figs. 3.8(c) to (f), respectively. It is shown that Ti wire is well deformed by the proposed technique. The deformation mechanisms of Ti processed by ECAP are well explained in previous studies [1−5]. According to those studies, during the first pass for pure Ti, twin deformation take place initially and changing to dislocation slip mechanism afterwards. Comparing the microstructure of Ti encapsulated in FGM1, FGM2, and FGM3 after ECAP at two passes (Figs. 3.8(a), (c), and (e)) and eight passes (Figs. 3.8(b), (d), and (e)), the largest volume of twins are observed on Ti in FGM1. The difference of the volume of twins on Ti encapsulated in FGM1, FGM2, and FGM3 is the result of having different types of host materials.
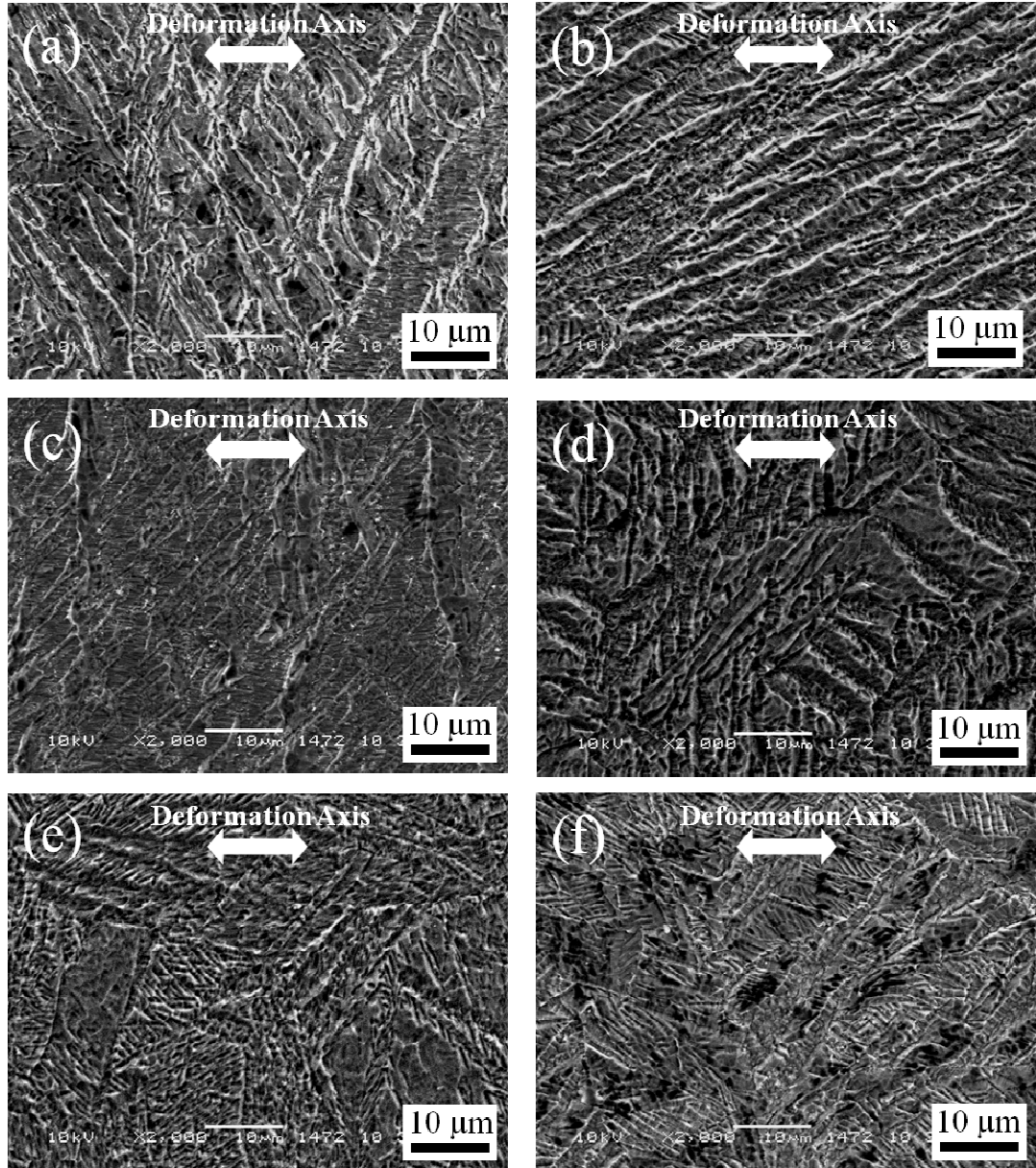
32

Fig. 3.8 The SEM micrographs of Ti: (a) and (b) in FGM1, (c) and (d) in FGM2, and (e) and (f) in FGM3 after two passes and eight passes, respectively.

There is a possibility of an existence of a new phase after SPD of composite material. Energy-dispersive X-ray (EDX) analysis is performed with focus on the interface of Ti and Al-Al$_3$Ti alloys. Figure 3.9(a) shows the SE image of the interface between Ti and Al-Al$_3$Ti alloy of FGM1 after eight passes. Figures 3.9(b) through (d) show the BE image and the corresponding Ti distribution and Al distribution maps. Although the cracks are clearly observed at the interface between Ti and Al-Al$_3$Ti alloy, no new phase is formed.
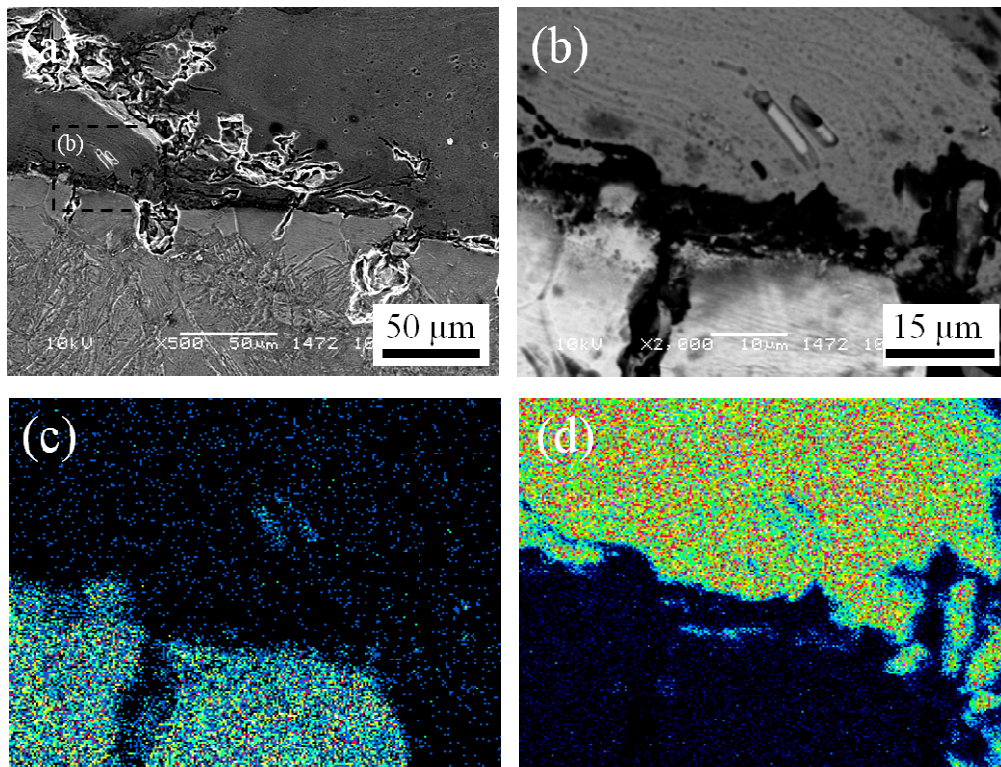

Fig. 3.9 The micrograph of interface between Ti and Al-Al$_3$Ti alloy: (a) SE image at low magnification and (b) the magnified BE image with Ti and Al distribution maps in (c) and (d), respectively.

It is interesting to investigate the microstructure of the host material since it has a strong effect on the deformation of Ti [14]. Figure 3.10 shows the SEM micrographs of Al-Al$_3$Ti alloys after ECAP for FGM1, FGM2, and FGM3. After ECAP, the initial Al$_3$Ti

platelet particles (Fig. 3.4) that are severely fragmented and granular Al$_3$Ti particles have been observed. The evolution of Al$_3$Ti particles are investigated by measuring the aspect ratio and the particle length using an image analysis software. The aspect ratio is defined as the ratio of the maximum and the minimum lengths of the rectangle with the smallest area that can be drawn around the particle.
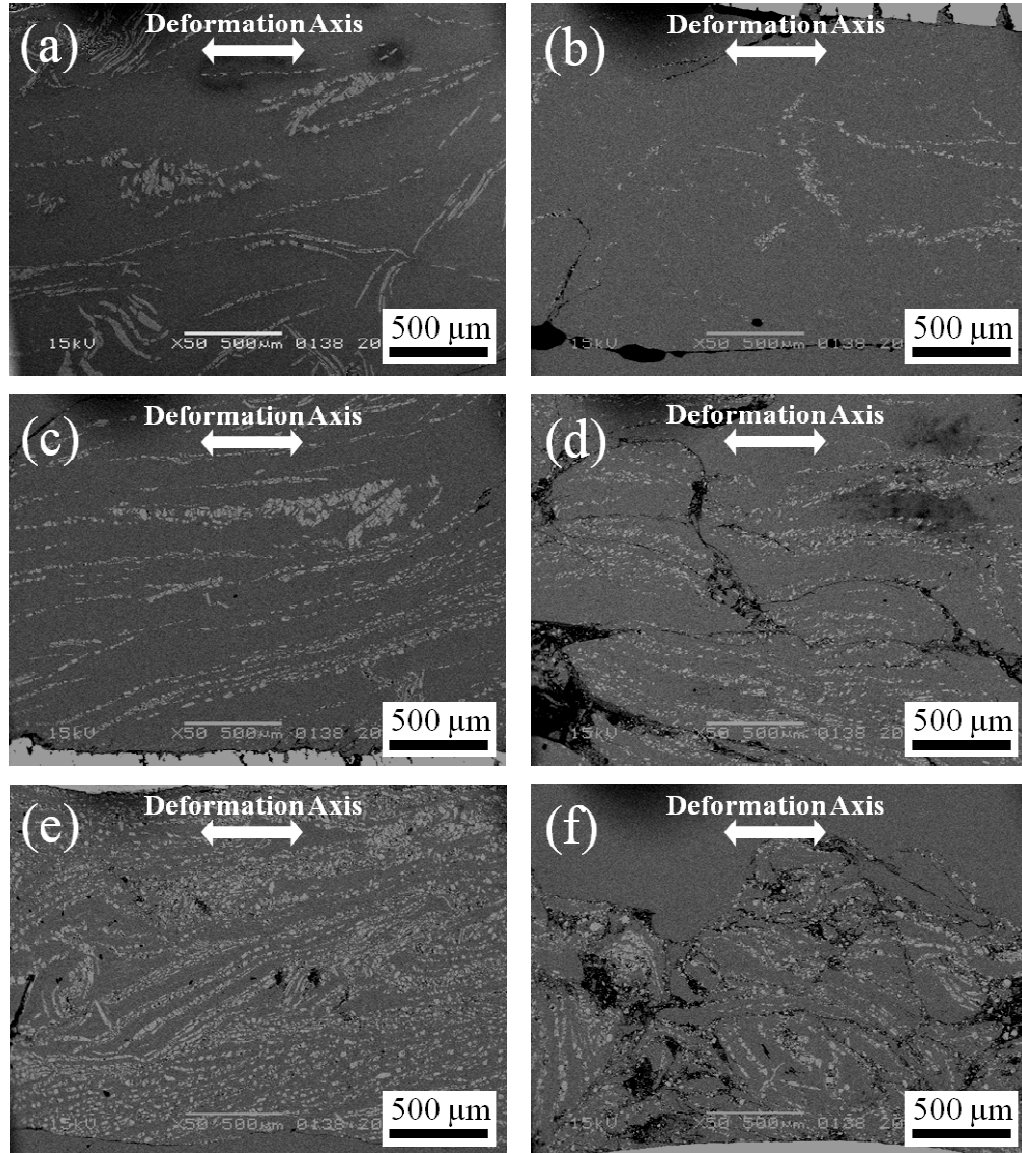

Fig. 3.10 The SEM micrographs of Al-Al$_3$Ti alloys: (a) and (b) in FGM1, (c) and (d) in FGM2, and (e) and (f) in FGM3 after two passes and eight passes, respectively.

Table 3.2 The average aspect ratio (AR) and particle length (PL) of Al$_3$Ti particles before and after ECAP.

Specimen	0 pass		2 passes		8 passes	
	AR	PL	AR	PL	AR	PL
FGM1	11.86	115.20	2.59	10.69	2.52	5.19
FGM2	8.19	104.24	2.22	6.10	2.21	4.40
FGM3	6.04	179.63	2.39	4.88	2.22	4.05

Table 3.2 shows average aspect ratio and particle length of Al$_3$Ti before and after ECAP for FGM1, FGM2, and FGM3. It is noted that the aspect ratio of Al$_3$Ti particles in all specimens decreased with increasing the number of ECAP passes. Simultaneously, the length of Al$_3$Ti decreases when the billet is deformed by ECAP. These results are in accordance with the results of previous studies on processing by ECAP for particle-reinforced Al composites [16−19]. Regardless of the different initial size of Al$_3$Ti particles due to the different processing conditions in preparing Al-Al$_3$Ti alloys before ECAP, the average aspect ratio of Al$_3$Ti is almost the same after ECAP at eight passes. However the reduction in the Al$_3$Ti particles size is significantly different. Zhang et al. [17] reported that the number of fine Al$_3$Ti particles still increases significantly with ECAP passes even after 15 passes.

Considering the deformation of Ti in billets by ECAP, FGM3 with the highest mechanical properties in Al-Al$_3$Ti alloy was expected to give the highest deformation to Ti. However, as mentioned above, the largest volume of twins in Ti is observed in FGM1. From Fig. 3.10, it is seen that the Al$_3$Ti particles that enhance the strength of as-cast Al-Al$_3$Ti are severely fragmented. As a result, many small cracks/dimples are generated between the particles and the Al matrix. The number of crack increases with the increase in the number of ECAP passes. Moreover, the size of crack increases with the increase in the number of ECAP passes. These cracks provide enough space for Ti to bend or "move" to accommodate the strain induced by ECAP process. Therefore, the

deformation of Ti in the FGM2 and the FGM3 is less than the FGM1. It is important that the initial small granular shape of Al_3Ti particle be considered.

Macroscopic observation on Al in FGM billets are shown in Fig. 3.11. Figures 3.11(a) and (b) show the typical macrographs of Al in FGM billet after two passes and eight passes, respectively. Initially, the as-cast Al comprises of large grains with an average grain size of 700 μm. After two passes, the grains are elongated (Fig. 3.11(a)) and after eight passes, the shear bands disappear and fine equiaxed grains are formed (Fig. 3.11(b)). The good ductility of Al facilitated the deformation of FGM billet by ECAP. The Al prevented the inner layer (Al-Al_3Ti and Ti) to break (cut at the edge) after the several number of ECAP passes. Therefore it increases the possibility to continue further the ECAP process.

As demonstrated above, not only the strength of host materials, but also the initial shape of Al_3Ti particles plays an important role in deforming Ti by the proposed technique. Instead of using the platelet-shaped Al_3Ti particles, the granular-shaped Al_3Ti particles should be used or the Al-Al_3Ti alloy should be replaced with single phase interlayer material such as Cu-Ni alloy. The granular shape of Al_3Ti particle can be obtained by carrying out the ECAP process first on as-cast Al-Al_3Ti and then re-cast at a temperature lower than the melting point of Al_3Ti. In addition, a selection of the particle-reinforced Al composite in this study is interesting since the continuous gradient in strength of FGM billet can be obtained by applying centrifugal force during casting [15].
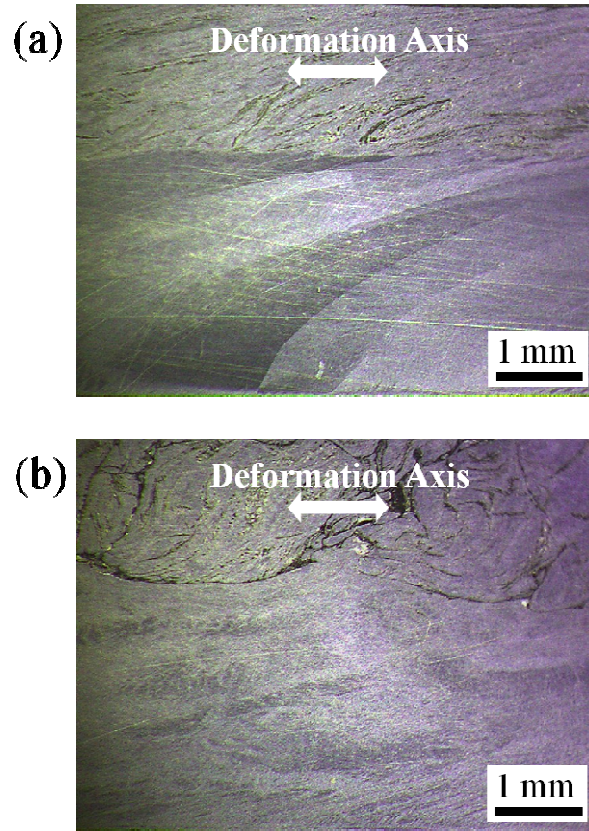
Fig. 3.11 The OM macrographs of Al in FGM2: (a) after two passes and (b) after eight passes.

3.3.4 Hardness

The average hardness values of Ti encapsulated in the FGM1, FGM2, and FGM3 after two passes and eight passes are listed in Table 3.3. It can be seen that the hardness value increases with the increase in the number of ECAP passes. The average hardness value of as-annealed Ti is 150 Hv. Comparing the hardness value of Ti as-annealed and after ECAP, there is significant enhancement in the hardness by ECAP. The measured hardness values are compared with the published data on pure Ti processed by ECAP in order to evaluate the effectiveness of the proposed technique. Figure 3.12 shows the variation of the hardness of Ti as a function of the number of ECAP passes from the earlier reports with different ECAP conditions [3, 8, 11−13].

Table 3.3 The Vickers hardness value, Hv of Ti and its equivalent number of ECAP passes (EP) according with earlier reports[3,8,11−13] after ECAP.

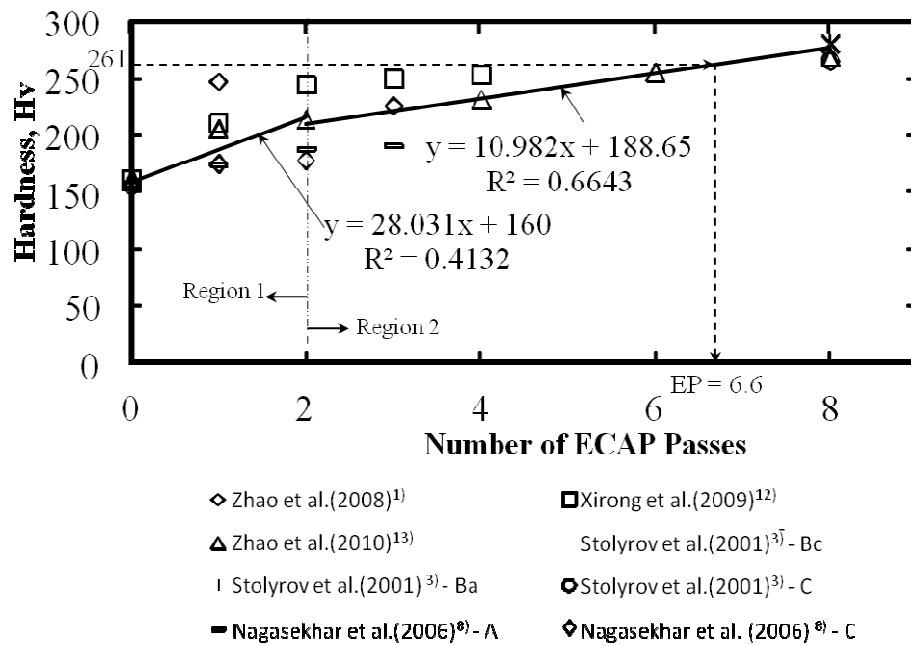| Specimen	2 passes		8 passes	
	Hv	EP	Hv	EP
FGM1	230	2.4	261	6.6
FGM2	227	2.3	235	4.2
FGM3	204	1.5	209	1.7

Fig. 3.12 A plot of hardness values versus number of ECAP passes obtained in earlier reports. Solid lines indicate the curve fit of the data in Region 1 and Region 2. Broken lines with arrows indicate an example of determination of the equivalent number of ECAP passes (EP).

39

The hardness of Ti as a function of the number of ECAP passes are divided into two regions, up to two passes and after two passes. Then, based on the data in each region, two curves are fitted as shown in Fig. 3.12. Comparing the measured hardness of Ti in this study with the earlier reports by using the two curve fits, the equivalent number of ECAP passes (EP) is determined as shown in Table 3.3. After two passes the equivalent number of ECAP passes for all FGM billets except for FGM3 is more than two passes. However, after eight passes, the equivalent number of ECAP passes for all FGM billets is less than the actual number of ECAP passes. This indicates that the proposed technique is effective in processing Ti by ECAP for the low numbers of ECAP passes. Although the ECAP process can be easily conducted at ambient temperature for higher number of ECAP passes, the increment of induced strain caused by it is not high.

3.4 Conclusions

The technique proposed in this study is a promising technique for SPD of Ti at ambient temperature and also can be applied to other difficult-to-work materials. The formation of twins and the increment of the hardness value in Ti by ECAP process are evidences that Ti can be deformed by the proposed technique. The stepwise gradient in strength of the Al-based FGM host material assists the deformation of Ti. The deformation of Ti depends on the properties of the host material. The Al prevents the inner layers (Al-Al$_3$Ti and Ti) to break (cut at the edge) after several ECAP passes. The existence of particles (platelet shape) in alloy (Al-Al$_3$Ti) makes it more brittle and more porous, resulting in increased the possibility of cracks.

References

1) I. Kim, W.S. Jeong, J. Kim, K.T. Park, and D. H. Shin: Scr. Mater. **45** (2001) 575.

2) Y. T. Zhu and T.C. Lowe: Mater. Sci. Eng. A **291** (2000) 46

3) V. V. Stolyarov, Y. T. Zhu, I. V. Alexandrov, T. C. Lowe, and R. Z. Valiev: Mater. Sci. Eng. A **299** (2001) 59.

4) S. L. Semiatin, V. M. Segal, R. E. Goforth, N. D. Frey, and D. P. Delo: Metall. Mater. Trans. A **30** (1999) 1425.

5) D. H. Shin, I. Kim, J. Kim, Y. S. Kim, and S. L. Semiatin: Acta Mater. **51** (2003) 983.

6) A. Balyanov, J. Kutnyakova, N. A. Amirkhanova, V. V. Stolyarov, R. Z. Valiev, X. Z. Liao, Y. H. Zhao, Y. B. Jiang, H. F. Xu, T. C. Lowe, and Y. T. Zhu: Scr. Mater. **51** (2004) 225.

7) G. I. Raab, E. P. Soshnikova, and R. Z. Valiev: Mater. Sci. Eng. A **387-389** (2004) 674.

8) A.V. Nagasekhar, U. Chakkingal, and P. Venugopal: J. Mater. Process. Technol. **173** (2006) 53.

9) R. B. Figueiredo, P. R. Cetlin, and T.G. Langdon: Acta Mater. **55** (2007) 4769.

10) A. Balakrishnan, B. C. Lee, T. N. Kim, and B. B. Panigrahi: Trends Biomater. Artif. Organs **22** (2008) 54

11) X. Zhao, W. Fu, X. Yang, and T.G. Langdon: Scr. Mater. **59** (2008) 542.

12) Y. Xirong, Z. Xicheng, and F. Wenjie: Rare Met. Mater. Eng. **38** (2009) 955.

13) X. Zhao, X. Yang, X. Liu, X. Wang and T.G. Langdon: Mater. Sci. Eng. A **527** (2010) 6335.

14) S. Jamian, H. Sato, E. Miura-Fujiwara, and Y. Watanabe: Jpn. J. Appl. Phys. **50** (2011) 01AJ06.

15) Y. Watanabe, H. Eryu, and K. Matsuura: Acta Mater. **49** (2001) 775.

16) Z. Zhang, Y. Watanabe, and I.S. Kim: Mater. Sci. Technol. **21** (2005) 708.

17) Z. Zhang, S. Hosoda, I.S.Kim, and Y. Watanabe: Mater Sci. Eng A **425** (2006) 55.

18) H. Sato, S. El-Hadad, O. Sitdikov, and Y. Watanabe: Mater. Sci. Forum **584-586** (2008) 971.

19) S. El-Hadad, H. Sato, and Y. Watanabe: Mater. Sci. Eng. A **527** (2010) 4674.

Chapter 4

A Numerical Crashworthiness Investigation of FGM Crash Boxes under Axial Quasi-static and Dynamic Loadings

4.1 Introduction

In automobile industry, much effort has been made to reduce the damage of vehicle and injury of passengers during an accident. A car is designed with energy-absorbing systems to reduce injury of car passengers in high speed-collisions and the damage of car in low-speed collisions [1]. One of the energy-absorbing systems in automobile is a crash box. A crash box, which is installed between a front bumper and a front side member of an automobile, is designed to be deformed in a predetermined mode and expected to be collapsed with absorbing crash energy prior to the other body part. The crashworthiness of the crash box is expressed in energy absorption, E, and specific energy absorption (SEA). The energy absorption is equal to the area of the crash load-displacement curve while specific energy absorption is defined as the amount of energy absorbed per unit mass crushed material [2−4]. Mainly the crashworthiness of crash box is affected by material properties, loading speed and geometrical dimensions [2, 5−7].

Conventionally, the car crash box is made from homogeneous steel sheet or aluminum extrusions [4−7]. In order to enhance the crashworthiness, a crash box is usually equipped with crash beads, designed with many ridge lines [8, 9] or filled with metal foams or honeycombs [10−14]. However, the weight of crash box equipped with crash beads or designed with many ridge lines will increase as the perimeter (circumferential length) of crash box cross-sectional shape increased. Meanwhile, the addition of metal foams or honeycombs obviously increases the weight of crash box. Nevertheless, the presence of the metal foams in crash box raises the idea to apply the concept of functionally graded materials (FGMs) in efforts to improve crashworthiness of a crash box [14]. Weight reduction of the structure is one of important issues in car design without reducing ability of crash energy absorption. Other important issues are

the need for higher stiffness and strength of the car body structure and cost reduction [15]. Therefore, multifunctional materials have begun to be used in the design of car.

Recently, functionally graded foam (FGF) materials have been investigated as energy absorber materials in crashworthiness applications [16, 17]. Sun et al. [14] introduced FGF fillers to fill thin-walled structures, aiming to improve crashworthiness. Their numerical simulations showed that the FGF material is superior to its uniform counterparts in overall crashworthiness. However, fabrication of an FGF material is uneasy. The fabrication method of FGF is based on investment casting replication of polymeric precursors which have been density-graded by non-uniform compression [18]. In this study, another design of FGM crash box is proposed. Namely the crash box made from stepwise material with strength gradient along longitudinal direction is obtained by dividing a homogenous structure into several segments and then conducting different heat treatment in each segment. A numerical crashworthiness investigation of the FGM crash boxes is carried out. Different FGM crash boxes with different stepwise strength gradient in longitudinal direction are designed, and their crash behaviors are analyzed by finite element method (FEM). The damage evolution is also considered in this analysis since the material may suffer damage and failure under crash loading conditions. Ignoring the material damages may lead over-predicts the load response [5]. The crash behavior of homogeneous crash box is also analyzed as reference. Two types of loadings are considered such as axial quasi-static and dynamic loading. The effects of the stepwise gradient in strength and the cross-sectional shape of crash box on the crash behavior are discussed.

4.2 FGM Crash Box

Figure 4.1 shows a set of schematic illustrations of the FGM crash box used in this work. The crash box was divided into several segments with the same size. Each segment was distinguished with its strength of the material to give stepwise strength gradient along longitudinal direction of crash box. Four different stepwise strength gradients were defined as shown in Figs. 4.2(a) to (d), namely, FGM1, FGM2, FGM3 and FGM4. Practically, such stepwise strength gradient can be obtained by dividing a homogeneous

43

metal tube into several segments and then conducting heat treatments with different conditions in each segment. Such stepwise strength gradient also can be obtained by stacking and assembling different metals tube together.

The material used in this study is an aluminum alloy EN AW-2024 T4. Density, Poisson's ratio and Young's modulus were assumed 2780 kg/m^3, 0.33 and 73.1GPa, respectively. The stress-strain curves and other relevant material properties as listed in Table 4.1 are obtained experimentally by Fujda et al. [19]. The material labels A, B, C and D indicate the initial state and annealing temperature of 520, 540 and 560 °C, respectively. The stress-strain curves are shown in Fig. 4.3, which were obtained by tensile tests carried out at room temperature at a constant strain rate of 2.5 x 10^{-4} s^{-1}. As for reference, the crash behavior of homogeneous crash boxes, namely, HA (the highest strength material, A) and HD (the lowest strength material, D), are also analyzed. The length of crash box, L, is 280 mm and the wall thickness, t_w, is 2 mm.

Length, $L = 280$mm
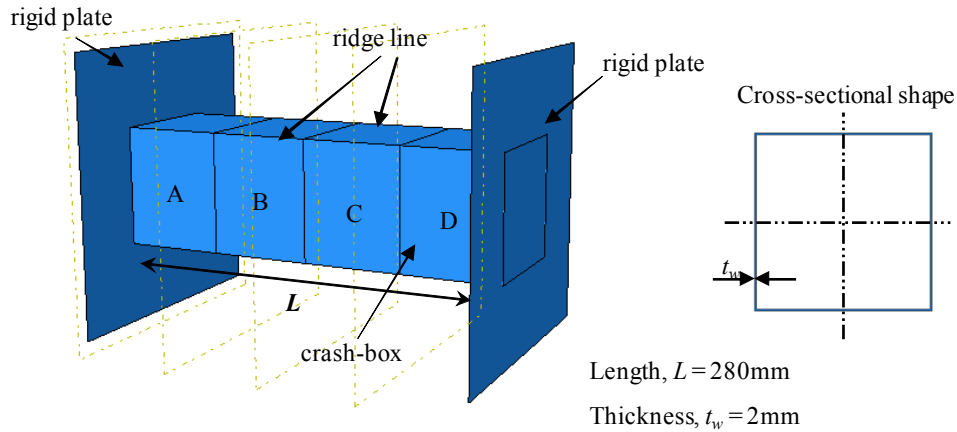
Thickness, $t_w = 2$mm

Fig. 4.1 A illustration of FGM crash box.

In order to study the crashworthiness behavior for different cross-sectional shapes, four simple cross-sectional shapes of crash boxes, which were considered in this study, i.e., circle, square, pentagon and hexagon as shown in Fig. 4.4. The simulations were only performed for material FGM1 in case of circle, pentagon and hexagon cross-sectional shape. All the simulations performed are listed in Table 4.2. Small letters 's', 'c', 'p' and 'h' at the front of crash box's name denote the cross-sectional shapes of crash boxes, i.e., square, circle, pentagon and hexagon, respectively. Meanwhile capital letter

'R' at the end of crash box's name denotes the inverse impact direction of FGM crash box.

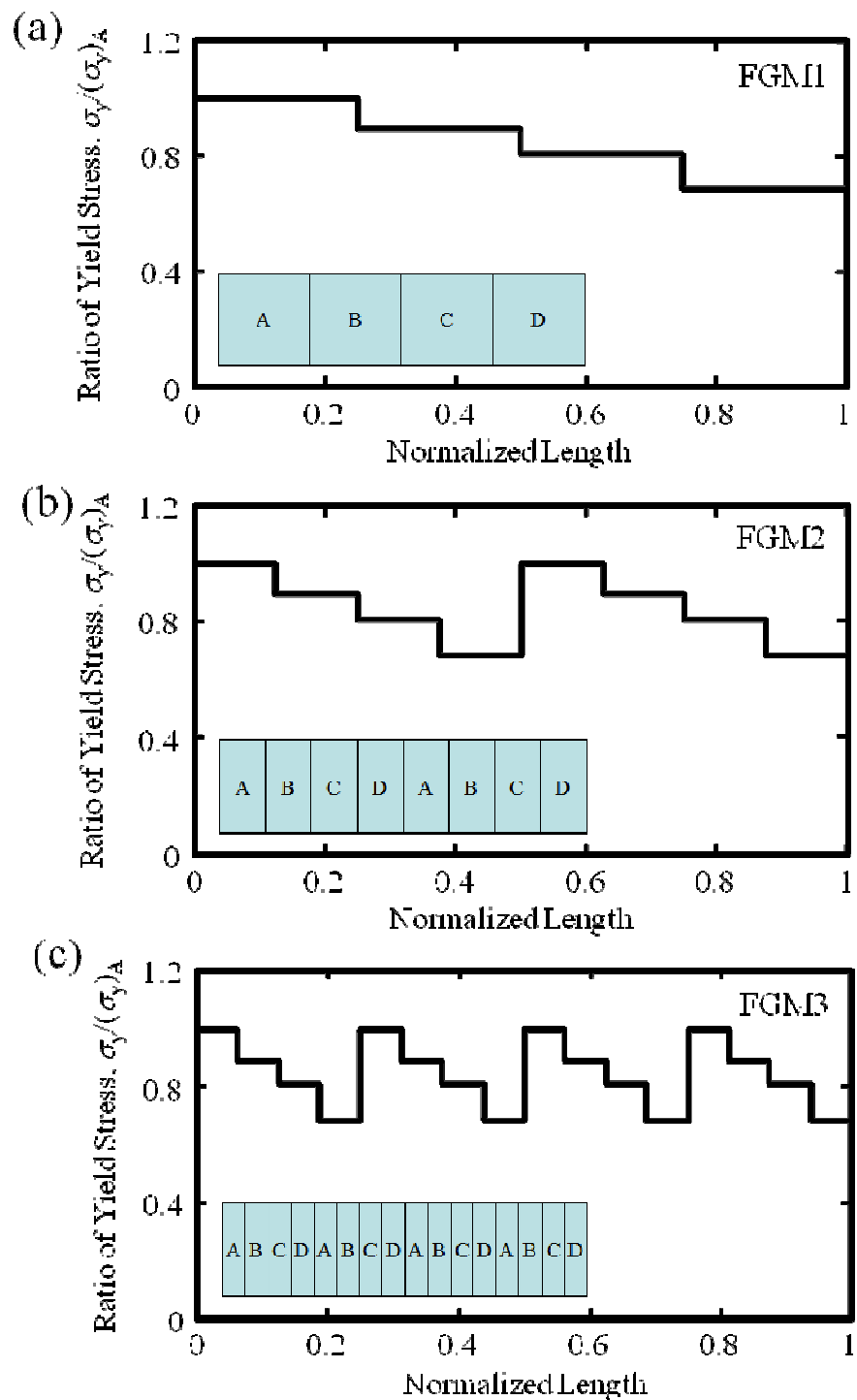(a) FGM1

(b) FGM2
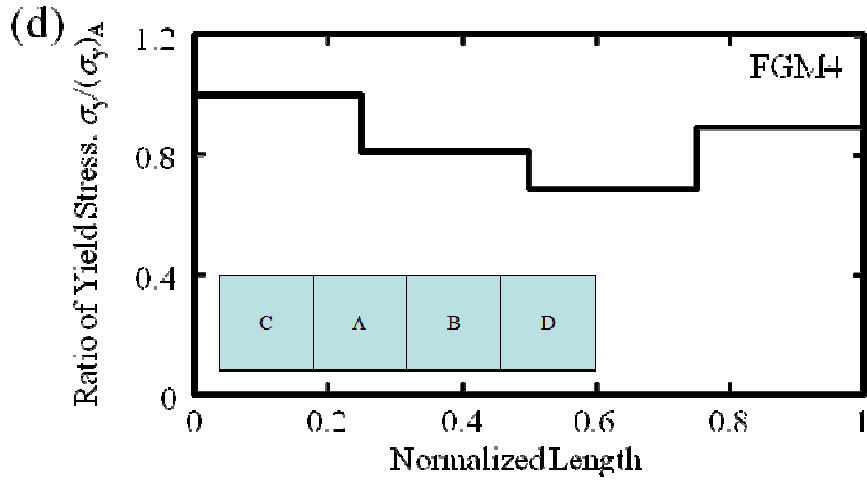
(c) FGM3

Fig. 4.2 (cont.)

Fig. 4.2 Distributions of yield stress ratio in a crash box along longitudinal direction: (a) FGM1, (b) FGM2, (c) FGM3, and (d) FGM4. A through D in each graph is present kinds of material shown in Table 4.1. $(\sigma_y)_A$ is the yield stress of material A.

Table 4.1 Material Properties [19]

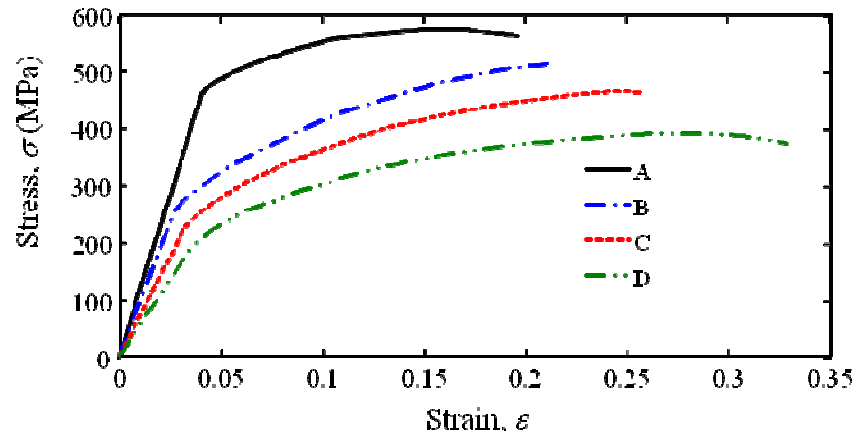| Label	A	B	C	D
State: Annealing Temperature	Initial	520°C	540°C	560°C
Ultimate tensile strength, σ_{uts}(MPa)	571	510	462	391
Yield Stress, σ_y (MPa)	464	259	237	209
Strain to failure (%)	14.5	16.1	19.3	25.8

Fig. 4.3 The stress-strain curves for EN AW 2024 T4 at initial state (A) and after heat treatment at 520°C (B), 540°C (C) and 560°C (D).
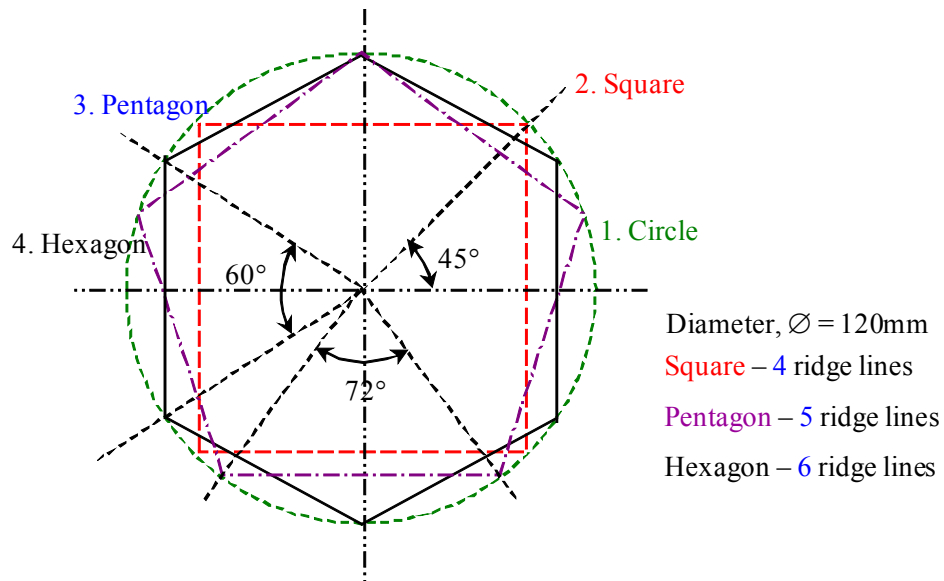

Fig. 4.4 The cross-sectional shape of FGM crash box.

Table 4.2 List of the FE simulations performed

Code	Material	Impact direction	Static/Initial Impact Velocity
sFGM1	FGM1	Front	
sFGM2	FGM2	Front	
sFGM3	FGM3	Front	
sFGM4	FGM4	Front	
sFGM1R	FGM1	Rear	quasi-static: 0.1m/s
sFGM2R	FGM2	Rear	dynamic:
sFGM3R	FGM3	Rear	15km/h
sFGM4R	FGM4	Rear	30km/h
			45km/h
sHA	A	Front	
sHD	D	Front	
cFGM1	FGM1	Front	
pFGM1	FGM1	Front	
hFGM1	FGM1	Front	

4.3 Finite Element Modeling

Simulation for crash behavior of crash box was carried out with the computer code ABAQUS explicit. The crash boxes were modeled using their complete dimensions, and the 4-node shell (S4R) element was selected for the mesh. The maximum size of element was set to be 5 mm. This size of mesh is the criteria recommended in automotive industries [5, 6, 13]. Two loading cases were considered, i.e., quasi-static and dynamic impact loading. The first case consists of a quasi-static compression configuration where the crash box was loaded in the axial direction with a constant speed of 0.1 m/s. In the second case, the crash box was subjected to a dynamic impact loading in the axial direction. A load of 500 kg impacted onto the front of crash box at an initial impact velocity. Three different initial impact velocities were considered, i.e., 15, 30 and 45 km/h.

The front and rear plates were considered to be rigid. The material of crash box was modeled as an elastic-plastic material. The material of crash box may fail due to one or a combination of following failure mechanism: ductile failure due to nucleation, growth and coalescence of voids; shear failure due to fracture within shear bands; and failure due to necking instabilities [20, 21]. The detail explanation of these damage mechanisms and the damage models as well as its implementation in simulation can be obtained from Hooputra et al. [20] and ABAQUS Manual [21]. In this study, the ductile damage, shear damage and Müschenborn-Sonne Forming Limit Diagram (MSFLD) were used to describe the material failure.

For a ductile damage initiation criterion, the equivalent plastic strain at the onset of ductile damage, $\bar{\varepsilon}_D^{pl}$ was assumed to be a function of the stress triaxiality and strain rate: $\bar{\varepsilon}_D^{pl}\left(\eta, \dot{\bar{\varepsilon}}^{pl}\right)$. Here $\eta = -p/q$ is the stress triaxiality, p is the pressure, q is the Mises equivalent stress, and $\dot{\bar{\varepsilon}}^{pl}$ is the equivalent plastic strain rate. For the shear damage initiation criterion, the equivalent plastic strain at the onset of shear damage, $\bar{\varepsilon}_S^{pl}$ was assumed to be a function of the shear stress ratio and strain rate: $\bar{\varepsilon}_S^{pl}\left(\theta_S, \dot{\bar{\varepsilon}}^{pl}\right)$. Here $\theta_S = (q + k_s p)/\tau_{max}$ is the shear stress ratio, k_s is a material parameter, and τ_{max} is the maximum shear stress. A typical value of k_s for aluminum is 0.3. The criterion for ductile and shear damage initiation, ω_D and ω_S, were met when the following conditions were satisfied:

$$\omega_D = \int \frac{d\bar{\varepsilon}^{pl}}{\bar{\varepsilon}_D^{pl}\left(\eta, \dot{\bar{\varepsilon}}^{pl}\right)} = 1 \text{ and } \omega_S = \int \frac{d\bar{\varepsilon}^{pl}}{\bar{\varepsilon}_S^{pl}\left(\theta_S, \dot{\bar{\varepsilon}}^{pl}\right)} = 1 \tag{4.1}.$$

Here ω_D and ω_S are state variables that increase monotonically with plastic deformation proportional to the incremental change in equivalent plastic strain. In the present study, the relationship between $\bar{\varepsilon}_D^{pl}$ and η and the relationship between $\bar{\varepsilon}_S^{pl}$ and θ_S at a constant equivalent plastic strain rate for material A, B, C and D are shown in Fig. 4.5(a) and (b), respectively.
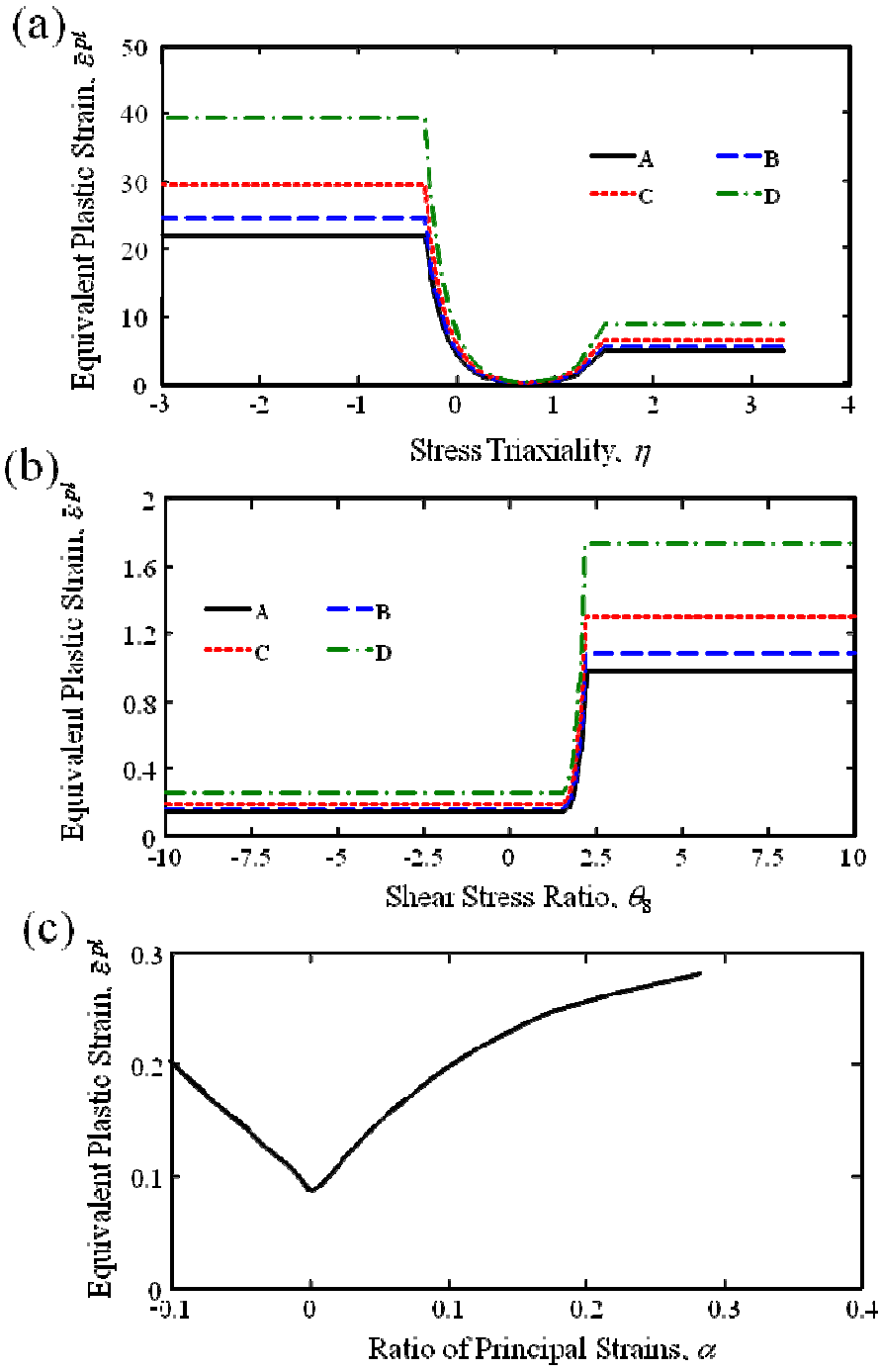
Fig. 4.5 EN AW 2024 T4 at initial state (A) and after heat treatment at 520°C (B), 540°C (C) and 560°C (D): (a) ductile criterion, (b) shear criterion, and (c) MSFLD criterion.

Meanwhile for the MSFLD a forming limit curve, the equivalent plastic strain versus ratio of principal strain rates, α, as shown in Fig. 4.5(c), was assumed. In ABAQUS, the value of α during a given time increment, from t to $t+\Delta t$ is computed using the following filtering method:

$$\alpha_{t+\Delta t} = (1 + OMEGA)\, \alpha_t + OMEGA\, \frac{\Delta\varepsilon_{minor}}{\Delta\varepsilon_{major}}, \qquad\qquad (4.2)$$

where $\Delta\varepsilon_{minor}$ and $\Delta\varepsilon_{major}$ are the principal values of the in-plane strain increment. The factor *OMEGA* used in conjunction with the MSFLD criterion was set to 0.001. The MSFLD criterion was met when the ratio of the current equivalent plastic strain to the equivalent plastic strain on the limit curve evaluated at the current values of α equal to one.

Damage evolution starts once the damage initiation has been reached. The plastic displacement-based linear damage evolution law was used for each of the damage initiation criterion. The value of the plastic displacement, at which the damage variable reaches 1, was taken as 0.1.

The contact between the rigid plate and the crash box was modeled using a node-to-surface contact pair with a friction coefficient of 0.3. Meanwhile for the contact between crash box walls during deformation, a contact inclusions algorithm with a friction coefficient of 0.15 was used. In this study, the initial imperfections or triggers were not considered, since the predetermined mode was set by the crash box strength gradient itself. The obtained deformed shapes and load-deformation curves were then evaluated to assess the effect of the stepwise strength gradient of the crash box. The comparisons between simulation results and experimental results with the similar numerical approach for homogeneous crash box had been conducted in previous studies [5, 20, 21]. Their studies show the good qualitative agreement between simulation and experimental results. Therefore, in this study, the simulation results obtained are reasonable to observe the effect of the stepwise strength gradient on the crash behavior of crash box even though the experimental works are yet to be conducted.

4.4 Results and Discussion

4.4.1 Failure Pattern of FGM Crash box

Figures 4.6(a) to (f) show the typical crash patterns of crash boxes under axial loading for sFGM1, sFGM2, FGM3, sFGM4, sHA and sHD, respectively. The FGM crash boxes experience the progressive crushing as compressive loading proceeds. Although sHA and sHD have no trigger mechanism, the crushed crash boxes (Figs. 4.6(e) and (f)) also experience the progressive crushing. The progressive crushing initiated at one end of the crash box with the exception of the sFGM4 (initiated at the middle) and failure gradually spreading along the crash box's length. The failure patterns are different depending on the material strength of crash box. For the crash box made from homogeneous material, sHA and sHD, the crushing failure pattern totally depends on the geometrical failure. On the other hand, for the crash box with stepwise strength gradient, the crushing failure pattern is also influenced on the material strength. The progressive crushing of the FGM crash box is more systematic than the homogeneous crash box. Crash deformation is initiated at a certain area where compressive strain is locally accumulated. For the FGM crash box, the deformation is started at the segments with lowest strength (segment A) as shown in Figs. 4.6(a) to (d). Then, plastic buckling arises at the above area and creates wrinkle. After the wrinkle is folded or failed, a new plastic buckling is caused at another area. The effect of the improvement of material ductility can be observed from the crushed sHA and sHD crash box (Figs. 4.6(e) and (f)). The sHD with better material ductility than sHA shows more stable collapse process. As can be observed in Fig. 4.6(f), some part of the sHA was systematically folded.

Figures 4.7(a) to (d) show the typical crash patterns of sFGM1 crash boxes under quasi-static and dynamic impact loading with initial impact velocity of 15, 30 and 45 km/h, respectively. As can be observed in these figures, the crash boxes experience almost similar crash failure pattern. For all load cases, the crushing starts at the side of impact. The first buckle can be seen at the front part of the crash box. Unlike in the case of quasi-static and dynamic loading with an initial impact velocity of 15 km/h, the wrinkles were observed along the length of the crash box at initial buckling for the crash boxes crushed with initial impact velocities of 30 and 45 km/h.
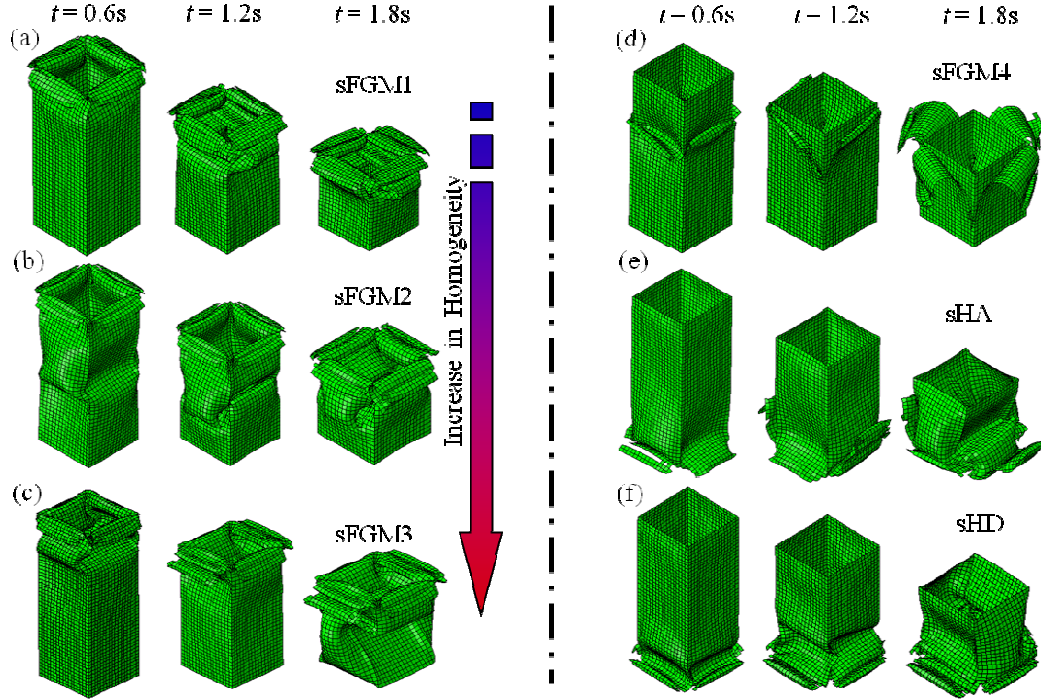
Fig. 4.6 Typical crash patterns of the crash box under axial loading: (a) sFGM1 (b) sFGM2, (c) sFGM3, (d) sFGM4, (e) sHA and (f) sHD.

The typical final shape of the crushed crash boxes under axial loading are presented in Fig. 4.8. The splaying mode was observed in all the crushed crash boxes. In sFGM1, sFGM2, sFGM3, cFGM1, pFGM1 and hFGM1, the failures were observed at the impact side. In contrast, in sFGM1R, sFGM2R and sFGM3R, the failures are caused at the opposite side. The failures are observed at both sides in sHA, sHD and sFGM4R. Different with the other crash boxes, only sFGM4 failed at the middle. A crash box with failures at the opposite side of impact is not preferable. It can be avoided by using trigger but it lowers the peak crushing load.
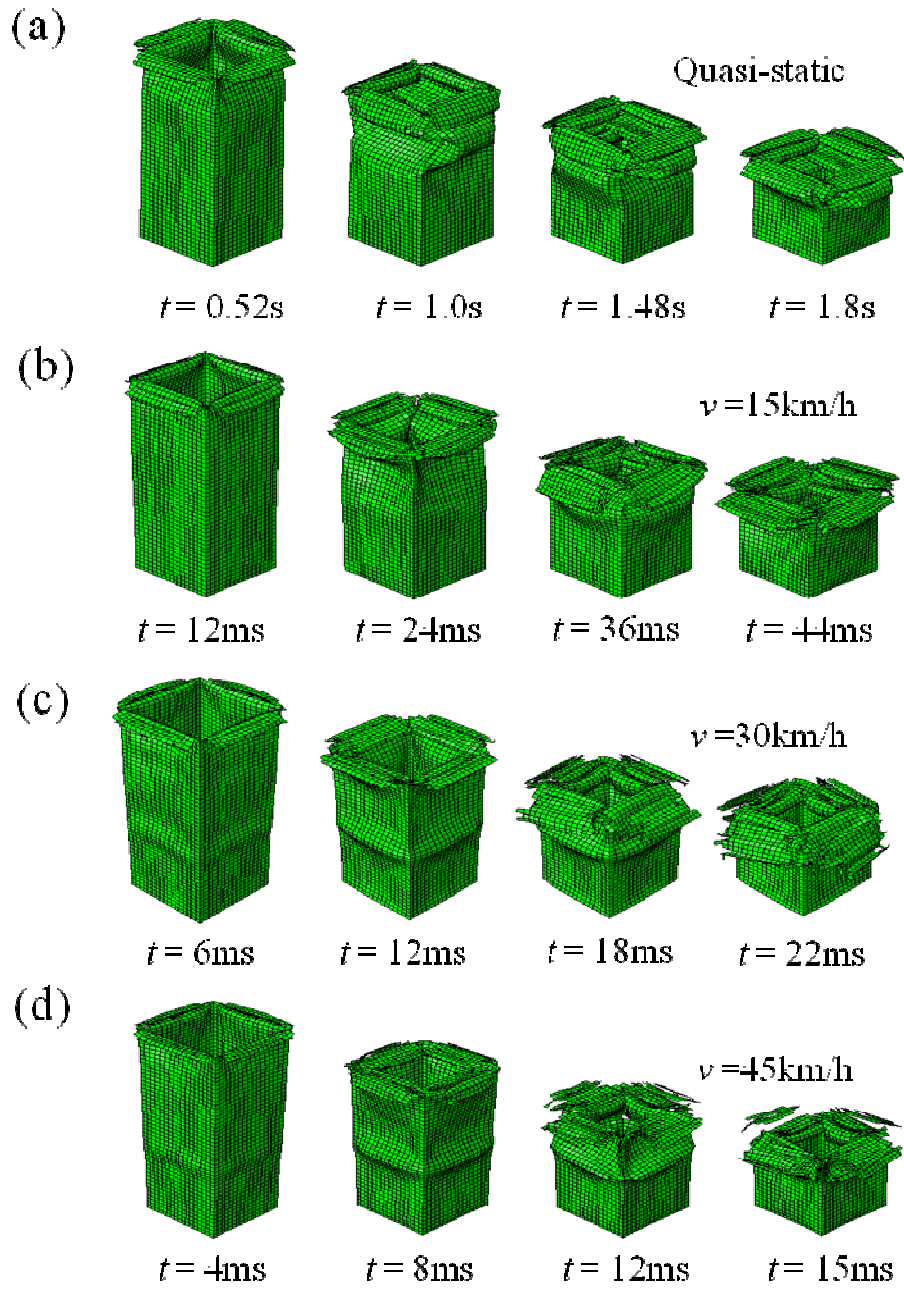
Fig. 4.7 The crash patterns of sFGM1 under different types of loading: (a) Quasi-static and (b), (c) and (d) dynamic impact loading with different initial impact velocities.
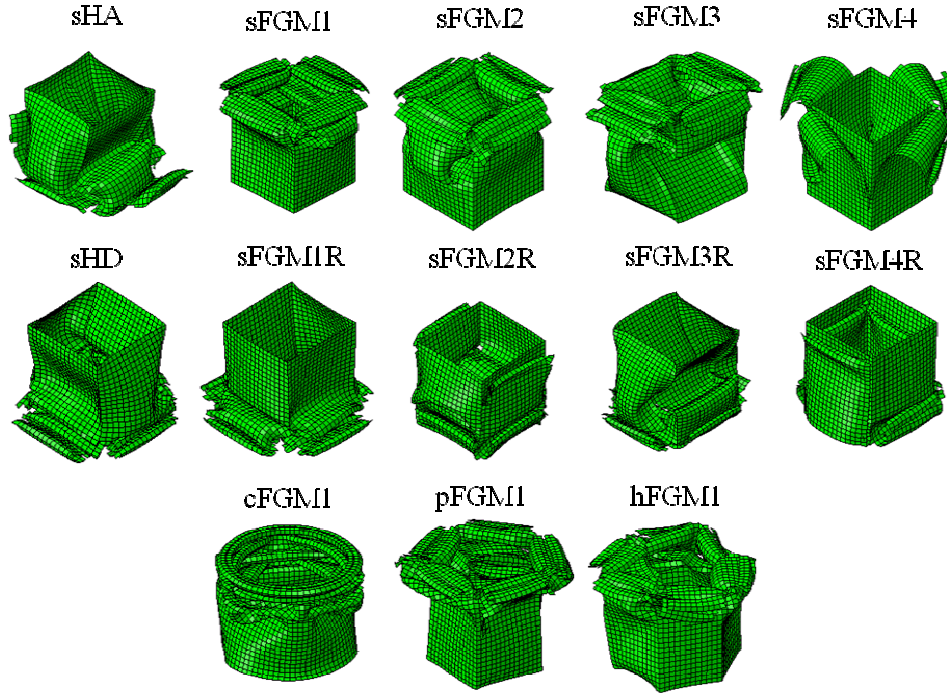
sHA   sFGM1   sFGM2   sFGM3   sFGM4

sHD   sFGM1R   sFGM2R   sFGM3R   sFGM4R

cFGM1   pFGM1   hFGM1

Fig. 4.8 The final shape of crushed crash boxes under quasi-static loading.

4.4.2 Load-Displacement Curves

Figure 4.9 shows the simulated crash load–displacement curves of the square cross-sectional shape crash boxes with different stepwise strength gradient patterns under the quasi-static loading. The load fluctuates throughout the collapse. Although the composition of materials is the same in all crash boxes, their load-displacement curve is different. As can be observed, there are almost no difference in the value of the first buckling load. According to Nakazawa et al. [8], the main points to improve the impact energy absorption are ensuring high buckling load at ridge lines, minimization of buckling cycle time and minimization of load fluctuation. From Fig. 4.9, it is seen that sFGM1 meets the requirements specified above. Compared to other crash boxes, the load fluctuation and buckling cycle time of sFGM1 is the lowest.
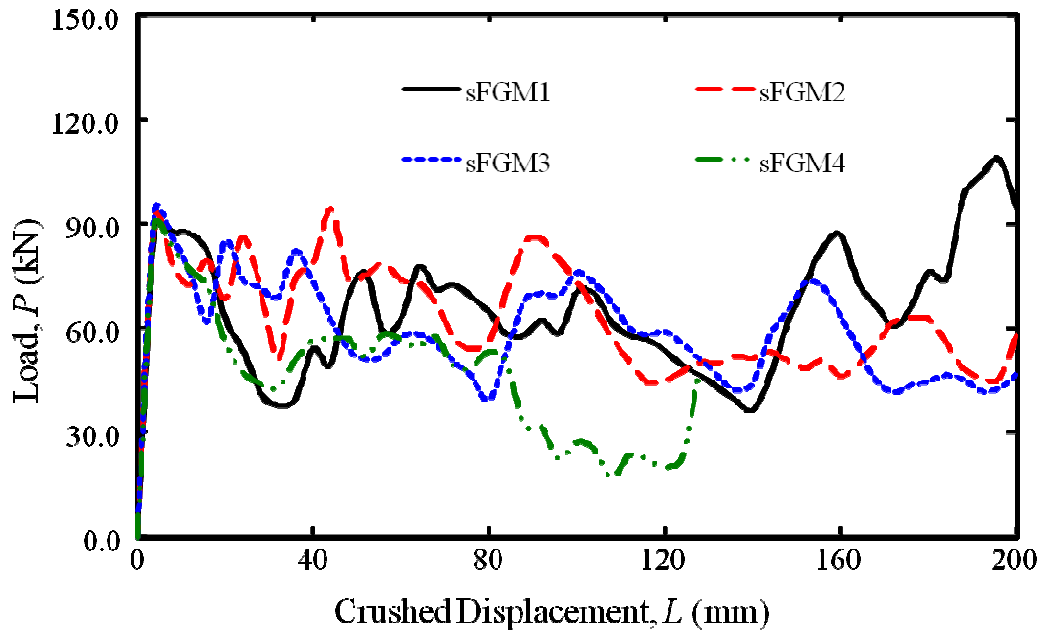
Fig. 4.9 Load-displacement curves for square cross-sectional shape of crash boxes under quasi-static loading.

In order to clarify the influences of cross-sectional shapes on the load, the analysis was carried out with various polygons, i.e., circle, square, pentagon and hexagon. Figure 4.10 shows the load-displacement curves for crash boxes made of FGM1 with different cross-section shapes under quasi-static loading. As can be observed, the crash box buckling behavior is strongly depended on the cross-sectional shape. Crash box with hexagonal cross-sectional shape attained the highest first buckling load due to the extra ridge lines than the crash box with square and pentagon cross-sectional shape. However, in terms of load fluctuation and buckling cycle, the crash box with the square cross-sectional shape shows the better minimization of load fluctuation and buckling cycle than others.
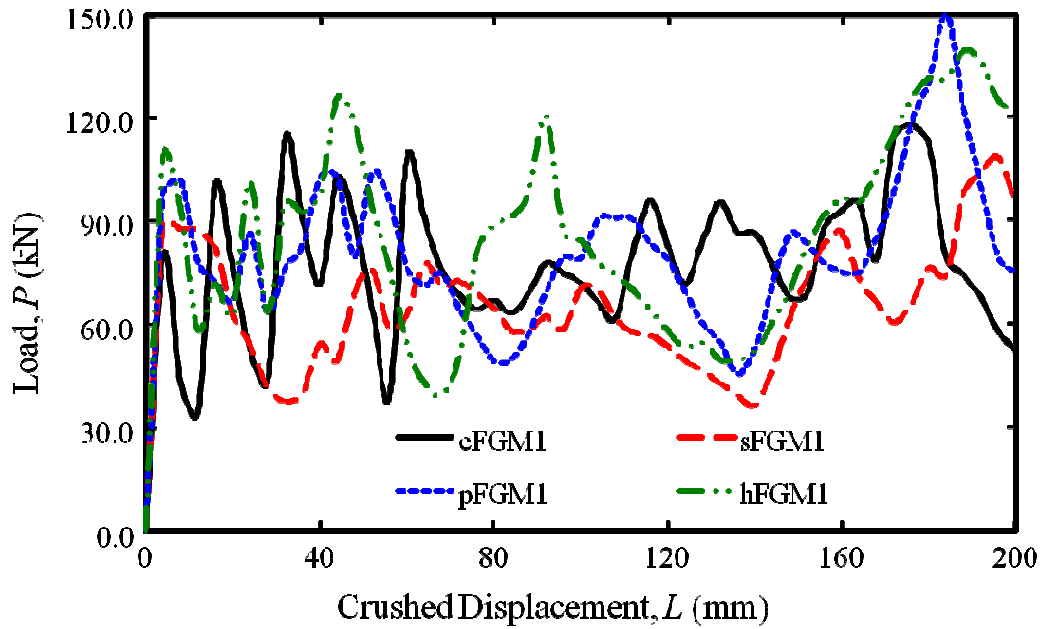
Fig. 4.10 Load-displacement curves for different cross-sectional shape i.e. circle, square, pentagon and hexagon.

Figure 4.11 shows the typical load-displacement curves for a crash box under quasi-static and dynamic impact loading with different initial impact velocities. The initial buckling load and load fluctuation increased with the impact velocity. The increasing of buckling load and load fluctuation has to be associated with inertia effects, since the material properties of aluminum alloys is assumed to be small sensitivity for the strain rates [5, 7].
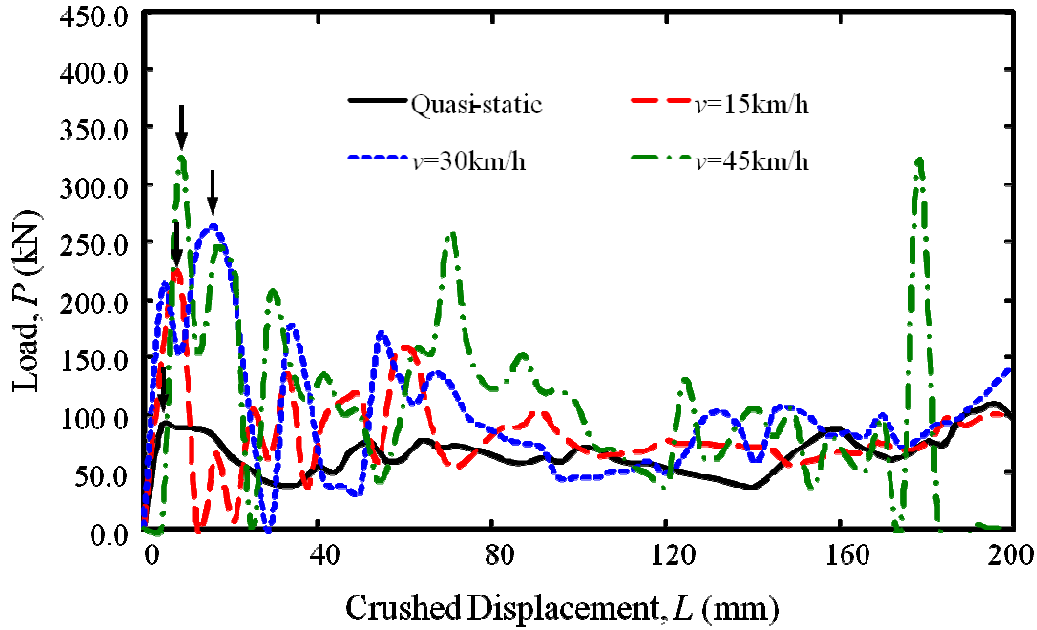
Fig. 4.11 Load-displacement curves for sFGM1 under quasi-static and dynamic loading with different initial impact velocities. Arrows indicate initial buckling loads.

4.4.3 Energy Absorption Characteristics

In order to estimate the energy absorbing capability of the designed crash box comprehensively, the specific energy absorption (SEA), crush force efficiency (CFE) and crush force coefficient of variance (CV) were calculated. The SEA is defined as the amount of energy absorbed per unit mass crushed material [3]:

$$\text{SEA} = \frac{P_{mean}L}{\rho A h} \qquad (4.3)$$

where P_{mean}, ρ, A, L and h are mean crush load, density, cross-sectional area, crushed length and initial length of a crash box, respectively. The CFE is ratio between the mean crush load, P_{mean} and the maximum load, P_{max}, which is useful to measure the performance of a crash box. The CV is the ratio between the standard deviation of the crush load, P_{stdev} and the mean crush load, P_{mean}. A low CV means the minimum load fluctuation. These parameters were investigated from the load-displacement curves of the crash boxes and plotted in Figs. 4.12 to 4.15 for quasi-static and dynamic loading

58

with different initial impact velocity, respectively. Generally, a good crash box is the crash box with the highest SEA and CFE and the lowest CV value. However, from the parameters calculated, it is found that the highest SEA, the highest CFE and the lowest CV are belonging to different crash box.

Considering the preferable square cross-sectional shape crash boxes, sFGM2 records the highest SEA and CFE and the lowest CV value under quasi-static loading. The preferable crash boxes (sFGM1, sFGM2, sFGM3 and sFGM4) are determined by the crash pattern discussed in previous section. In case of the dynamic loading, the SEA of sFGM2 shows the highest value at different initial impact velocity. However, in terms of CFE, sFGM3 shows the best force efficiency under impact loading with $v = 15$ km/h and $v = 45$ km/h. In terms of load fluctuation, sFGM3 records the lowest load fluctuation at high initial impact velocity and sFGM1 records the lowest load fluctuation at low initial impact velocity.

The effect of cross-sectional shape on the crashworthiness also can be clearly observed from the parameters calculated in Figs. 4.12 to 4.15. The crash box with hexagon cross-sectional shape (hFGM1) has the highest SEA in all cases except in case of the dynamic loading with the initial impact velocity of 30 km/h. It is reasonable since the hexagon cross-sectional shape has the highest number of ridge lines. In terms of CFE, the circle shape has the highest CFE in case of quasi-static and dynamic impact loading with $v = 45$ km/h and the pentagon shape has the highest CFE under dynamic impact loading with $v = 15$ km/h and $v = 30$ km/h. Conversely, in terms of CV, the square shape has the lowest CV in case of quasi-static and dynamic impact loading with $v = 15$ km/h.
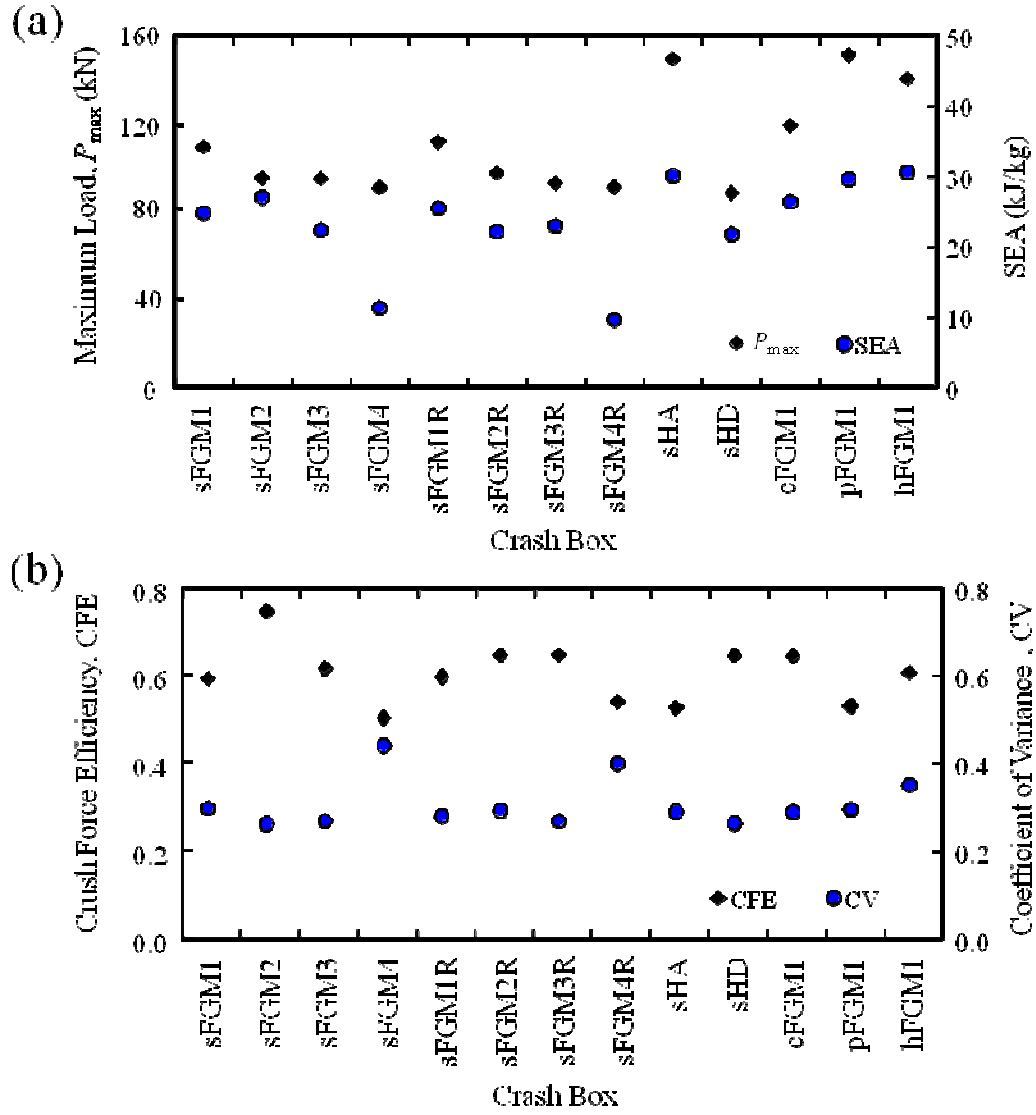
Fig. 4.12 Energy absorption characteristics of crash boxes under quasi-static loading: (a) P_{max} and SEA, and (b) CFE and CV.
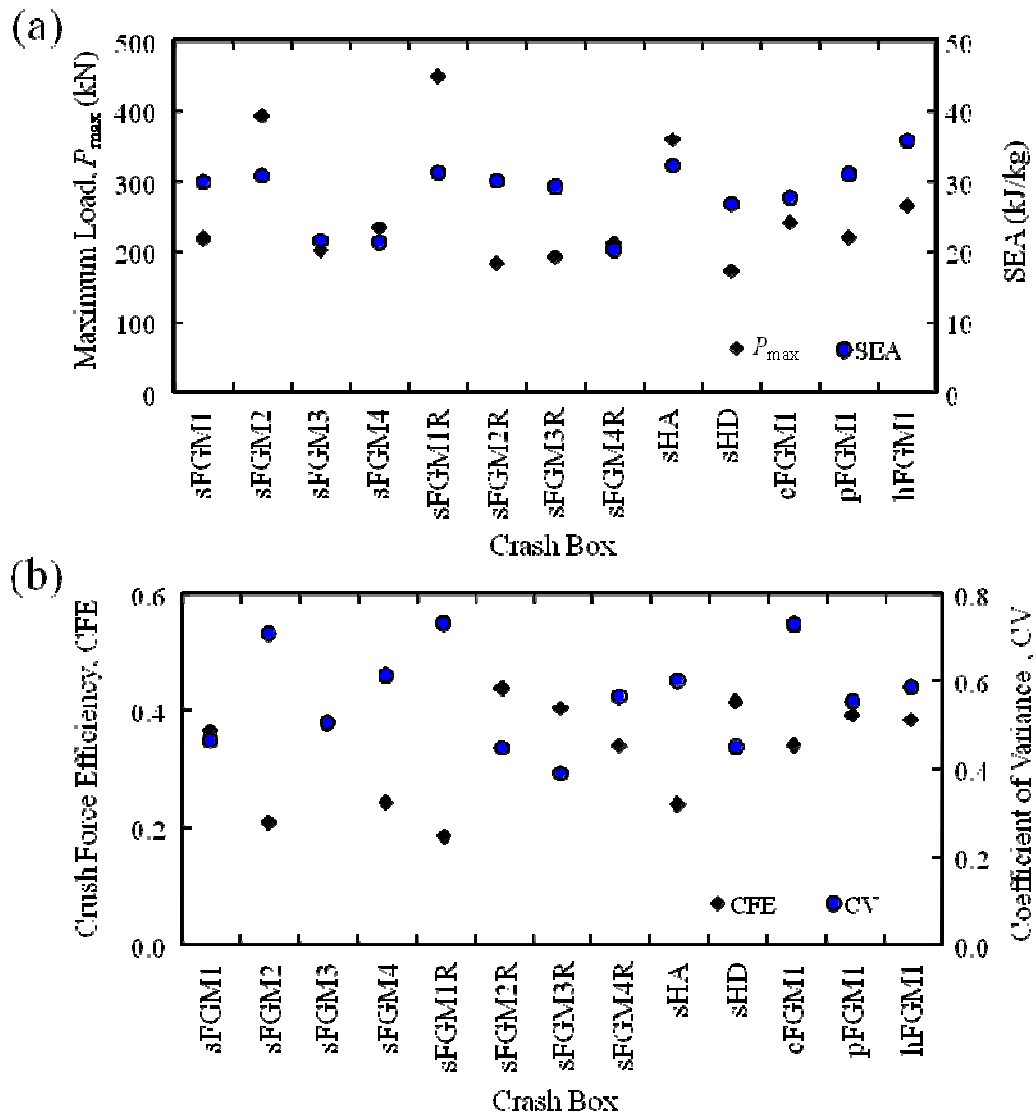
Fig. 4.13 Energy absorption characteristics of the crash boxes under dynamic impact loading (v = 15km/h): (a) P_{max} and SEA, and (b) CFE and CV.
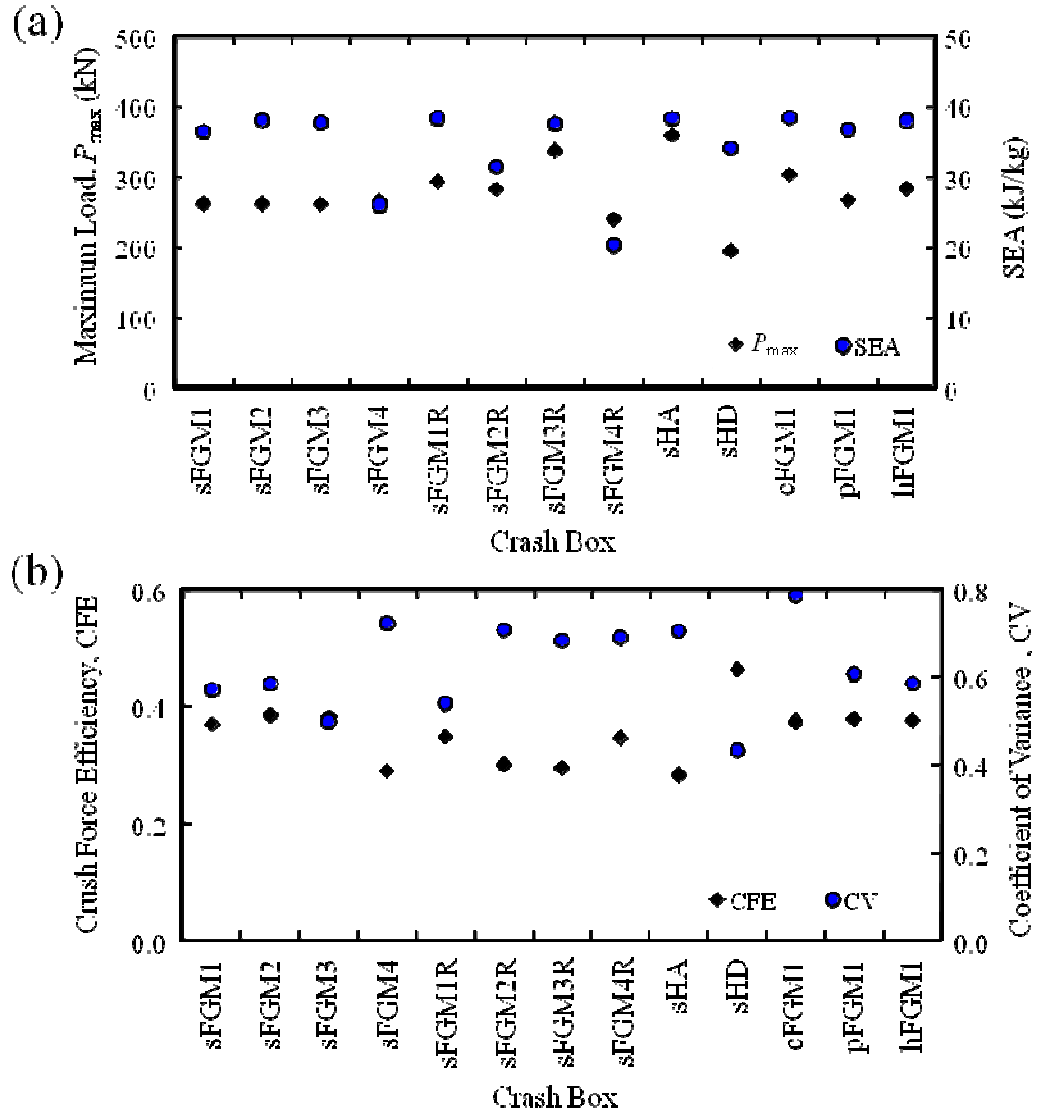
Fig. 4.14 Energy absorption characteristics of the crash boxes under dynamic impact loading (v = 30km/h): (a) P_{max} and SEA, and (b) CFE and CV.
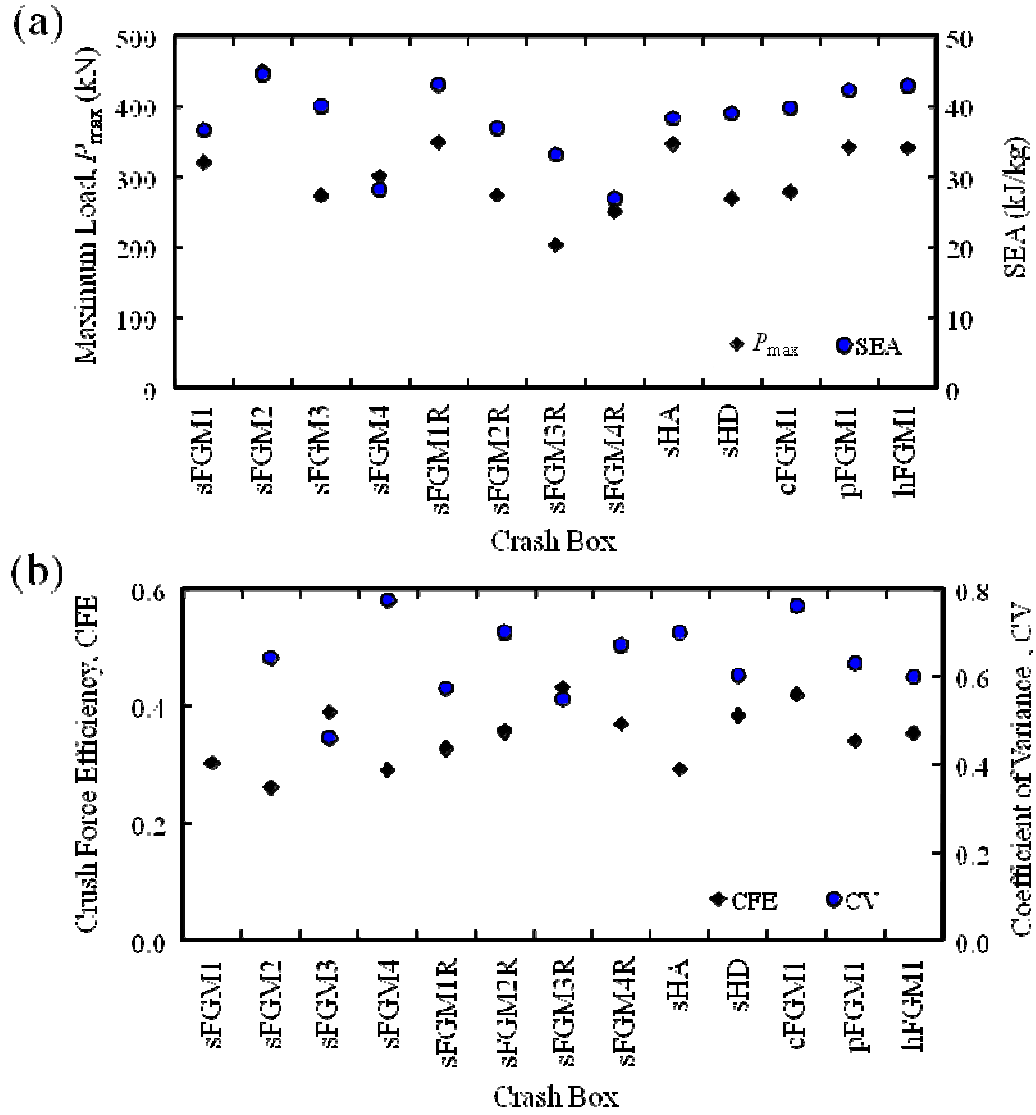
Fig. 4.15 Energy absorption characteristics of the crash boxes under dynamic impact loading ($v = 45$km/h): (a) P_{max} and SEA, and (b) CFE and CV.

4.5 Conclusions

A new design of crash box with stepwise strength gradient in longitudinal directions has been successfully proposed. The crash behavior of FGM crash boxes with different stepwise strength gradients were investigated using FEM. The results of numerical simulations showed that the crash or folding patterns can be pre-determined by using FGMs. High crash energy absorption can be achieved by the proposed FGM crash box. Moreover, it is shown that the energy absorption characteristics of crash box are changed with different stepwise strength gradient in FGMs and the cross-sectional shape of the crash box. In designing an FGM crash box for certain purpose, the stepwise strength gradient in FGMs and/or the cross-sectional shape of the crash box can be changed depends on the type of loading. For an example, the stepwise strength gradient FGM2, which gives high crash force efficiency and low load fluctuation, is recommended for the crash box under the quasi-static load. In contrast, for the cross-sectional shape of the crash box under the same loading condition, hexagonal is recommended.

References

1) K.S. Bae: Front structure for car body. United States Patent (2009) US007533913 **B2**.

2) H. R. Zarei, M. Kroger, and H. Albertsen: Compos. Struct. **85** (2008) 245.

3) J. S. Kim, H.J. Yoon, and K.B. Shin: Adv. Compos. Mater. **20** (2011) 385.

4) H. S. Kim: Thin-Walled Struct. **40** (2002) 311.

5) J.S. Qiao, J.H. Chen, and H.Y. Che: Thin-Walled Struct. **44** (2006) 692.

6) A. Rusinek,R. Zaera, P. Forquin, and J.R. Klepaczko: Thin-Walled Struct. **46** (2008) 1143.

7) M. Langseth,O.S. Hopperstad, and T. Berstad: Int. J. Impact Eng. **22** (1999) 829.

8) Y. Nakazawa, K. Tamura, M. Yoshida, K. Takagi, and M. Kano: in Onate, E.,Owen and D.R.J. (Eds.): Proceedings of the VIII International Conference on Computational Plasticity (COMPLAS VIII), Barcelona (2005) p. 167.

9) K. Tamura, Y. Nakazawa, M. Yoshida, K. Takagi, and M. Kano: Bull. Iron Steel Inst. Japan **16** (2011) 369. (*in Japanese*).

10) A.G. Mamalis, D.E. Manolakos, M.B. Ioannidis, D.G. Chronopoulos, and P.K. Kostazos: Comp. Struct. **89** (2009) 416.

11) J. Bi, H. Fang,Q. Wang, and X. Ren: Finite Elements in Analysis and Design **46** (2010) 698.

12) S. Santosa and T. Wierzbicki: Comput. Struct. **68** (1998) 343.

13) H.W. Song, Z.J. Fan, G. Yu, Q.C. Wang, and A. Tobota: Int. J. Solid Struct. **42** (2005) 2575.

14) G. Sun, G. Li, S. Hou, S. Zhou, W. Li, and Q. Li: Mater. Sci. Eng. A **527** (2010) 1911.

15) L. Peroni, M. Avalle, and G. Belingardi: Int. J. Impact Eng. **36** (2009) 498.

16) N. Gupta and W. Ricci: Mater. Sci. Eng. A **427** (2006) 331.

17) S. Kiernan, L. Cui, and M.D. Gilchrist: Int. J. Non-Linears Mech. **44** (2009) 456.

18) A.H. Brothers and D.C. Dunand: Mater. Sci. Eng. A **489** (2008) 439.

19) M. Fujda, R. Mišičko, L. Rusňáková, and M. Sojko: J. Metal. Mater. Miner. **17** (2007) 35.

20) H. Hooputra, H. Gese, H. Dell, and H. Werner: Int. J. Crash **9** (2004) 449.

21) ABAQUS analysis user manual. Version 6.8. Dassault Systemes 2008.

Chapter 5

Thermo-Visco-Plasticity and Creep Analysis of Thick-Walled Pressure Vessels made of Functionally Graded Materials

5.1 Introduction

The pressure vessels commonly used in industry is a thick-walled cylinder. From the strength analysis, if the homogeneous materials are used, the most dangerous point is located at the inner portion of the cylinder. However, if the functionally graded materials (FGMs) are used for the pressure vessels, this situation can be changed [1]. The composition and the morphology of FGMs gradually change over the volume; consequently, the material properties of the material change with position. Thus, the stress and strain distributions along the radius direction in a thick-walled cylinder can be changed by varying the material composition.

The elastic analysis for a cylinder made of FGMs has been investigated by numerous researchers [1−6]. However, the pressure vessels are expected to expose to high temperature and pressure for long time. Therefore, the creep behavior and plastic deformation should be considered. Creep damage for most materials becomes significant at a temperature above $0.4T_M$, where T_M is melting temperature.

In this paper, the finite element method (FEM) is used to obtain the thermo-visco-plasticity and creep behavior of FGM asymmetrical structure under thermal and mechanical loading. The structure is approximated by a set of finite elements. The element used to represent the structure is a four-node rectangular element. The FGM is characterized by continuously changing properties due to a continuous change in composition. The material properties in function of volume fraction of material composition are calculated at every integration points. The combination of two different materials is considered for an FGM. An incremental approach is used to handle the inclusion of creep behavior in finite element model. The creep strains are treated as

66

initial strains. The creep strains for a small time interval, Δt at time $t + \Delta t$ are computed based on the stresses obtained from the previous time, t. The validity of the finite element model is verified for a homogeneous thick-walled pressure vessel. After that the model is demonstrated for FGM thick-walled pressure vessels. The numerical results of thermo-visco-plasticity with creep are presented to examine the effects of graded components on the stress distributions.

5.2 Finite Element Formulation of Thermo-Visco-Plasticity and Creep Analysis

This section presents the basic incremental equations for thermo-visco-plasticity and creep. The thick-walled cylinder is a geometric symmetry about a reference axis and can be solved using two-dimensional elements for an example 4-node rectangular element shown in Fig. 5.1. Therefore, the structure can then be represented by axisymmetric ring elements and analyzed in a similar fashion to that of a two-dimensional problem ($r - z$ plane) using polar coordinates, (r, θ, z).
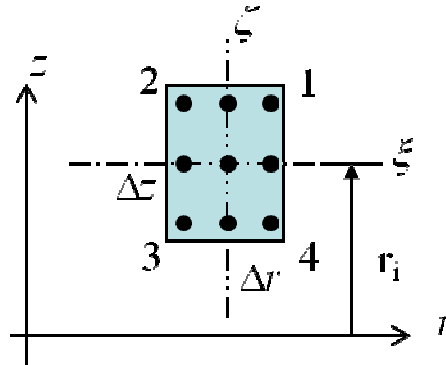

Fig. 5.1 A rectangular element with nine integration points in *r-z* plane.

The thermo-visco-plasticity was introduced by Zienkiewics and Cormeau [7]. The total change in strain during time interval is the sum of the changes in elastic, visco-plastic, creep and thermal strain, i.e

$$\Delta \boldsymbol{\varepsilon}^{\mathrm{T}} = \Delta \boldsymbol{\varepsilon}^{\mathrm{e}} + \Delta \boldsymbol{\varepsilon}^{\mathrm{vp}} + \Delta \boldsymbol{\varepsilon}^{\mathrm{C}} + \Delta \boldsymbol{\varepsilon}^{\mathrm{th}} \tag{5.1}$$

where

$\Delta \boldsymbol{\varepsilon}^{\mathrm{T}}$ stands for total change in strain,

$\Delta \boldsymbol{\varepsilon}^{\mathrm{e}}$ stands for incremental elastic strain,

67

$\Delta\boldsymbol{\varepsilon}^{vp}$ stands for incremental visco-plastic strain,

$\Delta\boldsymbol{\varepsilon}^{C}$ stands for incremental creep strain,

and

$\Delta\boldsymbol{\varepsilon}^{th}$ stands for incremental thermal strain.

The incremental stress $\Delta\boldsymbol{\sigma}$ are then related to the elastic strains given by

$$\Delta\boldsymbol{\sigma} = \mathbf{D}(\Delta\boldsymbol{\varepsilon}^{T} - \Delta\boldsymbol{\varepsilon}^{vp} - \Delta\boldsymbol{\varepsilon}^{C} - \Delta\boldsymbol{\varepsilon}^{th}) \tag{5.2}.$$

Here, $\mathbf{D}$ is a symmetric elasticity matrix(compliance matrix). The thermal strain is calculated from

$$\Delta\boldsymbol{\varepsilon}^{th} = \alpha\Delta\mathbf{T} \tag{5.3}$$

where α and $\Delta\mathbf{T}$ are the coefficient of thermal expansion and the incremental temperature, respectively. The visco-plastic strains are generated at a rate that is related to the amount by which yield has been violated through the expression

$$\dot{\boldsymbol{\varepsilon}}^{vp} = F\frac{\partial\mathbf{Q}}{\partial\boldsymbol{\sigma}} \tag{5.4}.$$

Here, F and $\mathbf{Q}$ are the yield condition and plasticity potential, respectively. The yield condition is given as

$$F = \sigma_{eff} - \sqrt{3}\,\mu_S \tag{5.5}$$

where σ_{eff} and μ_S are effective stress and shear modulus, respectively. Shear modulus is given in function of temperature as follow

$$\mu_S = \mu_0\left(1 + \frac{T - T_0}{T_M}\right)\left(\frac{T_M}{\mu_0}\frac{d\mu}{dT}\right) \tag{5.6}$$

where μ_0, T, T_0, T_M, and $\left(\dfrac{T_M}{\mu_0}\dfrac{d\mu}{dT}\right)$ are shear modulus at room temperature, instant temperature, room temperature, melting temperature and temperature dependence of modulus, respectively. $F < 0$ denoting the purely elastic region and $F \geq 0$ denoting visco-plasticity region. When the visco-plasticity is invoked, the visco-plastic strain rate is calculated by Eq. (5.4). Then the increment of visco-plastic strain is determined by multiplication of the visco-plastic strain rate, $\dot{\boldsymbol{\varepsilon}}^{vp}$ by a time step Δt; thus

$$\Delta \boldsymbol{\varepsilon}^{vp} = \Delta t \left(\dot{\boldsymbol{\varepsilon}}^{vp} \right) \qquad (5.7).$$

The derivatives of the plastic potential function with respect to stresses are complex. However it can be evaluated numerically. The appropriate step to determine it can be found in Zienkiewics and Cormeau [7].

The increment of creep strain is determined by

$$\Delta \boldsymbol{\varepsilon}^{c} = \frac{\dot{\varepsilon}^{C}}{2\sigma_{eff}} \Delta t \begin{bmatrix} 2\sigma_r - \sigma_z - \sigma_\theta \\ 2\sigma_z - \sigma_r - \sigma_\theta \\ 2\sigma_\theta - \sigma_r - \sigma_z \\ 3\sigma_{rz} \end{bmatrix} \qquad (5.8)$$

where $\dot{\varepsilon}^{C}$ is creep strain rate, and σ_r, σ_z, σ_θ and σ_{rz} are the radial, z-axis, circumferential and shear stress components, respectively. The creep strain rate is determined by the Coble creep equation. The Coble creep equation, which is applicable to fine-grain polycystalline materials [8, 9], is assumed

$$\dot{\varepsilon}^{C} = \frac{40\pi D_w \Omega}{d^3} \sigma_{eff} \exp\left(-\frac{Q}{RT} \right) \qquad (5.9).$$

Here, d, D_w, Q, Ω and R are grain size, boundary diffusion pre-exponential constant, boundary diffusion activation energy, atomic volume and gas constant coefficient, respectively. The increment of creep strain at any integration point is calculated when the temperature at the corresponding point above $0.4T_M$. The increment of total strain are obtained from the relationship between strain and displacement, where the incremental displacement can be calculated by a general equation in FEM,

$$\Delta \mathbf{u} = \mathbf{K}^{-1} [\Delta \mathbf{R}] \qquad (5.10)$$

where

$\mathbf{K}$ is stiffness matrix

and

$\Delta \mathbf{R}$ is incremental load matrix consisting of external load and body-loads vector caused by inelastic strain.

The analysis is conducted by solving the heat conduction equation, stress equilibrium equation with visco-plastic constitutive equation and creep equation simultaneously. In

order to determine the temperature distribution at time *t*, a heat conduction equation of the following form is analyzed

$$\rho c_p \frac{dT}{dt} = \frac{d}{dr} k_r \frac{dT}{dr} + \frac{k_r}{r} \frac{dT}{dr} + \frac{d}{dz} k_z \frac{dT}{dz} + HG \qquad (5.11).$$

Here, ρ, c_p, k and HG are the mass density, specific heat, heat conductivity and heat generated, respectively.

The FGM considered is made of two material components. The FGM thick-walled cylinder is assumed to be a kind of single solid phase where the material composition changes toward the radial direction. The compositional gradation in FGM is defined by the volume fraction given as follows

$$f_A(\xi, \eta) = 1 - f_B(\xi, \eta) = \frac{r(\xi, \eta) - r_{inner}}{r_{outer} - r_{inner}} \qquad (5.12).$$

where f_A and f_B are the volume fraction of material components A and B, respectively. Therefore, the thermal expansion coefficient, α, the Young's modulus, E, and the thermal conductivity, k in a two-component system at integration point,(η, ξ), as related to the composition, are expressed as follows [10]:

$$\alpha(\eta, \xi) = f_A \alpha_A + f_B \alpha_B + f_A f_B \frac{(\alpha_A - \alpha_B)(E_A - E_B)}{f_A E_A + f_B E_B} \qquad (5.13)$$

$$E(\eta, \xi) = f_A E_A + f_B E_B + f_A f_B \frac{(E_A - E_B)(1/E_A - 1/E_B)}{f_A/E_A + f_B/E_B} \qquad (5.14)$$

$$k(\eta, \xi) = f_A k_A + f_B k_B + f_A f_B \frac{k_A - k_B}{f_A + 3k_A/k_B} \qquad (5.15).$$

The rest material properties are treated similar to the rule of mixtures approach. For an example, the density at integration point is given by:

$$\rho(\eta, \xi) = f_A \rho_A + f_B \rho_B \qquad (5.16).$$

In this study, the incremental deformation theory or known as the initial strain approach is applied. The advantage of this approach is that no iterative procedure is necessary as in the case of the initial stress approach [11]. A disadvantage of the incremental approach is the necessity of using very small load increments. Therefore in

70

this study the selection of time steps is very important. The time steps is set to be smaller than

$$\Delta t = \frac{4(1+v)\sigma_{eff}}{3E\dot{\varepsilon}^C}$$ (5.17)

The solution technique is then as follows:

  a) Initialize strain for all element in model.

  b) Compute temperature, displacement, strain and stress due to initial loads

  c) Set the time increment by Eq.(5.17).

  d) Determine the incremental thermal strain, the incremental visco-plasticity strain (if exceed the yield condition) and the incremental creep strain.

  e) Compute the incremental deformation by Eq. (5.10).

  f) Compute the incremental stress by Eq. (5.2).

  g) Update the stress, strain and deformation

$$\boldsymbol{\sigma}^{t+\Delta t} = \boldsymbol{\sigma}^t + \Delta\boldsymbol{\sigma}$$

$$\boldsymbol{\varepsilon}^{t+\Delta t} = \boldsymbol{\varepsilon}^t + \Delta\boldsymbol{\varepsilon}$$

$$\mathbf{u}^{t+\Delta t} = \mathbf{u}^t + \Delta\mathbf{u}$$

  h) Repeat step c) to g) for the next time step.

5.3 Results and Discussion

5.3.1 Verification of Finite Element Model

To verify the validity of the present finite element model, it is applied to the case of a homogeneous isotropic thick-walled pressure vessel. For this purpose, a problem solved by Greenbaum and Rubinstein [12] is considered. The creep behavior of thick-walled pressure vessels with spherical-end closure as shown in Fig. 5.2 is recomputed. The obtained results are shown in Figs. 5.3 and 5.4. Excellent comparison between the two results is shown. The small difference between these two results may come from the different element type and mesh used. In the present study, the pressure vessel is modeled by 200 rectangular elements and 231 nodes. Meanwhile, in the previous study 520 triangular elements and 301 nodes are used.

$r_{inner} = 4.04$ mm , $r_{outer} = 6.25$ mm, $L = 8.23$ mm

$P = 3.07$MPa,

E=137.9GPa, v=0.3

$\dot{\varepsilon}_c = 21.146 \times 10^{-16} (\sigma_{eff.})^{4.4}$ hr^{-1}
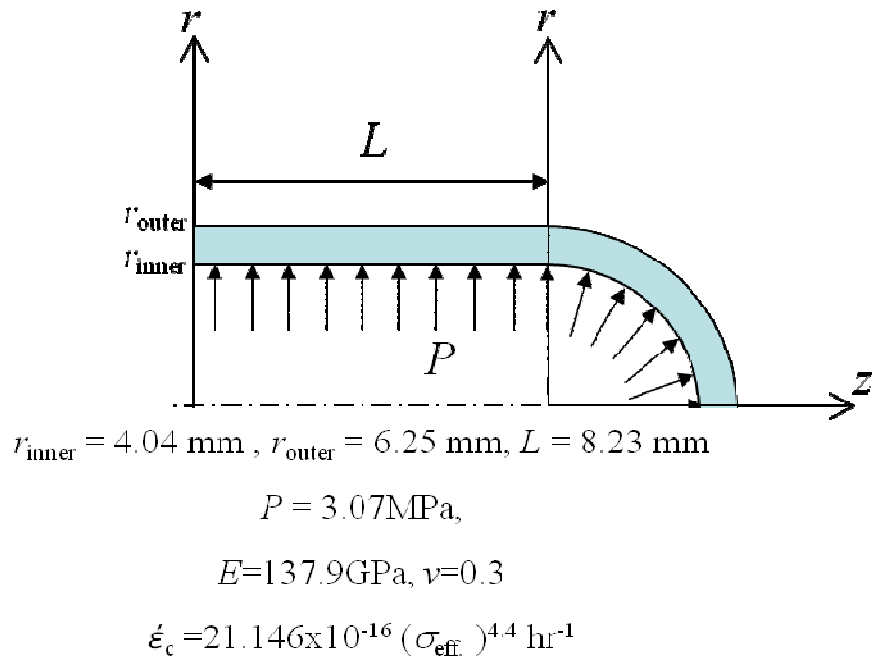
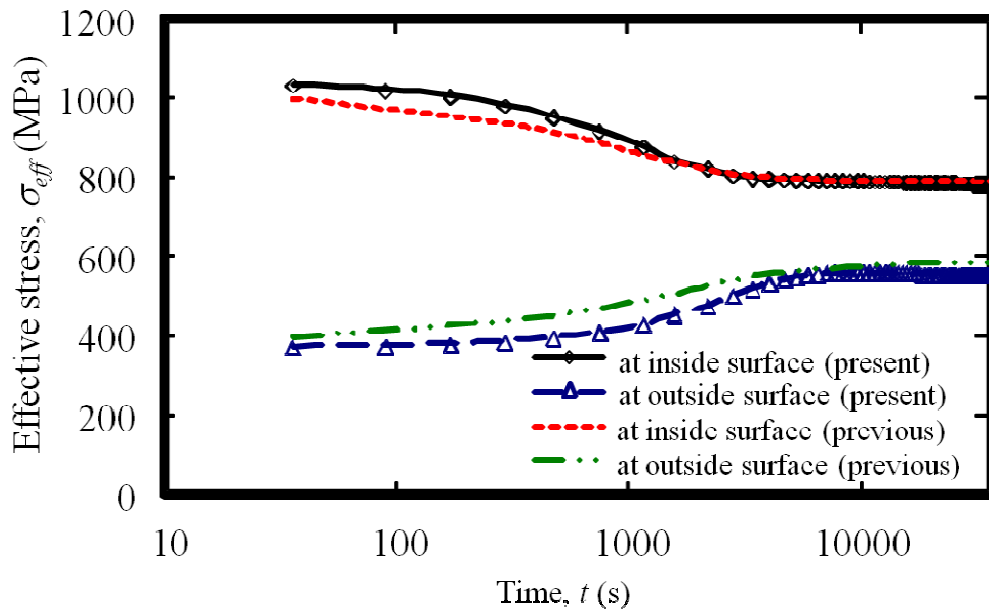Fig. 5.2 Thick-walled pressure vessels with spherical end closure.

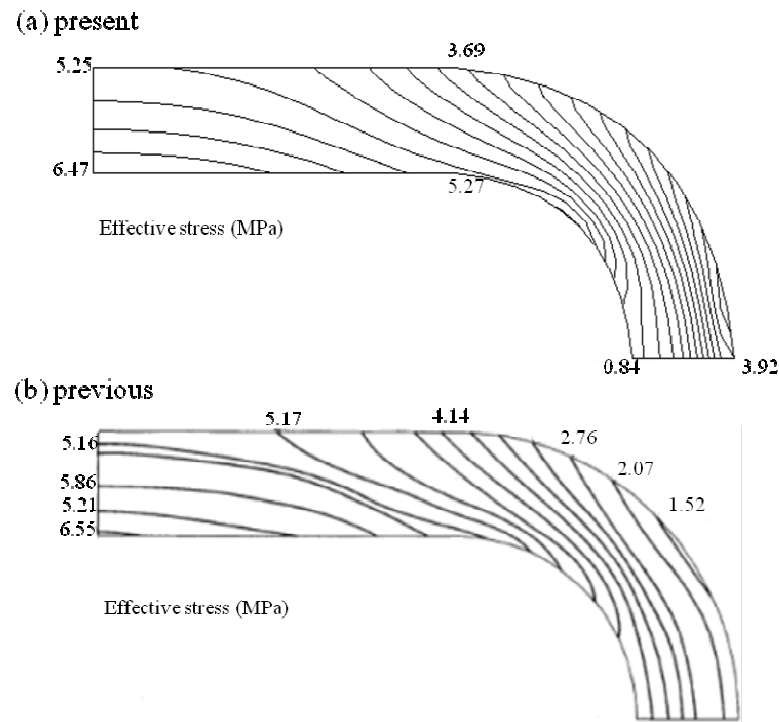Fig. 5.3 Stress relaxation at the junction of the cylinder closure.

Fig. 5.4 Effective stress contour line at time t=3 hours for the pressure vessel with a spherical end closure: (a) present study and (b) previous work [12].

5.3.2 FGM Thick-walled Pressure Vessels

Figure 5.5 illustrates the model of one quarter of thick-walled pressure vessel with spherical end closure under mechanical and thermal loadings. Plane stress conditions are assumed. The structure is modeled by a total 200 rectangular elements and 231 nodes. As subject of study, Cu-Ni system is considered for the material of thick-walled pressure vessels. Three thick-walled pressure vessels with different material compositions are analyzed. The three thick-walled pressure vessels are homogeneous Cu-50%Ni alloy (H1), Cu-Ni FGM (Cu-rich at the outer surface, FGM1) and Ni-Cu FGM (Ni-rich at the outer surface, FGM2). The material properties of Cu and Ni are listed in Table 5.1. The thick-walled pressure vessels are loaded with pressure of 2 MPa at the inner surface and thermal loading as shown in Fig. 5.5. The initial temperature is held at 300 K over the entire thick-walled pressure vessels.
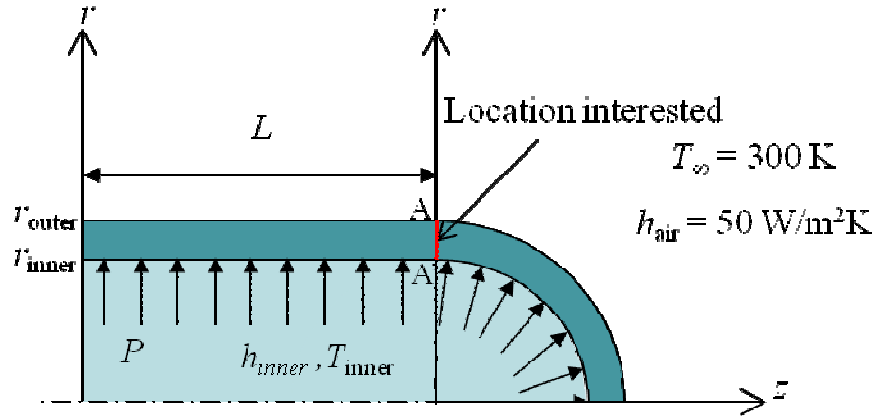
$$r_{inner} = 7 \text{ mm}, r_{outer} = 10 \text{ mm}, L = 12 \text{mm}$$

$$P = 2 \text{ MPa}, h_{inner} = 500 \text{ W/m}^2\text{K}, T_{inner} = 773 \text{ K}$$

Fig. 5.5 Thick walled pressure vessels with spherical end closure under mechanical and thermal loading.

Figures 5.6(a) to (d) show the temperature distributions along line A-A' at the cylinder-end closure as a function of the normalized radius after 0.01, 0.5, 50 and 600 s, respectively. The abscissa represents the position of normalized thickness of the cylinder, i.e., 0.0 is the inner surface and 1.0 is the outer surface. Initially, the temperature difference between the inner surface and outer surface is large. However, this difference narrowed with increasing time. The increase in temperature of FGM1 is faster than the increase in temperature of FGM2 and H1. It is reasonable since in FGM1 content rich Cu than that in H1 and FGM2. Cu is well known as good thermal conductivity material. Figures 6.7(a), (b) and (c) indicate the radial stress, circumferential stress and z-axis stress contours at $t = 10810$ s, respectively. At this time the stresses have almost reached a steady-state condition. All the stresses are tensile at the entire thick-walled pressure vessels. These figures show a remarkable dependence on the gradation of components. For H1, almost no different in all stress components is observed. On the other hand, there are big different in all stress components of FGM1 and FGM2. It is noted that, the

74

high stress concentration area in FGM1 is close to the inner surface. Unlike FGM1, the high stress concentration area in FGM2 is close to the outer surface.

Table 5.1 The material properties of Cu and Ni

| Parameter	Unit	Cu	Ni
Young's modulus, E	GPa	110	207
Poisson's ratio, v		0.35	0.31
Density, ρ	kg/m^3	7940	8880
CTE, α	1/K	1.85×10^{-5}	1.31×10^{-5}
Thermal conductivity, K	W/m-K	385	60.7
Specific heat, Cp	J/kg-K	385	406
Shear modulus at room temperature, μ_0	GPa	42.1	78.9
Melting temperature, T_M	K	1356	1726
Temperature dependence of modulus, $\left(\dfrac{T_M}{\mu_0}\dfrac{d\mu}{dT}\right)$		-0.54	-0.64
Boundary diffusion pre-exponential, D_w	m^3/s	5×10^{-15}	3.5×10^{-15}
Boundary diffusion activation energy, Q	kJ/mol	104	115
Atomic volume, Ω	m^3	1.18×10^{-29}	1.09×10^{-29}
Grain size, d	m	1×10^{-4}	1×10^{-5}

Fig. 5.6 (cont.)

76

(d)
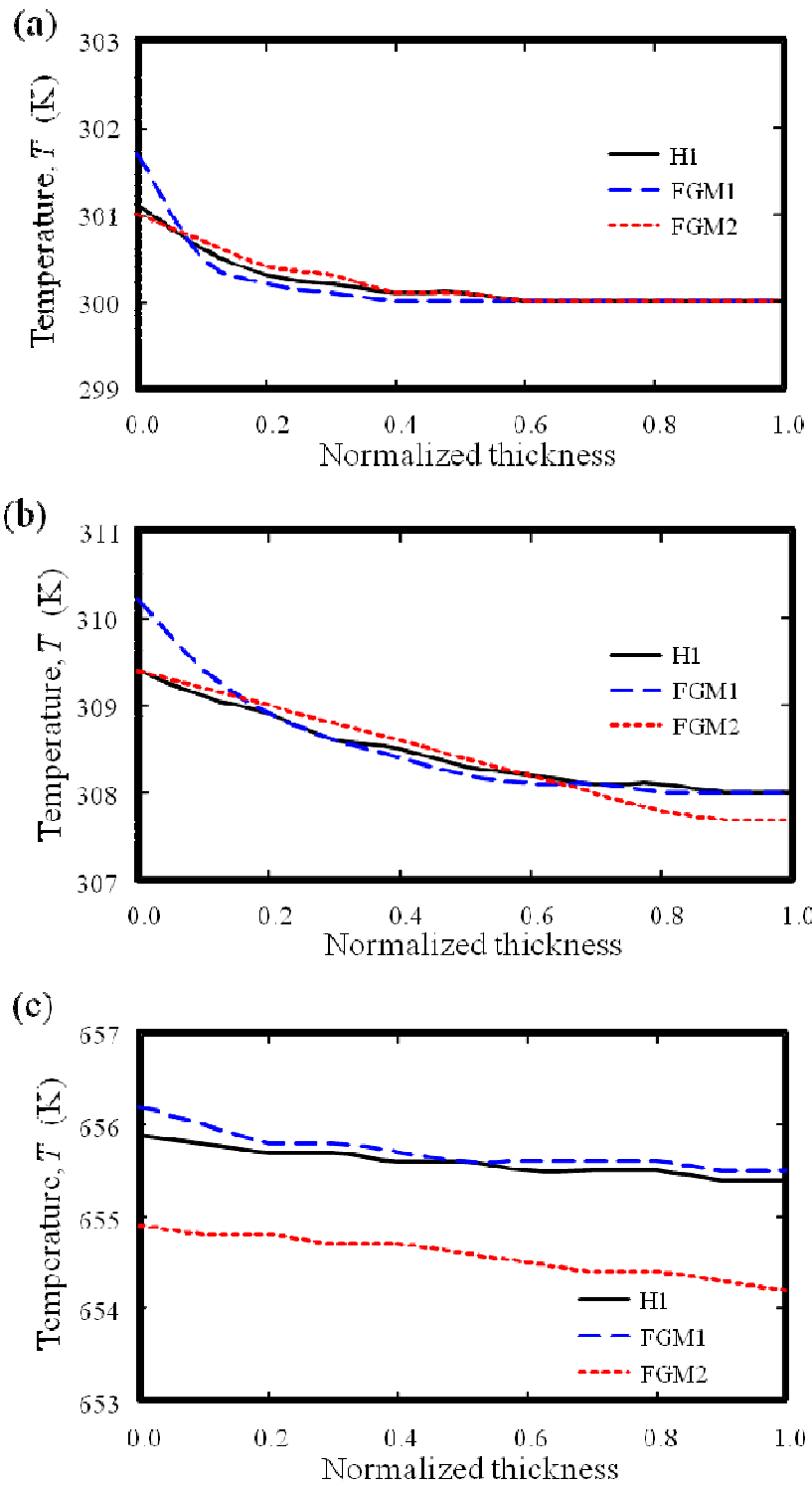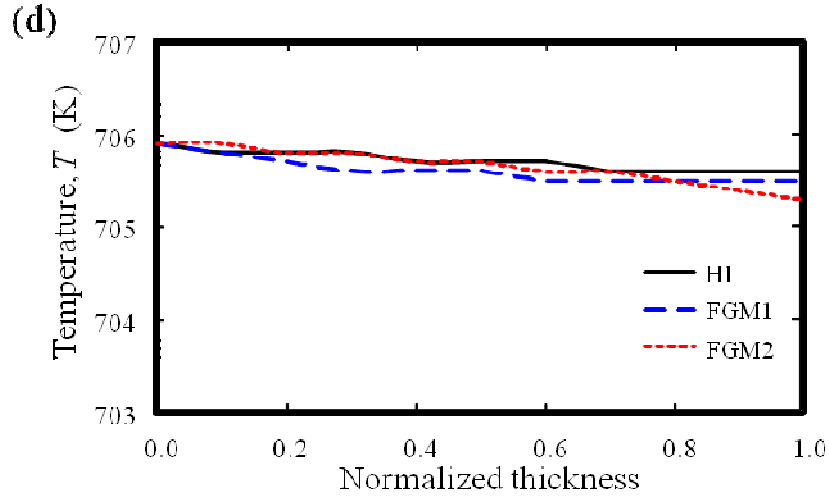
Fig. 5.6 Temperature distribution in pressure vessel along line A-A': (a) t = 0.01s, (b) t = 0.5 s, (c) t = 50 s and (d) t = 600 s.
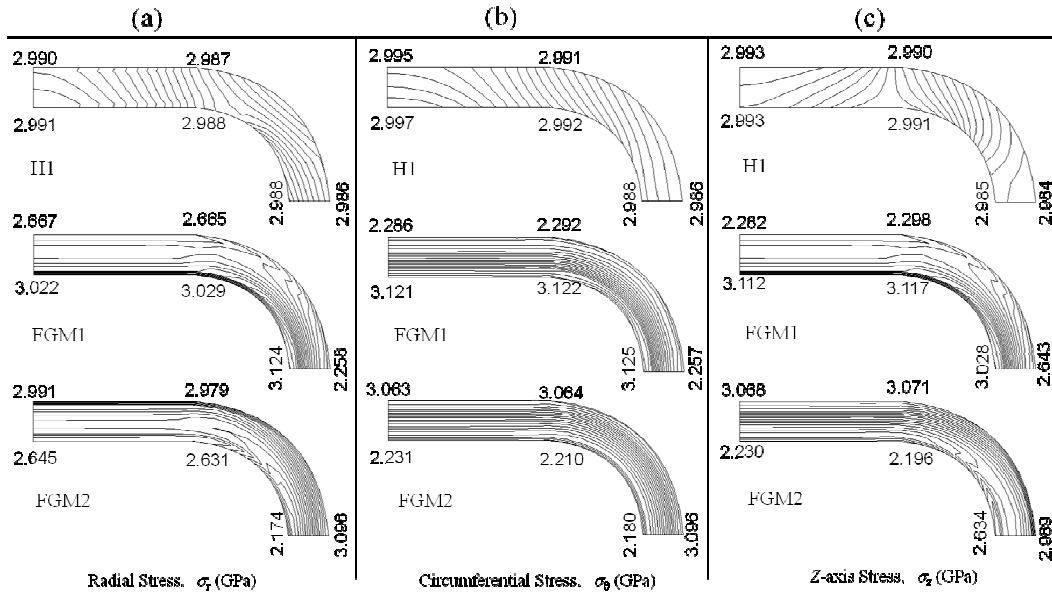

Fig. 5.7 Stress contour line at time t = 10810 s for the H1, FGM1 and FGM2: (a) radial stress, (b) circumferential stress and (c) z-axial stress.

Figures 5.8 and 5.9 indicate the radial stress distributions and the circumferential stress distributions along a line A-A', between the inner and outer surface at the cylinder-end closure junction at different times, respectively. At the early stage of heating, the compressive stress about 2 MPa appears on the inner surface as results of internal pressure. Then, with times change, the compressive stress decreases and the tensile stress appears near the inner surface. The radial stress and circumferential stress in H1 along line A-A' become almost constant with the increasing in temperature. In contrast, the radial stress and circumferential stress in FGM1 and FGM2 are varies widely throughout the inner to outer surface. The effects of FGMs on the stress profiles are clearly observed. Therefore, the necessary gradation of material composition can be readily judged from the initial thickness of pressure vessel and the loading conditions.
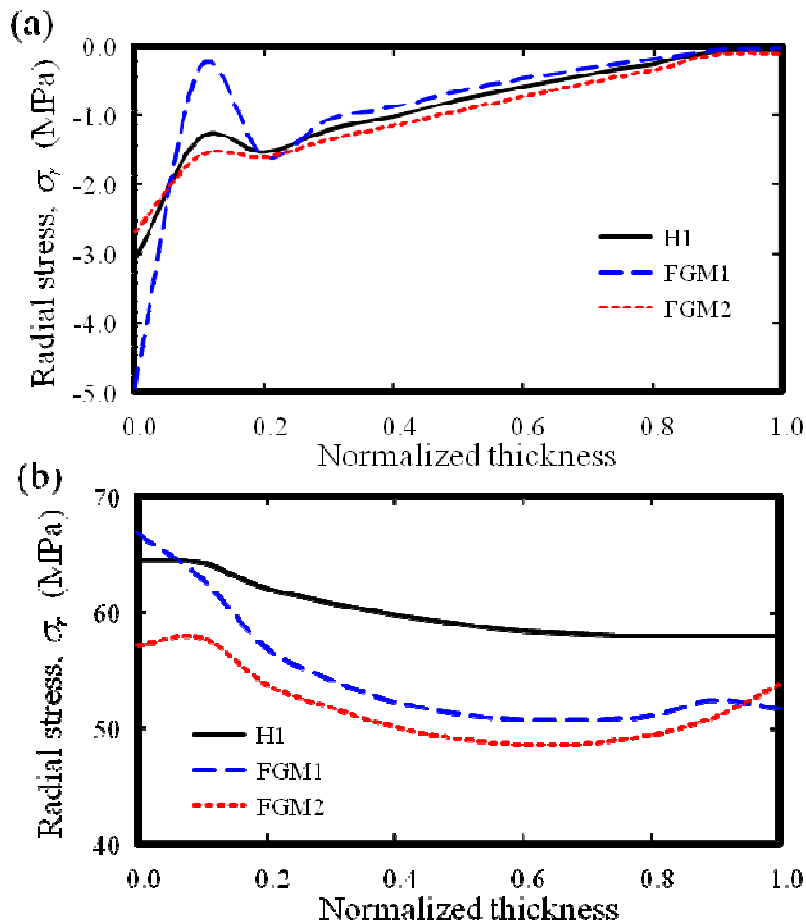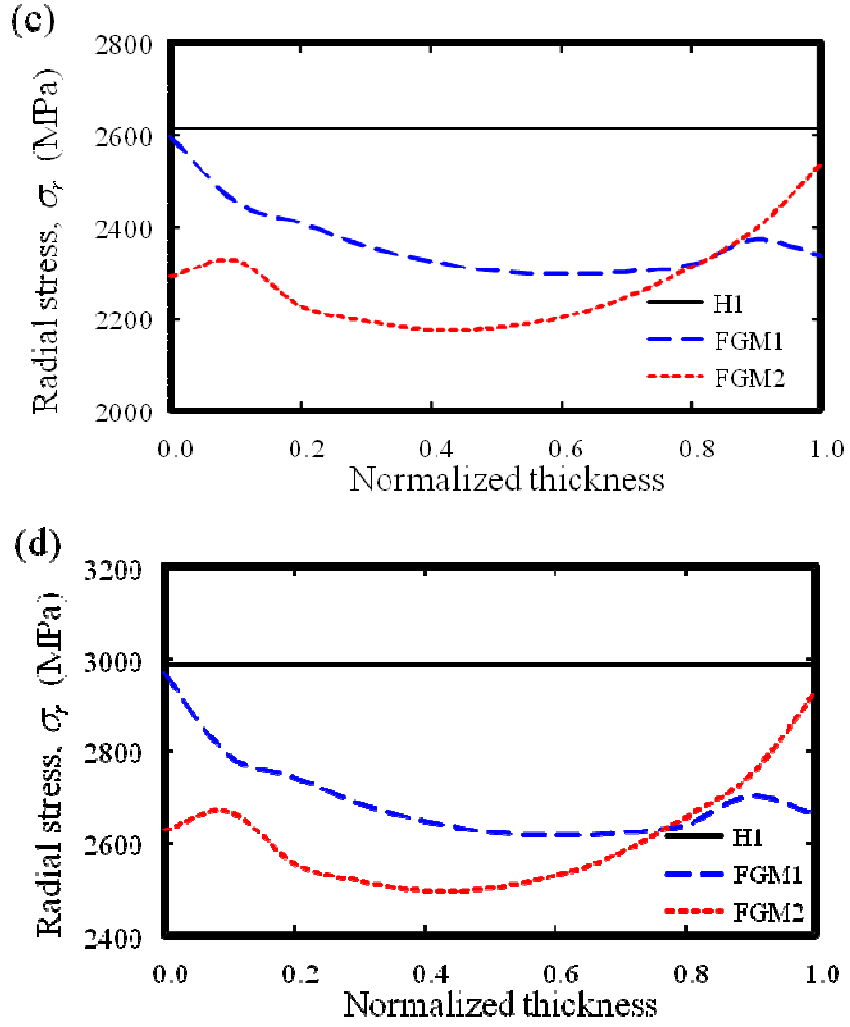

Fig. 5.8 (cont.)

Fig. 5.8 Radial stress distribution in pressure vessel along line A-A': (a) $t = 0.01$s, (b) $t = 0.5$ s, (c) $t = 50$ s and (d) $t = 600$ s.
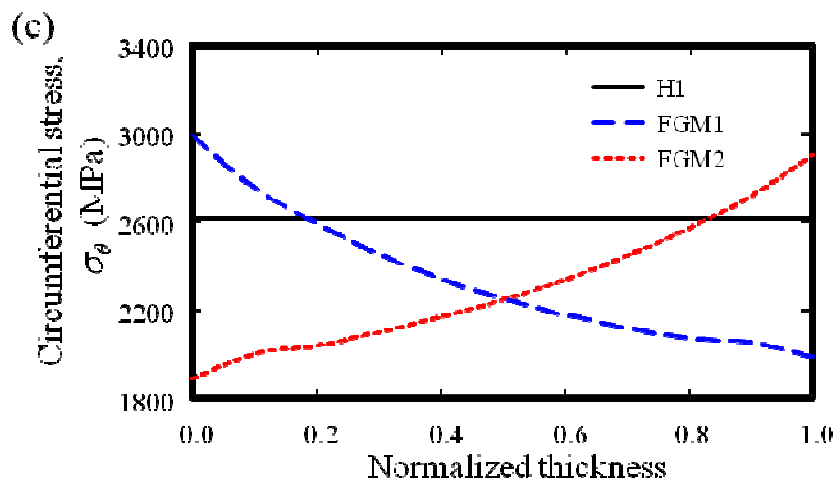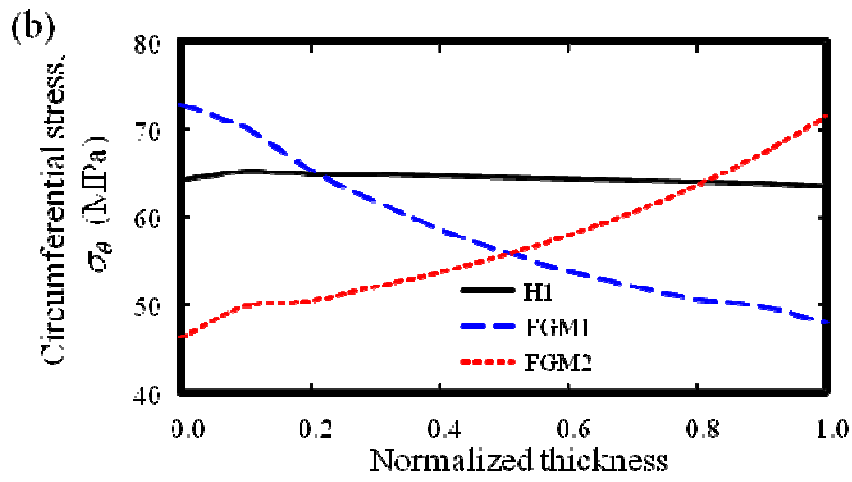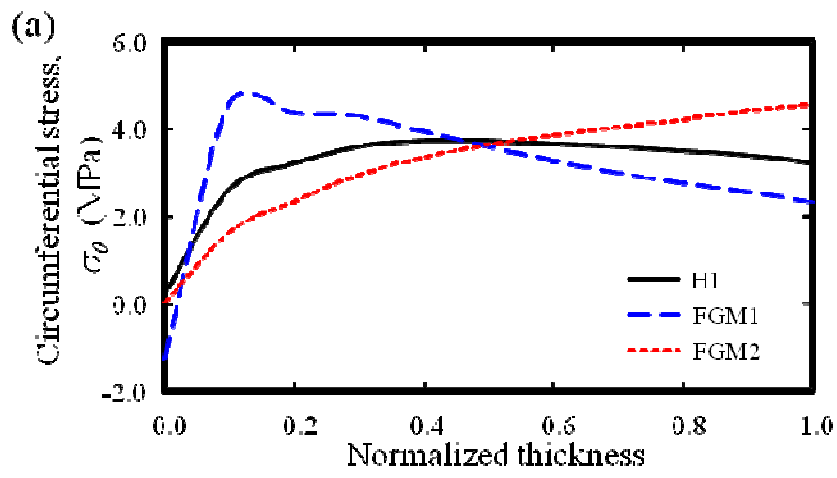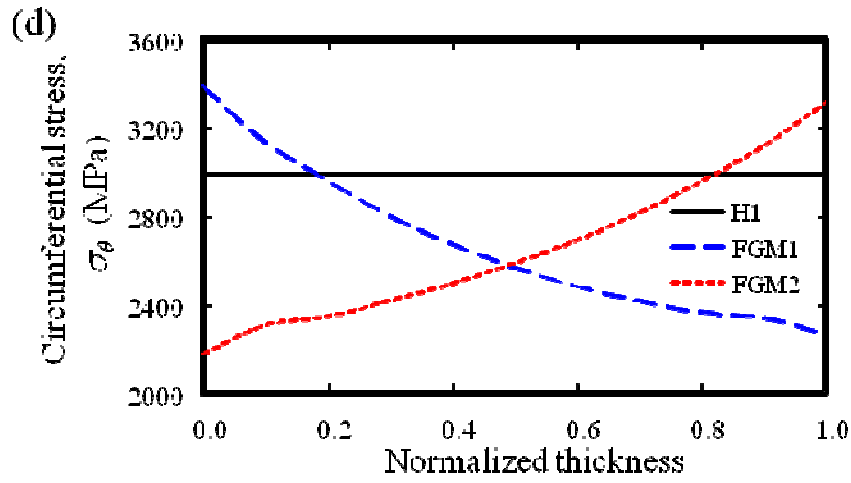
Fig. 5.9 (cont.)

Fig. 5.9 Circumferential stress distribution in pressure vessel along line A-A': (a) t = 0.01s, (b) t = 0.5 s, (c) t = 50 s and (d) t = 600 s.

Figures 5.10(a) and (b) show the variation of radial stress and circumferential stress as a function of time for thick-walled pressure vessels subject to internal pressure and thermal loading with different material compositions at inner and outer surface, respectively. From these figures it may be seen that the radial and circumferential stress at the both surfaces initially increases with time until reach the maximum value and then remain at the steasy state condition. The radial stress at the inner and outer surface in FGM1 and FGM2 are always lower than in H1. In contrast, the circumferential stress in H1 is in the middle between FGM1 and FGM2. However, there is tendency that the circumferential strees at the inner surface of FGM1 and at the outer surface of FGM2 will decreases with further times change.
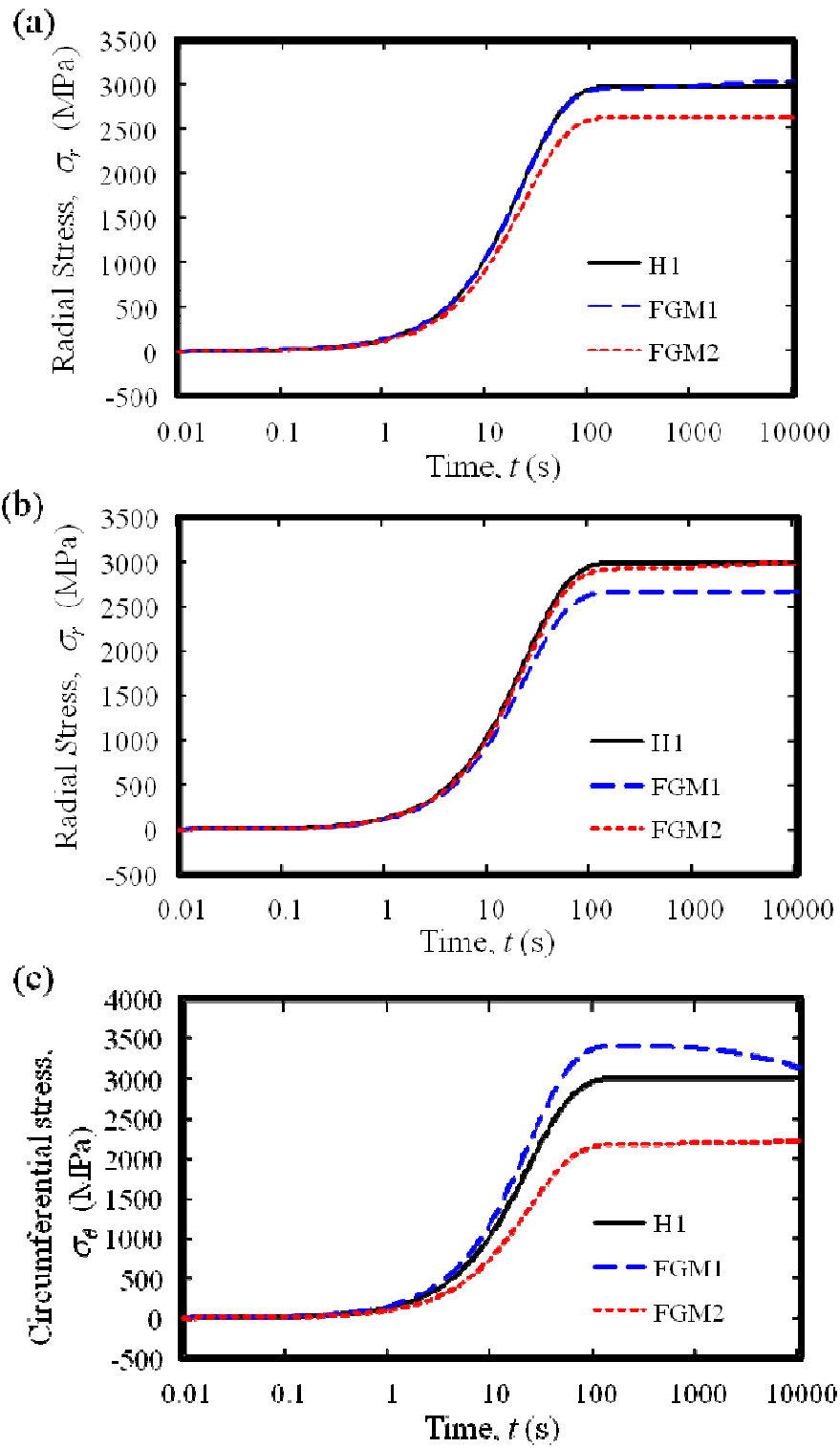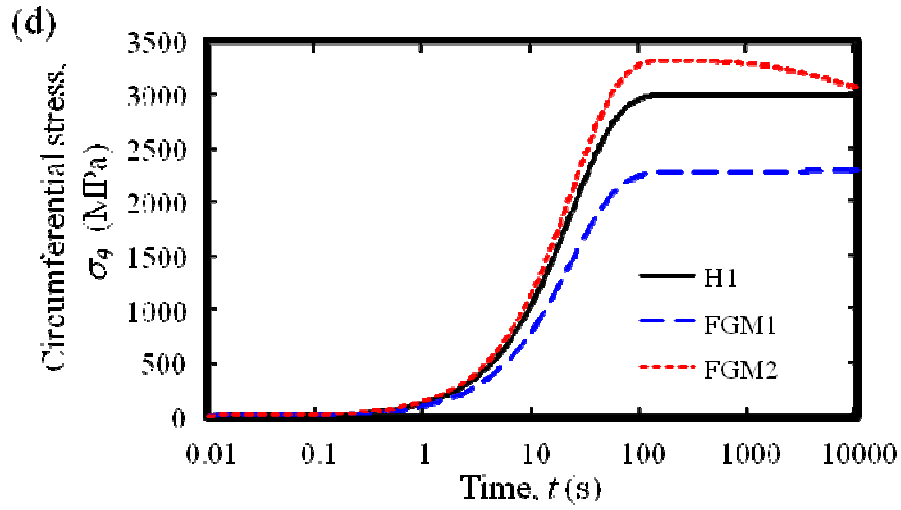
Fig. 5.10 (cont.)

Fig. 5.10 Radial and circumferential stress changes with time at the junction of spherical-end closure of pressure vessels: (a) and (c) at the inner surface, and (b) and (d) at the outer surface.

5.4 Conclusions

A finite element model has been developed to analyze the thermo-visco-plasticity with creep behavior of FGM thick-walled pressure vessels. The validity of the model is verified by comparing the results obtained for a thick-walled pressure vessel of homogeneous isotropic material. Then, it is demonstrated for FGM thick-walled pressure vessels. It is found that the stress distributions in thick-walled pressure vessels are significantly changed if FGMs are used. The gradient in FGM can be tailored to obtain the desired stress distribution in order to change or lower the stress concentration at the critical point that might be initiate the failure of a certain structure. The obtained results show that the promising application of FGMs in pipe and pressure vessels industry.

References

1) Y.Z. Chen and X.Y. Lin: Comp. Mater. Sci. **44** (2008) 581.

2) Y. Fukui and N. Yamanaka: JSME Int. J., Ser. 1 **35** (1992) 379.

3) Y. Fukui, N. Yamanaka and K. Wakashima: JSME Int J. Ser. A **36** (1993) 156.

4) J. Dryden: Int. J. Sol. Struct. **44** (2007) 4158.

5) M. Mohammadi and J. Dryden: Int. J. Sol. Struct. **46** (2009) 788.

6) J. Go, A.M. Afsar and J.I. Song: Adv. Comp. Mater. **19** (2010) 197.

7) O.C. Zienkiewicz and I.C. Cormeau: Int. J. Num. Met.Eng. **8** (1974) 821.

8) H. Tsukamoto: Comp. B **34** (2003) 561.

9) H.J. Frost and M.F. Ashby: *Deformation-Mechanism Maps: The Plasticity and Creep of Metals and Ceramics*, Pergamon Press, New York (1982).

10) K. Wakashima and H. Tsukamoto: in M. Yamanouchi, M. Koizumi, T. Hirai, and I. Shiota (Eds.): Proc. First Int. Symp. FGM, Sendai (1990) p. 19.

11) O.C. Zienkiewicz, S. Valliappan and I.P. King: Int. J. Num. Met.Eng. **1** (1969) 75.

12) G.A.Greenbaum and M.F. Rubinstein: Nuc.Eng. Des. **7** (1968) 379.

Chapter 6

Formation of Compositional Gradient in Al/SiC FGM Fabricated under Centrifugal Force: Solid-Particle Method and Mixed-Powder Method

6.1 Introduction

Centrifugal casting is one of the effective methods for fabrication of particulate-type functional graded material (FGM) [1–2]. Centrifugal casting of particulate reinforced composite is solidification of a suspension of molten alloy and particles under centrifugal force. Particle segregation during casting with the centrifugal casting occurs due to the difference in density between the particles and molten alloy [3]. The particulate-type FGM fabricated by the centrifugal casting showed interesting properties that are not obtained in conventional monolithic materials, such as gradual changes in hardness, wear resistance, Young's modulus, etc [4]. Comparing centrifugal casting method with the other FGM fabrication methods such as chemical vapor deposition, the plasma spray technique and various powder metallurgy techniques, the centrifugal casting method is the easiest and inexpensive to produce relatively large FGM components.

Al/SiC FGM are presently produced by centrifugal casting method. During solidification, the SiC particles are moved to the outer part of spinning mold because of their higher density than the Al melt. The process of SiC segregation evolves together with heat transfer process. The segregation process of SiC particles and the heat transfer process define changes of physical properties in Al melt and these physical properties changes influence the evolution of these two processes [5]. Conventionally, in fabrication of Al/SiC FGM, homogeneous Al/SiC composite ingot is melted at temperature higher than melting temperature of Al in a crucible and then is cast in a spinning mold. This technique is referred to as centrifugal solid-particle method (CSPM)

[6]. Compositional gradient in Al/SiC FGM is formed from the inner surface to outer surface.

Recently, as practical centrifugal casting method, the centrifugal mixed-powder method (CMPM) was developed [2, 7]. It was reported in Watanabe et al. [2] that the CMPM has good prospects in fabrication of functionally graded grindstone for grinding or sharpening tools. In this method, a powder mixture of Al and SiC particles is inserted into a spinning mold. Then, Al ingot is melted and poured into spinning mold with the powder mixture. As a result, the molten Al penetrates into the space between particles by the pressure due to the centrifugal force. At the same time, powder of Al is melted by the heat from molten Al ingot poured from crucible. Finally, an FGM ring with SiC particles distributed on its surface can be obtained.

However, to obtain the compositional gradient desired for certain application is not easy. Many experiments should be conducted by changing casting conditions. The critical processing parameters that decide the final formation of compositional gradient in Al/SiC includes the processing temperature, rotating speed of mold, pouring rate of melts etc. One of the main problems in centrifugal casting is to determine the temperature distribution during casting by experimental techniques as the mold rotates at a very high speed during solidification. In this work, an effort has been made to fabricate Al/SiC FGM by CSPM and CMPM under huge centrifugal force. The centrifugal force of 1120 times of gravity acceleration, G number equal to 1120 G, is considered huge since the common centrifugal force used in centrifugal casting is less than 200 G. Moreover, the final formation of compositional gradient in Al/SiC FGM fabricated is numerically predicted. The validity of the method for engineering the desired composition gradient in Al/SiC FGM is discussed by comparing the simulation results with the experimentally obtained gradient. The effects of different casting conditions on the final formation of compositional gradient in Al/SiC FGM are investigated.

6.2 Microstructure of Al/SiC FGM Fabricated by CSPM and CMPM

6.2.1 Experimental Procedure

The Al/SiC FGMs in hollow cylinder shape were produced by using CSPM and CMPM. Figure 6.1 shows the configuration of the system where the castings were carried out. The chamber was designed to be used under vacuum condition. For Al/SiC FGM fabricated by CSPM, the material used was Duralcan (25 vol. % SiC-Al alloy composite) ingot. The ingot is melted at 1023 K in crucible and then cast in a spinning mold. The mold rotates at 5000 rpm, allows the molten alloy experiences about 1120 times of gravity acceleration. The temperature of mold is kept at 773 K for 10 minutes after the melt ingot completely released from the crucible. Twenty minutes later, the motor speed is reduced to 2500 rpm and kept rotates for one hour. After a day, the fabricated Al/SiC FGM has the outer diameter of 80 mm, the length of 178 mm and thickness of 5 mm is removed out.
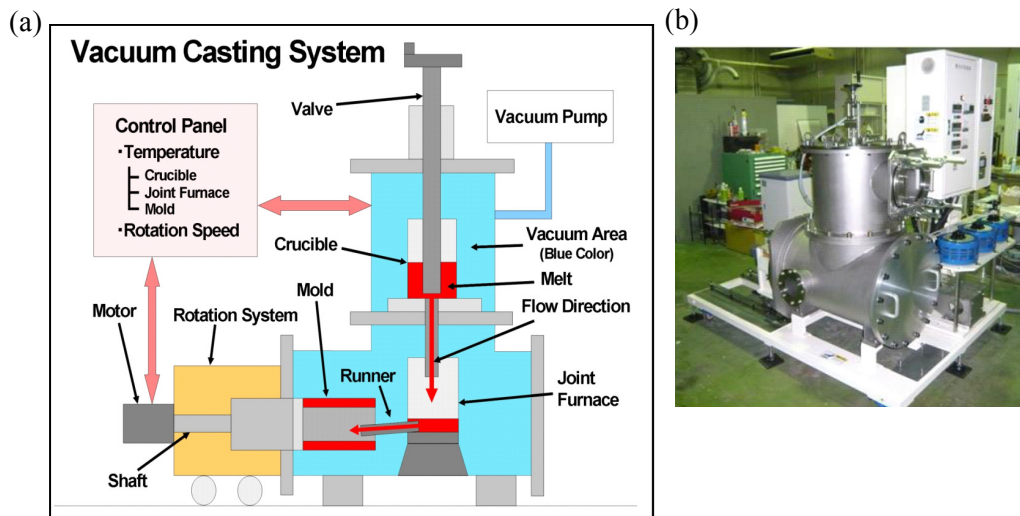

Fig. 6.1 Vacuum centrifugal casting system: (a) the schematic drawing and (b) picture.

In case of CMPM, pure Al ingot is used. A mixture of Al and SiC particles is first inserted into the spinning mold. Then, Al matrix ingot is melted and poured into the spinning mold. The rest casting parameters are same as for CSPM. The diameters of Al and SiC particles are 425-850 μm and 1 μm in average, respectively. The Al/SiC FGM

is also fabricated using SiC particles with average diameter of 30 μm. The Al-20vol.%SiC powder mixture is prepared by mix together 0.032 kg of Al and 0.009 kg of SiC particles.

The microstructures of the Al/SiC FGM are observed using scanning electron microscope (SEM). SEM specimens are cut from the cross-sectional plane and the surface plane of the Al/SiC FGM as shown in Fig. 6.2. For the cross-sectional plane, the specimens are mechanically polished and the compositional analyses on these planes are made by electron-dispersive X-ray spectroscope (EDX) and image analysis software.
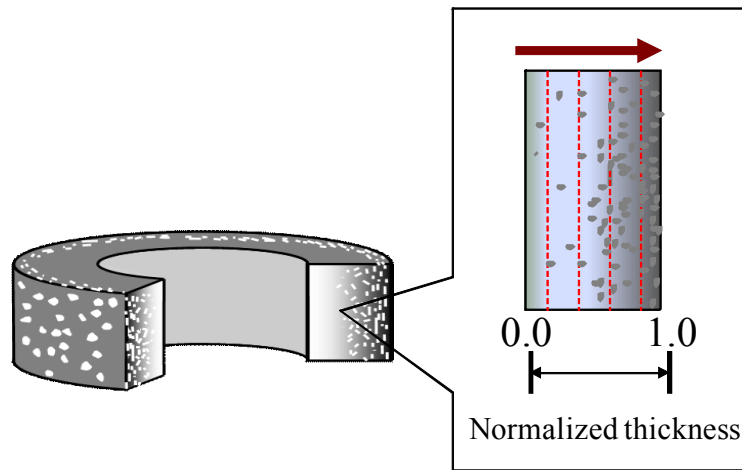

Fig. 6.2 Specimens taken from centrifugal cast materials.

6.2.2 Al/SiC FGM Fabricated by CSPM

Figure 6.3(a) shows the Al/SiC FGM made by the centrifugal solid-particle method. It can be observed from the figure that the obtained FGM has few defects. Two different layers can be observed clearly from the sliced plane of Al/SiC FGM (Fig. 6.3(b)). The outer layer contains richer SiC particles than the inner layer and many voids can be observed in inner layer. The gradient pattern obtained in the casting then is examined by SEM/EDX. Micrographs are taken across the cross-section at various locations and are shown in Fig. 6.4. The Al/SiC FGM thickness is normalized, where 0.0 and 1.0 correspond to the inner and outer peripheries, respectively. It can be seen from the

micrographs that the SiC particles move toward the outer surface and the Si particles move toward the inner surface owing the higher density of SiC and lower density of Si than Al matrix, respectively. It is also seen from the micrographs the trend of SiC particles concentration from the inner surface to the outer surface. Near to the inner surface, there is almost no SiC particle. The SiC particle concentration increased sharply in the middle zone and then almost remained with high SiC particle concentration towards the outer surface. This pattern is different from the patterns of SiC particle concentration in Al/SiC fabricated under low G number [8] for which the SiC particle concentration gradually increases towards the outer surface.
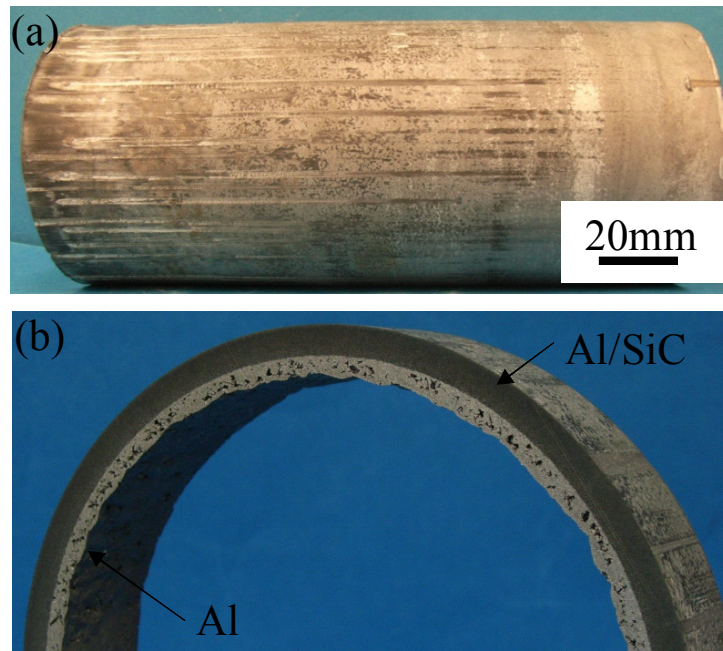

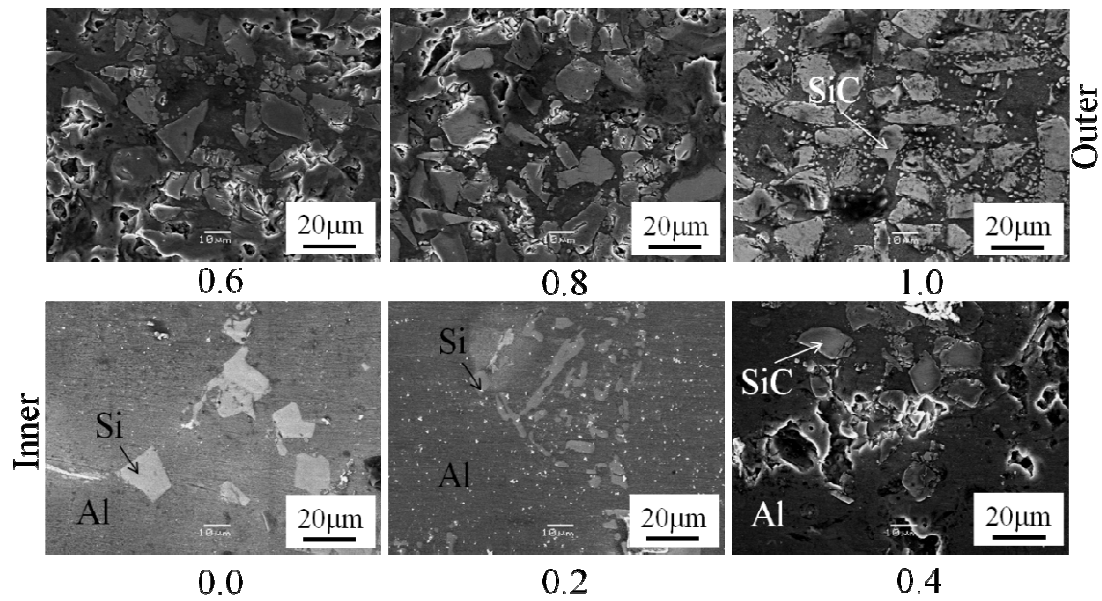Fig. 6.3 Al/SiC FGM fabricated using CSPM.

Fig. 6.4 Microstructures of Al/SiC FGM fabricated by centrifugal solid-particle method (taken at various thicknesses).

Figure 6.5(a) shows the backscatter electron (BE) micrograph on the cross-section of Al/SiC FGM. It can be clearly observed the existence of Si. As comparison, the BE micrograph and the corresponding Al and Si distribution maps of as-received Al/SiC ingot are shown in Figs. 5(b), (c) and (d), respectively. The initial size of Si and SiC particles are approximately about 2 μm and 10 μm, respectively.
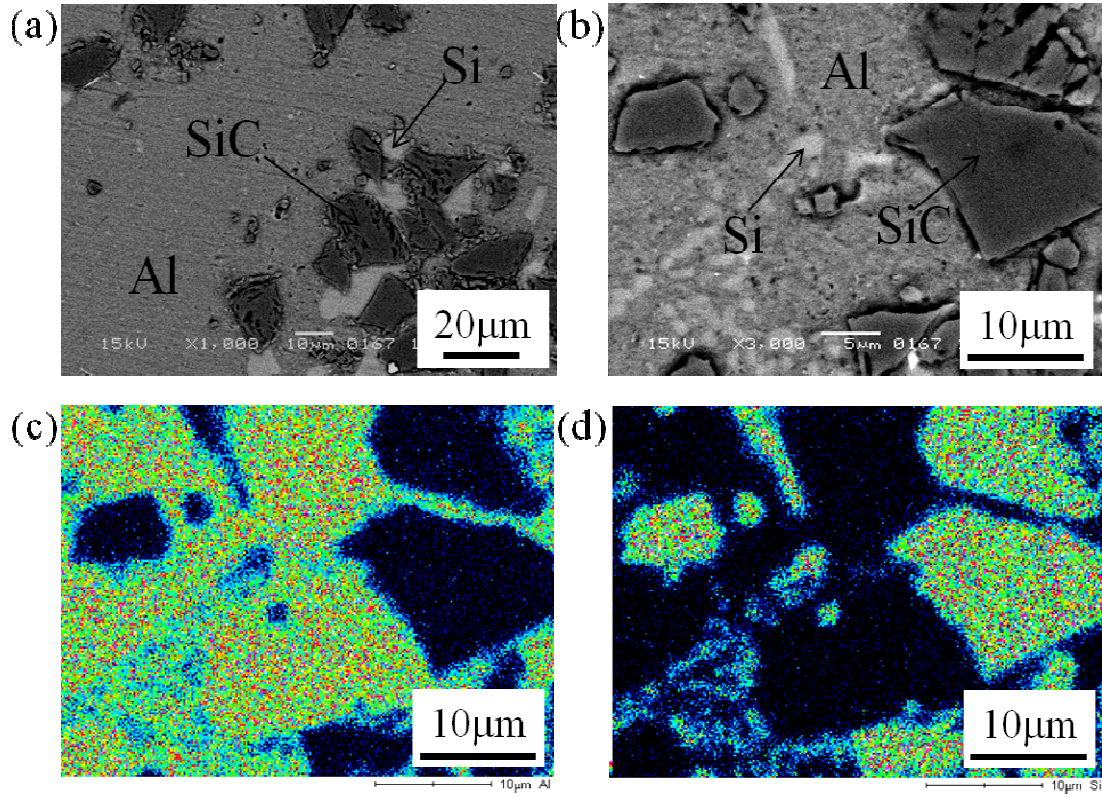
Fig. 6.5 (a) The BE image of Al/SiC FGM fabricated by CSPM. (b) to (e) BE image, the corresponding Al and Si distribution maps and EDX analysis of the as-received Al/SiC ingot, respectively.

6.2.3 Al/SiC FGM Fabricated by CMPM

Figures 6.6(a) and (b) show the overall Al/SiC FGM fabricated by CMPM with the average diameter of SiC particles equal to 1 μm and 30 μm, respectively. The outer surface of the Al/SiC FGM was covered by SiC particles. Observing the SE images of the outer surface of Al/SiC FGM as shown in Figs. 6.7(a) and (b), is found that SiC was agglomerated on the outer surface. Figures 6.7(c) and (d) show the SE image on the cross-sectional surface of the Al/SiC FGM with the average diameter of SiC particles equal to 1 μm and 30 μm, respectively. In case of the average diameter of SiC particles equal to 1 μm, there is no SiC particle on the cross-sectional plane except a layer on the outer surface as a result of high centrifugal force (Fig. 6.7(c)). Meanwhile, in case of SiC

91

particles with the average diameter of 30 μm, few SiC particles are observed at the area near the outer surface, about 1 mm in depth from the outer surface.

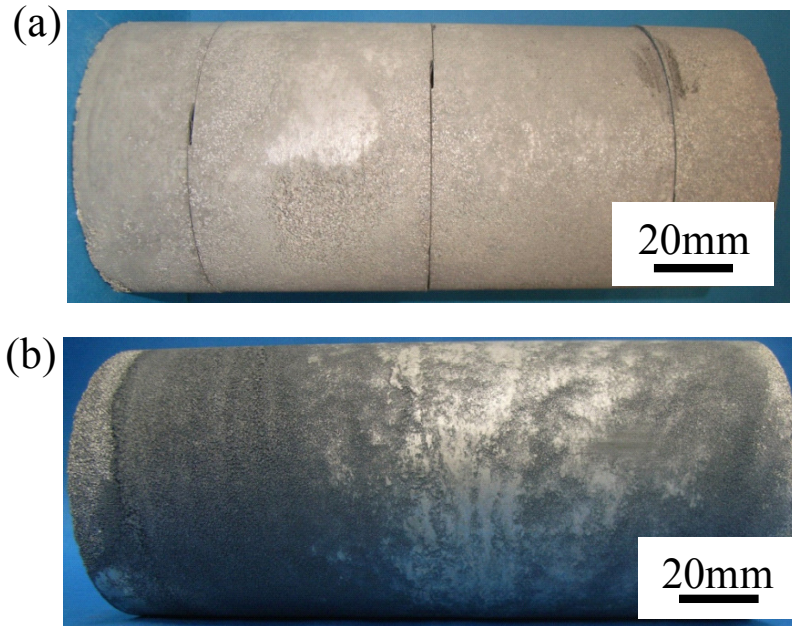Fig. 6.6 Al/SiC FGM fabricated using CMPM with different diameter of SiC particle: (a) 1 μm and (b) 30 μm.

In case of SiC particles with the average diameter of 1 μm, the casting of Al/SiC FGM is also done for different spinning mold speed i.e. 1495 rpm (100 G) and 3500 rpm (550 G). Moreover, Al/SiC FGM is also fabricated at higher molten Al temperature i.e. 1070 K. Although the results are not presented here, no observable difference was found with the results obtained for Al/SiC FGM fabricated with spinning mold speed of 5000 rpm (1120 G) and Al melted at 1020 K. It was reported in previous study [7] that is is difficult to fabricated an FGM containing nano-particles by CSPM, which very small compositional gradient of nano-particle obtained. Instead, as shown in Figs. 6.7(a) to (d), SiC particle can be dispersed homogeneously close to the outer surface of Al/SiC FGM by CMPM regardless the particle size. Interestingly, it is possible to obtain the

compositional gradient of SiC particle in the Al/SiC FGM fabricated with high particle concentration at the outer surface by combining CSPM and CMPM.
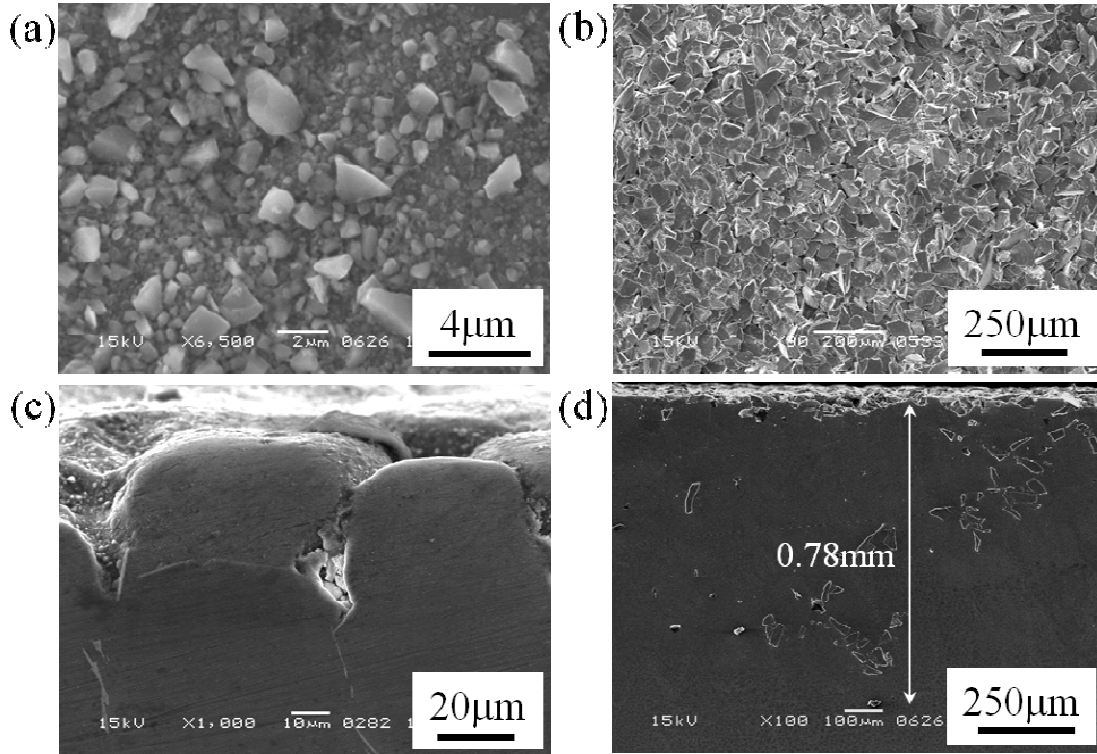

Fig. 6.7 Al/SiC FGM fabricated using CMPM with different diameter of SiC particle. In (a) and (c) the average diameter of SiC is 1 μm and (b) and (d) the average diameter of SiC is 30 μm. (a) and (b) present outer surface, and (c) and (d) show cross-sectional surface.

6.3 Numerical Simulation of Compositional Gradient in Al/SiC FGM

6.3.1 Theory of Simulation

The motion of particles in a viscous liquid under a centrifugal force can be described based on the Stokes' law [1, 8, 9]. Considering the movement velocity of a particle during centrifugal method, the movement velocity of a spherical particle in viscous

liquid depends on position of the ring-shaped mold along radial direction. The movement velocity of particles in viscous liquid can be written as

$$\frac{dx}{dt} = \left|\rho_c - \rho_m\right| \frac{GgD_c^2}{18\eta}$$ (6.1).

Here, dx/dt, ρ, g, G, D and η are velocity, density, gravitational acceleration, centrifugal force, particle diameter and the viscosity of the molten metal, respectively. The subscript indices 'c' and 'm' denotes particle and metal, respectively. The centrifugal force, G is represented as:

$$G = \frac{4r\pi^2 N^2}{g}$$ (6.2)

where r and N are radius of casting mold and velocity of mold rotation, respectively. It is obvious from Eq. (6.1) that the velocity of particles is depended on density and viscosity of molten metal. It is known that these two variables increase according to the temperature drop during solidification. The viscosity of the molten metal also increases according to the increase in number of particles in the suspension. At the same time the temperature distribution is also affected by the changes of physical properties in the molten metal. Therefore in order to predict the formation of compositional gradient in Al/SiC FGM, the process of particle segregation evolves together with heat transfer and phase transformation process. These two processes should be solved simultaneously.

6.3.1.1 Particle segregation process model

The particle movement in this simulation is not considered for an individual particle, but for group of the particles, namely the particle movement is calculated each region in FGM ring divided by same intervals along centrifugal force direction by using volume fraction of solid particles. In addition, it is assumed that particles move only along centrifugal direction. The cylindrical area of casting is divided into a number of cylindrical zones. During the solidification, the change of particle volume fraction in each zone is calculated. The movement of SiC particles in viscous liquid under centrifugal force is calculated by Eq. (6.1). With considering the suspension of particles in molten metal, the viscosity of molten metal can be written as [10]

94

$$\eta = \frac{\eta_0}{\left(1 - V/V_{\max}\right)^{5/2}} \tag{6.3}.$$

Here, η_0, V, and $V_{\max}$ are the viscosity of molten metal without particles, the volume fraction of particle and the maximum containable volume fraction of solid particles, respectively. The $V_{\max}$ depends on the packing condition of solid particles in molten metal. It is known that theoretical value with even sphere particle case is ranged from 0.52 for simple cubic packing to 0.74 for close packing. Moreover, the viscosity of molten metal is also influenced by temperature [11]. The relationship between viscosity and temperature is given by

$$\eta = \eta_0 \exp\left(\frac{Q}{RT}\right) \tag{6.4}$$

where Q and R are the activation energy and the gas constant, respectively. The relationship between the density of Al liquid and temperature is given by [12]

$$\rho = 2377.23 - 0.311(T - T_{\text{ref}}) \quad \text{kg/m}^3 \tag{6.5}$$

T_{ref} is reference temperature and equal to 993.47 K.

6.3.1.2 Heat conduction process model

The analysis is conducted by solving the heat conduction equation and segregation of particles equations simultaneously. Finite element method (FEM) is used in determining the temperature distribution. The Al/SiC FGM fabricated is a geometric symmetry about a reference axis and can be solved using two-dimensional elements for an example 4-node rectangular element shown in Fig. 6.8(b). Therefore, the cast can then be represented by axisymmetric ring elements and analyzed in a similar fashion to that of a two-dimensional problem ($r - z$ plane) as shown in Fig. 6.8(a). In order to determine the temperature distribution at time t, a heat conduction equation of the following form is analyzed

$$\rho c_p \frac{dT}{dt} = \frac{d}{dr} k_r \frac{dT}{dr} + \frac{k_r}{r} \frac{dT}{dr} + \frac{d}{dz} k_z \frac{dT}{dz} + HG \tag{6.6}.$$

Here, c_p, k and *HG* are the specific heat, heat conductivity and heat generated, respectively. For the phase transformation, the simple enthalpy method is implemented. The ρc_p in Eq. (6.5) is replaced by effective heat capacity, c_{eff} given by

$$c_{\text{eff}} = \rho(c_p)_s \quad \text{for } T < T_s,$$

$$c_{\text{eff}} = \rho(c_p)_f + \frac{L}{T_l - T_s} \quad \text{for } T_s < T < T_l, \text{ and}$$

$$c_{\text{eff}} = \rho(c_p)_l \quad \text{for } T > T_l \tag{6.7}$$

where $(c_p)_f$ is specific heat in the mushy zone. The superscripts 's' and 'l' are denote solid and liquid, respectively. The boundary conditions (BCs) on casting surface and mold surface are incorporated in finite element formulation. The detail explanation on these BCs can be found in [3]. The simplest phase, ϕ state equation [5, 14] is assumed

$$\phi = \frac{T_l - T}{T_l - T_s} \tag{6.8}$$

The material properties of FGMs at each integration points, (ξ, ζ) are determined by the rule of mixture as a function of the particle volume fraction discussed in previous section. An exceptional for the thermal conductivity, k is determined based on micromechanical consideration [15] is expressed as

$$k = V_m k_m + V_c k_c + V_m V_c \frac{k_m - k_c}{V_m + 3k_m / k_c} \tag{6.9}$$
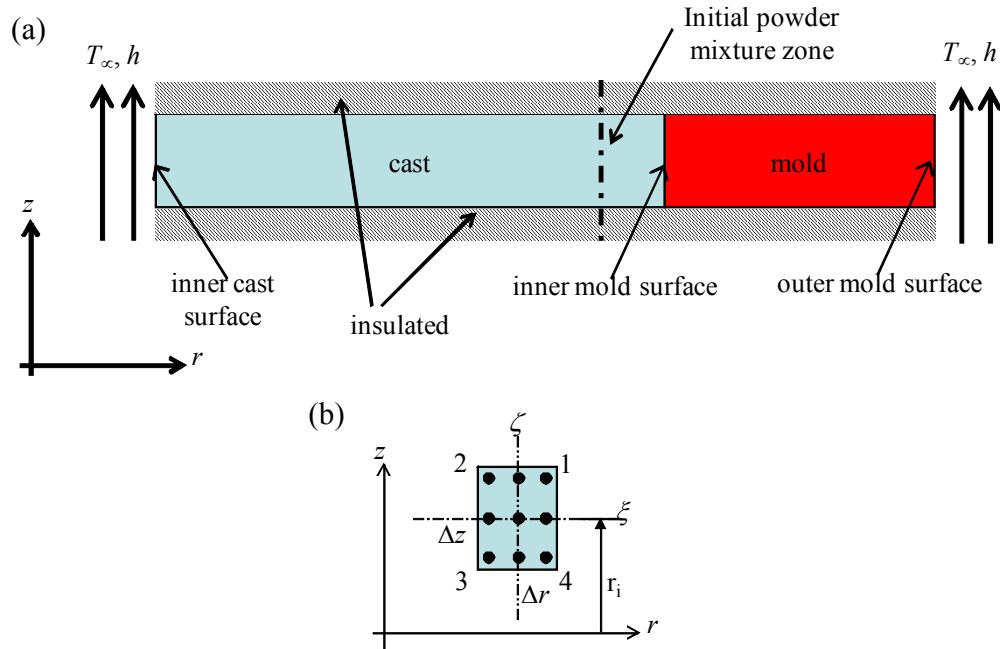
Fig. 6.8 Axisymmetrical solidification problem: (a) overall model and (b) a 4-node rectangular element with nine integration points.

6.3.2 Compositional Gradient in Al/SiC FGM Fabricated by CSPM

The computer simulation is performed using a code developed in FORTRAN based on the theory explained in Section 6.3.1. The material properties and relevant data are given in Table 6.1. Considering the ratio of the thickness to the length of the FGM is too small, only a small cross-sectional plane at the middle of Al/SiC FGM is modeled as shown in Fig. 6.8(a). The thickness of cast and mold are 5 and 2 mm, respectively. The packing limit of volume fraction is set to be 0.43. The initial volume fraction of SiC and Si are set to be 0.2 and 0.1, respectively. To simplified the problem, the particles size assumed remain unchanged during solidification.

Table 6.1 The list of relevant data for casting simulation

Parameter	Value and dimension	Parameter	Value and dimension
Outer mold radius	0.042 m	Inner mold radius	0.04 m
Specific heat of Al liquid	1180 J/kg-K	Specific heat of Al solid	870 J/kg-K
Thermal conductivity of Al liquid	151 W/m-K	Thermal conductivity of Al solid	210 W/m-K
Viscosity of Al liquid	0.257×10^{-3} Pa/s	Latent heat	386 kJ/kg
Solidus temperature of Al	853 K	Liquidus temperature of Al	893 K
Thermal conductivity of steel mold	38 W/m-K	Specific heat of steel mold	460 J/kg-K
Density of steel mold	7870 kg/m^3	Initial mold temperature	773 K
Heat convection coefficient	60 – 200 W/m^2-K	Initial mixed-powder temperature	773 K
Radiation coefficient of Al	0.44	Radiation coefficient of steel mold	0.9
Density of SiC	3230 kg/m^3	Density of Si	2329 kg/m^3
Specific heat of SiC	670 J/kg-K	Specific heat of Si	794 J/kg-K
Thermal conductivity of SiC	77.5 W/m-K	Thermal conductivity of Si	130 W/m-K

Simulation is first performed under conditions same as used in experiments for Al/SiC FGM fabricated using CSPM. Al/SiC FGM is fabricated under the vacuum condition with initial molten ingot temperature of 1023 K, centrifugal force of 1120 G and mold temperature of 773 K. Figure 6.9(a) show the cooling curves calculated at the inner surface of cast and at the inner and outer surface of mold for 1 s. The corresponding temperature distributions along the thickness of the cast at different time are shown in Fig. 6.9(b). As can be observed the temperature of cast and mold reached

the equilibrium temperature in less than 1 s. The final formations composition gradient of the Al/SiC FGM by simulation and experiment are shown in Fig. 6.9(c). Better agreement is observed between the trend of SiC particles distribution in simulation and experiments. From this figure, the steeper particle gradient along the radius direction can be observed. Such gradient type is appropriate gradient for the grinding wheel.
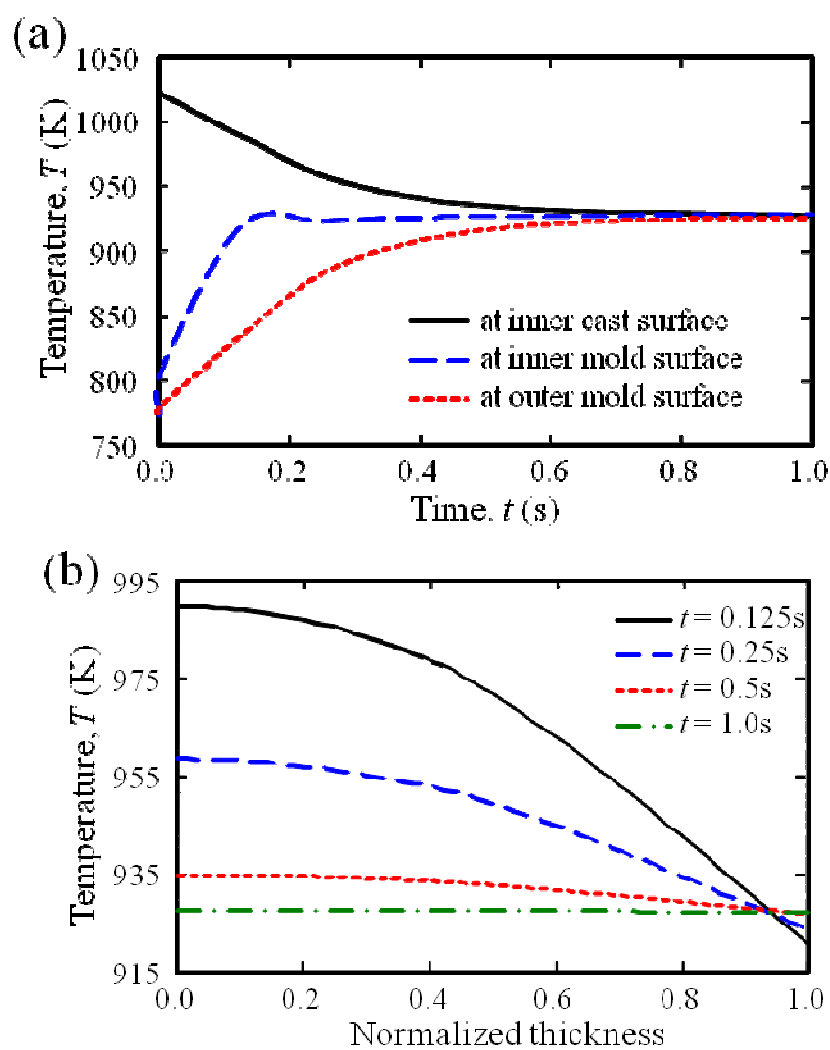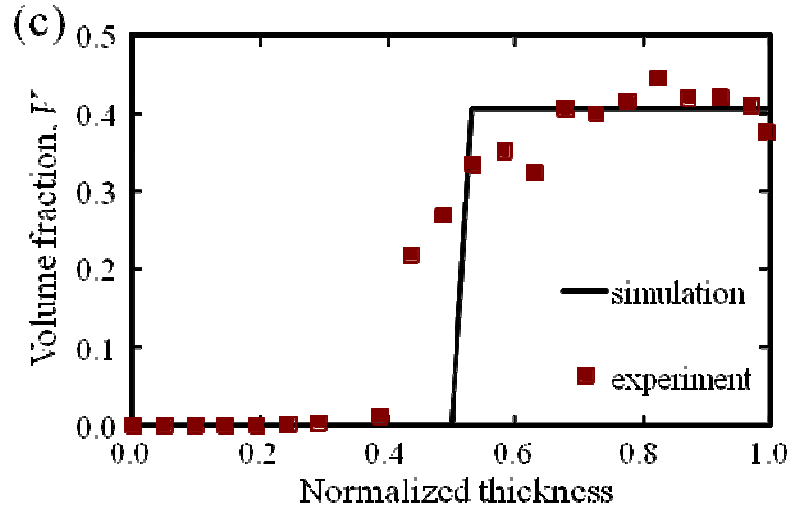

Fig. 6.9 (cont.)

Fig. 6.9 The simulation results of casting Al/SiC FGM using CSPM under vacuum condition, 1120 G, mold temperature of 773 K and ingot temperature of 1023 K: (a) casting cooling curve for 1 s, (b) the corresponding temperature distribution along the thickness, and (c) the final composition gradient of Al/SiC FGM.

Then, the numerical analysis is done to investigate the effects of various casting conditions on the composition gradient of Al/SiC FGM. Here, the main purpose is to investigate the effects of mold temperature and initial ingot temperature on the composition gradient of Al/SiC FGM under 1120 G and vacuum condition. However, the effects of casting atmosphere and different G number on the composition gradient of Al/SiC FGM are also investigated. Two different heat BCs are considered i.e. radiation (vacuum) and heat convection. For convective BCs, the simulation is carried for three different values of heat transfer coefficient, h to describe different casting atmospheres such as normal air and argon. The three convective BCs are h100-h100 (100 W/m^2-K for both at inner cast and outer mold surface), h200-h200 (200 W/m^2-K for both at inner cast and outer mold surface) and h60-h130 (60 W/m^2-K and 130 W/m^2-K at inner cast and outer mold surface, respectively).

Figures 6.10(a) to (f) show the formation of compositional gradient of Al/SiC FGM fabricated by CSPM under various conditions. In these figures, only the volume fraction of SiC particles in function of normalized thickness is shown. From these figures, it is found that the effects of initial ingot temperature, casting atmosfere and G number on the compositional gradient of Al/SiC FGM fabricated at high mold temparature (773 K) are less significant than that fabricated at low mold temperature (573 K). It is also found that the gradient of particle volume fraction increases with increase of the centrifugal force and initial ingot temperature.
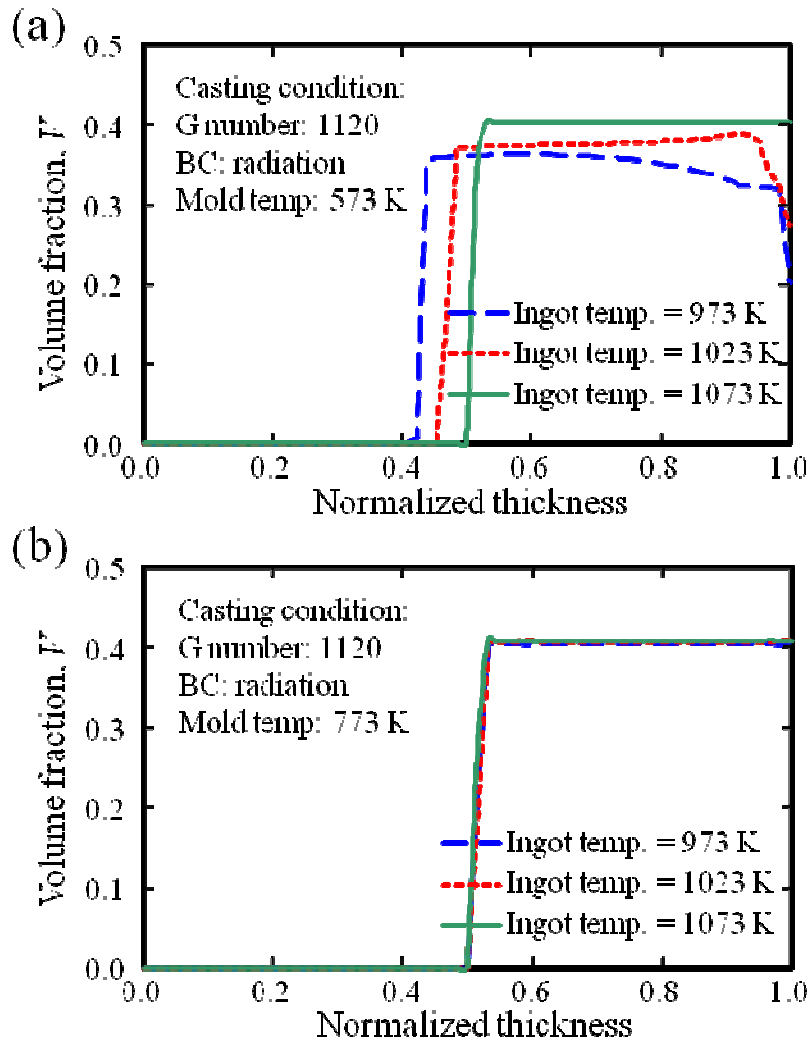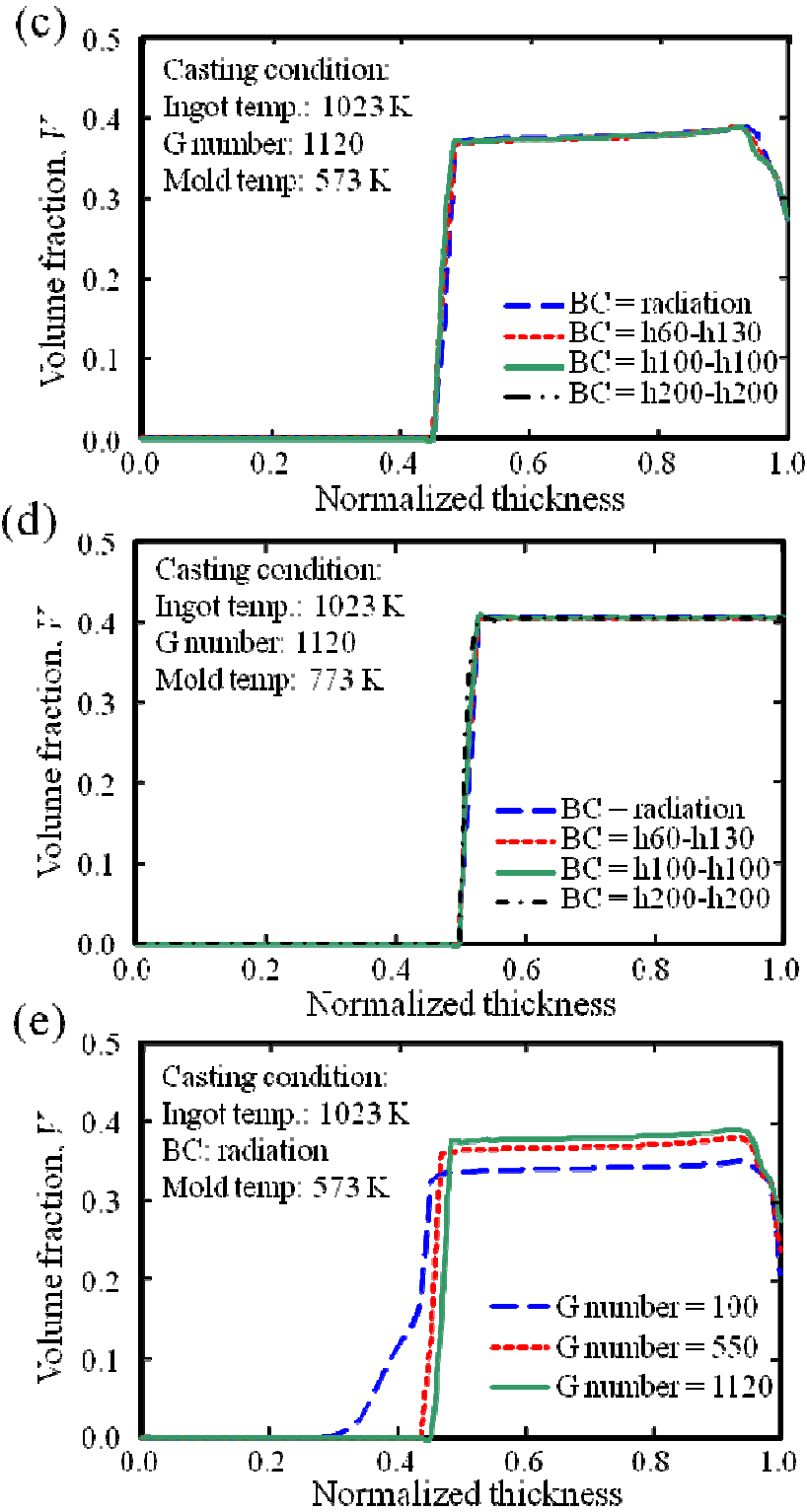

Fig. 6.10 (cont.)

(c) Casting condition:
Ingot temp.: 1023 K
G number: 1120
Mold temp: 573 K

BC = radiation
BC = h60-h130
BC = h100-h100
BC = h200-h200

(d) Casting condition:
Ingot temp.: 1023 K
G number: 1120
Mold temp: 773 K

BC = radiation
BC = h60-h130
BC = h100-h100
BC = h200-h200

(e) Casting condition:
Ingot temp.: 1023 K
BC: radiation
Mold temp: 573 K

G number = 100
G number = 550
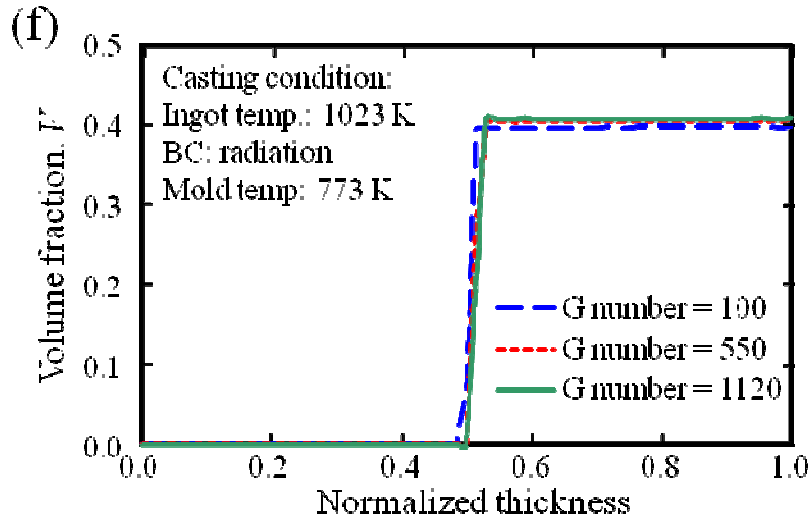G number = 1120

Fig. 6.10 (cont.)

102

Fig. 6.10 The distribution of Si/SiC particle in Al/SiC FGM fabricated by CSPM: (a) and (b) with different initial ingot temperatures, (c) and (d) with different BCs, and (e) and (f) under different G numbers.

6.3.2 Compositional Gradient in Al/SiC FGM Fabricated by CMPM

The simulation for Al/SiC FGM fabricated by CMPM is similar with the simulation conducted for Al/SiC FGM fabricated by CSPM. Here, the mixture of SiC and Al powder, Al-20vol.%SiC, are placed inside the mold before casting. The mixture filled the inner mold with the thickness of 0.38 mm. The packing limit of volume fraction is set to be 0.6. Figure 6.11(a) shows the cooling curve at the inner surface of cast, initial mixture powder zone and outer surface of mold during solidification process under the vacuum condition with initial molten Al temperature of 1023 K and centrifugal force of 1120 G. As can be observed, the temperature of initial mixed powder zone raised from 773 K to above 900 K in less than 1 s. At this point, the powder of Al is melted by the heat from molten Al ingot and then SiC particles start move to the outer periphery with the relative time spent. The temperature distributions along the thickness of the cast at different time t are shown in Fig. 6.11(b). Comparing this figure with Fig. 6.9(b), there is

small different in temperature distribution as a result of different composition gradient of the Al/SiC FGM.
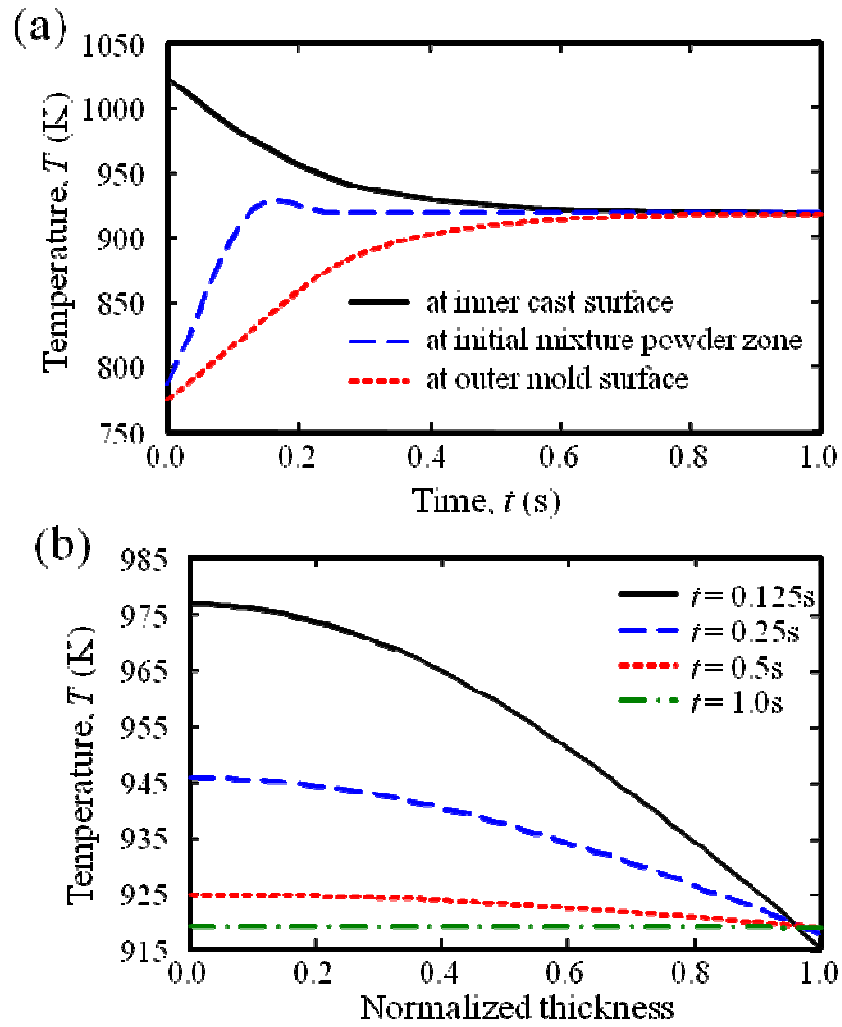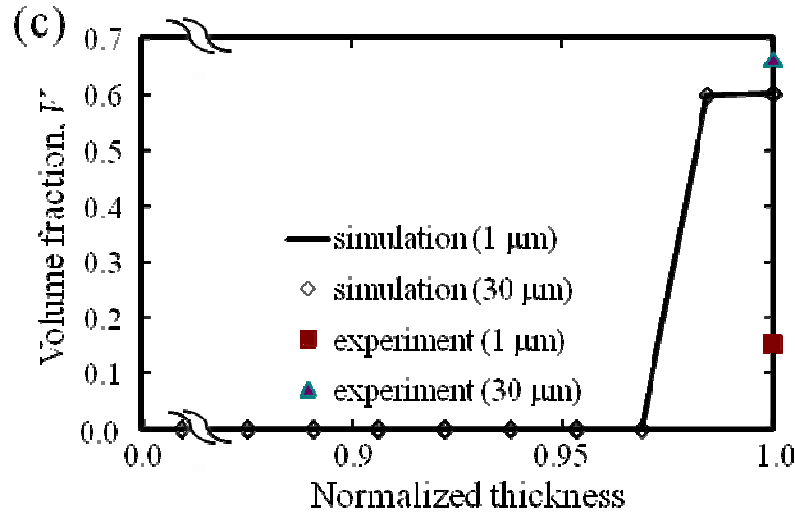

Fig. 6.11 (cont.)

Fig.6.11 The simulation results of casting Al/SiC using CMPM under the vacuum condition, 1120 G, mold temperature of 773 K and ingot temperature of 1023 K: (a) casting cooling curve for 1 s, (b) the corresponding temperature distribution along the thickness, and (c) the final formation composition gradient of Al/SiC FGM.

The numerical and experimental final formation of composition gradient of the Al/SiC FGM fabricated by CMPM are shown in Fig. 6.11(c). A partcile free zone can be cleary seen with all particles concentrates at near the outer surface. It can be seen that, regardless the size of SiC particles, the similar composition gradient in Al/SiC FGM can be obtained. Comparing the volume fraction of SiC at the outer surface calculated in simulation with the experimental results, good agreement is showed in case of SiC particle size of 30 μm (also Fig.6.7(d)) but not in case of SiC particle size of 1 μm. The difference between experimental and simulation is mainly as the result of assumption made in simulation that all SiC particles are fixed in Al matrix. Experimentally, in case of SiC particle size of 1 μm, when the Al/SiC FGM removed from the mold, there are many SiC particles dropped out and some particles at the outer surface are easily removed.
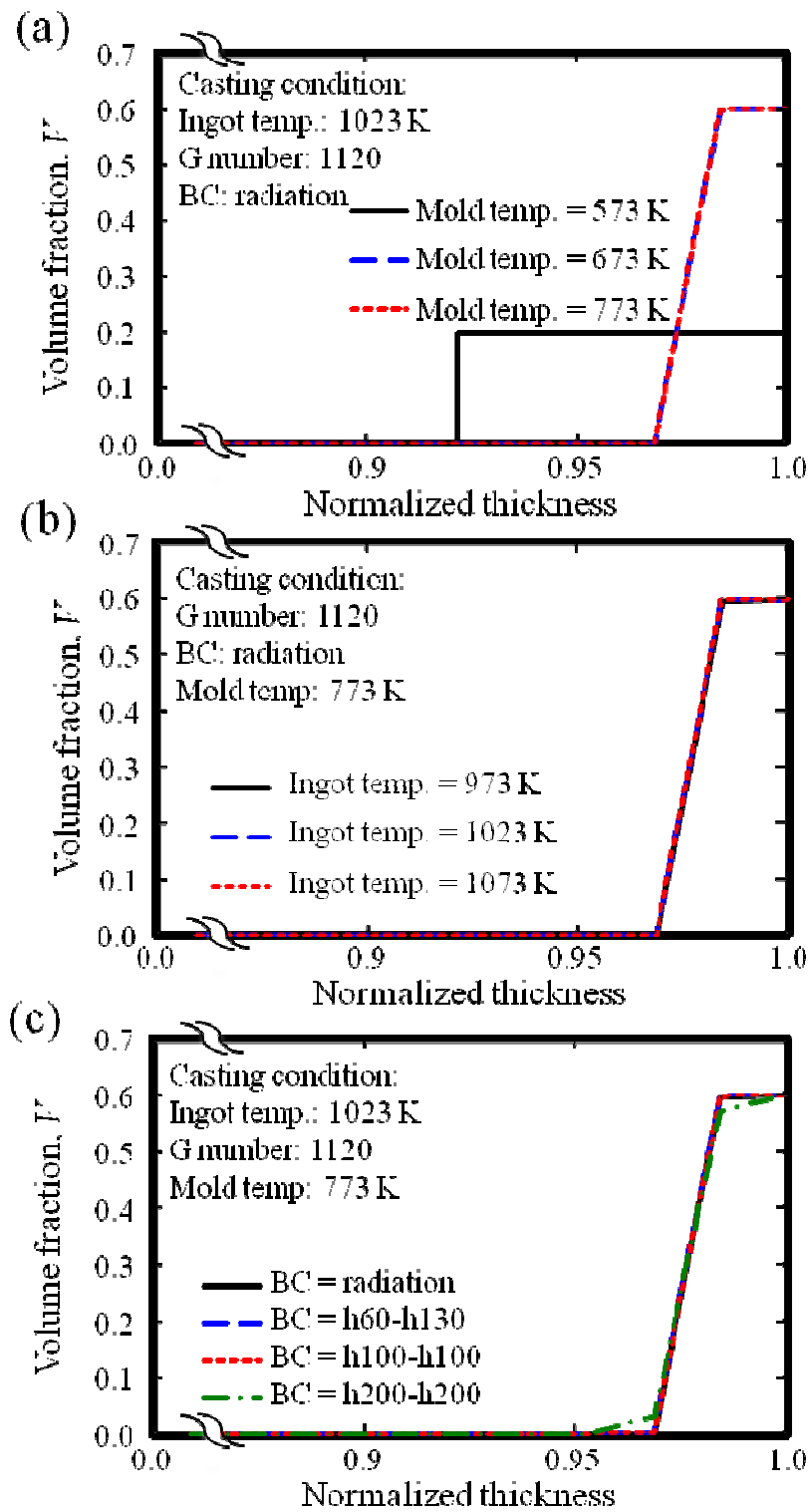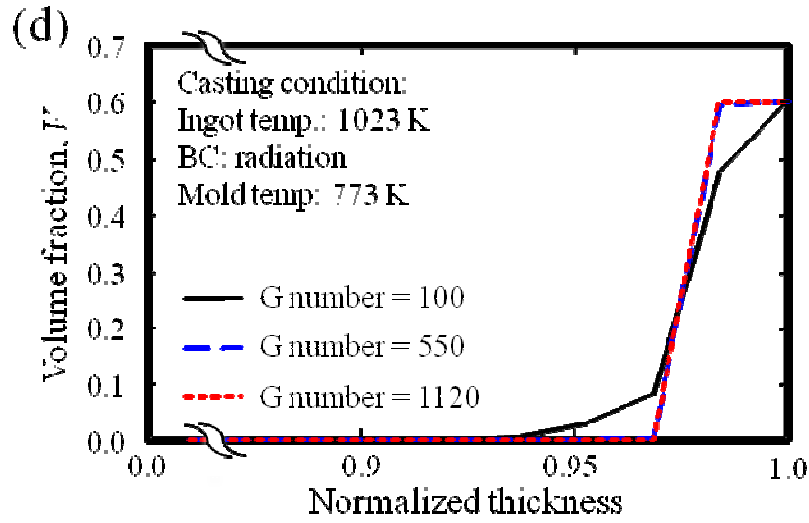
Fig 6.12 (cont.)

Fig. 6.12 The distribution of Si/SiC particle in Al/SiC FGM fabricated by CMPM: (a) with different mold temperatures, (b) with different initial ingot temperatures, (c) with different BCs, and (d) under different G numbers.

Figures 6.12(a) to (d) show the formation of compositional gradient of Al/SiC FGM fabricated by CMPM under various conditions. From these figures, it is found that there are no significant differences in the gradient of particle volume fraction in Al/SiC FGM fabricated by CMPM under huge centrifugal force with different initial temperatures of molten Al and casting atmospheres. However, there is possibility to have gradual gradient of particle volume fraction by decreasing mold temperature and G number.

6.4 Conclusions

A computer code to simulate the formation of compositional gradient in an Al/SiC FGM manufactured by CSPM and CMPM has been developed. The gradient pattern of SiC particles in aluminum matrix were analyzed at various time steps using simulation and the final formation are compared with the results obtained from experiments to validate the theory. The code developed for performing the numerical simulation is formulated in a simple manner. Therefore the parameters in code can be easily varied and thus can be employed to any type of particulate FGM systems. From the obtained results, it is found that the SiC particles can be dispersed on the surface or graded from inner to outer

107

surface of Al/SiC FGM by CMPM or CSPM, respectively. Moreover, unlike Al/SiC FGM fabricated under low centrifugal force, the graded distribution in Al/SiC FGM under huge centrifugal force is not strongly affected by the initial temperature of molten Al and casting atmosphere.

References

1) Y. Watanabe, N. Yamanaka and Y. Fukui: Comp. A **29A** (1998) 595.

2) Y. Watanabe, Y. Inaguma, H. Sato and E. Miura-Fujiwara: Mater. **2** (2009) 2510.

3) L. Lajoye and M. Suery: in S.G. Fishman and A.K. Dhingra (Eds.): Proc. Int. Symp. On Advances in Cast Reinforced Metal Composites, ASM International, Chicago (1988) p. 15.

4) Y. Watanabe, R. Sato, I.S. Kim, S. Miura, and H.Miura: Mater. Trans. **46** (2005) 944.

5) L. Drenchev, J. Sobczak, S. Malinov and W. Sha: Modeling Simul. Mater. Sci. Eng. **11** (2003) 635.

6) Y. Fukui : JSME Int.J. Series III **34** (1991) 34.

7) Y. Inaguma, H. Sato, and Y. Watanabe: Mater. Sci. Forum **631-632** (2010) 441.

8) Y. Fukui and Y. Waranabe: Metall.Mater. Trans. A **27A** (1996) 4145.

9) C.G. Kang and P.K. Rohatgi: Metall. Mater. Trans B **27B** (1996) 277.

10) H.C. Brinkman: J. Chem. Phys. **20(4)** (1952) 571.

11) A.T. Dinsdale and P.N. Quested: J. Mater. Sci. **39(24)** (2004) 7221.

12) M.J. Assael, K. Kakosimos, R.M. Banish, R. Brooks, P.N. Quested, K.C. Mills, A.Nagashima, Y. Sato and W.A. Wakeham: J. Phy. Chem. Ref. Data **35(1)** (2006) 285.

13) T.R. Hsu: The finite element method in thermomechanics, Allen and Unwin, Boston (1986).

14) L. Drenchev, J. Sobczak, S. Malinov and W. Sha: Modeling Simul. Mater. Sci. Eng. **11** (2003) 651.

15) H. Tsukamoto: Mater. Sci. Eng. A **527** (2010) 3217.

Chapter 7

Summary and General Conclusions

In Chapter 1, a general introduction about functionally graded materials (FGMs) concepts, their fabrications and applications are presented. Moreover, the approaches to handle the material properties gradient of FGMs in numerical analysis are explained.

In Chapter 2 and Chapter 3, FGMs was proposed in severe plastic deformation of difficult-to-work materials using equal channel angular pressing (ECAP) at ambient temperature. As subject of study, ECAP billet was prepared by embedded Ti as difficult-to-work materials into Al-based FGM. First, in Chapter 2, the ECAP process of this billet was simulated using finite element method (FEM). Then, in Chapter 3, the experimental work was carried out to confirm the workability of the proposed technique. From the stress-strain distribution predicted by FEM, the appropriate FGMs gradient, position and the condition of ECAP process were determined. Experimentally, the microstructure and hardness of ECAPed specimens were investigated. The changes in microstructure and the increase in the hardness value of Ti with increased number of ECAP passes are evidences showing that Ti is successfully deformed by this technique.

In Chapter 4, the new type of crash box was designed. Instead of homogeneous material, FGMs were used to fabricate a crash box. An FGM crash-box was proposed to improve the crash worthiness and to reduce the body weight. FGM crash boxes with different stepwise strength gradient in longitudinal direction were designed and analyzed by FEM. Crash behavior of this crash-box under quasi-static compressive loads and impact loading was studied. The obtained load-displacement curves then were evaluated to assess the effect of the stepwise strength gradient of the crash-box. High crash energy absorption can be achieved by the proposed FGM crash-box. Folding pattern can be pre-set by using FGM crash-box to improve the safety of passengers during accident.

In Chapter 5, the analysis of thermo-visco-plasticity and creep characteristics of the FGM thick-walled pressure vessels was carried out using FEM. The material properties

of FGMs were continuous functions of volume fraction of material composition. The obtained results show that the material composition significantly affects the effective stress as a function of time at the inside and outside surface of thick-walled cylinder. The use of FGMs can adjust the stress distribution in the structure.

In Chapter 6 the formation of compositional gradient in Al/SiC FGM fabricated under centrifugal force were investigated experimentally and numerically. Two types of centrifugal casting, solid-particle method and mixed-powder method were considered. The desired formation of compositional gradient can be obtained by choosing the appropriate centrifugal casting method with certain conditions.

In summary, there are many potentially useful applications of the FGM concept which is not limited to the fields discussed in this report as well as the manufacturing processes of FGMs. The FGM can be applied in very wide field. However, the fundamental concepts especially the gradation of the material ingredients should be clear first before applied for a certain application.

List of Publications

1. Saifulnizan Jamian, Hisashi Sato, Eri Miura-Fujiwara and Yoshimi Watanabe, Finite Element Analysis of Severe Plastic Deformation of Difficult-to-Work Material by Equal-Channel Angular Pressing at Ambient Temperature, Japanese Journal of Applied Physics **50** (2011) 01AJ06.

2. Saifulnizan Jamian, Hisashi Sato, Eri Miura-Fujiwara and Yoshimi Watanabe, Experimental Study on Severe Plastic Deformation of Ti by Novel Equal-Channel Angular Pressing, Japanese Journal of Applied Physics **51** (2012) 01AK04.

3. Saifulnizan Jamian, Hisashi Sato, Hideaki Tsukamoto and Yoshimi Watanabe, Analysis of FGM Crash-box using Finite Element Method, to be published in Proceeding of FGM Symposium **25** (2012).

4. Saifulnizan Jamian, Hisashi Sato, Hideaki Tsukamoto and Yoshimi Watanabe, A Numerical Crashworthiness Investigation of FGM Crash-Boxes under Axial Quasi-static and Dynamics Loading, submitted to International Journal of Solids and Structures.

5. Saifulnizan Jamian, Hisashi Sato, Hideaki Tsukamoto and Yoshimi Watanabe, Thermo-Visco-Plasticity and Creep Analysis of Thick-Walled Cylinders and Pressure Vessels made of Functionally Graded Materials, to be submitted to Japanese Journal Applied Physics.

6. Yoshimi Watanabe, Saifulnizan Jamian, Eri Miura-Fujiwara and Hisashi Sato, Fabrication of Active Smart Composites by a Centrifugal Mixed-Powder Method, in Proceeding of 11th Japan International SAMPE, Tokyo (2009) SMS-4-1.

7. Saifulnizan Jamian, Hisashi Sato and Yoshimi Watanabe, Formation of Compositional Gradient in Al/SiC FGM Fabricated under Centrifugal Force: Solid-Particle Method and Mixed-Powder Method, to be submitted to Journal of Material Processing Technology.